



Electrochemical, Polarization, and Crevice Corrosion Testing of Inconel X750

A Supplement to the Environmental Control and Life Support System Sustaining Metal Materials Compatibility Study

R.E. Lee

*Jacobs Space Exploration Group (JSEG)/Bevilacqua Research Corporation
Marshall Space Flight Center, Huntsville, Alabama*

Prepared for Marshall Space Flight Center
under Contract 80MSFC18C0011

December 2019

The NASA STI Program...in Profile

Since its founding, NASA has been dedicated to the advancement of aeronautics and space science. The NASA Scientific and Technical Information (STI) Program Office plays a key part in helping NASA maintain this important role.

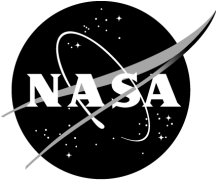
The NASA STI Program Office is operated by Langley Research Center, the lead center for NASA's scientific and technical information. The NASA STI Program Office provides access to the NASA STI Database, the largest collection of aeronautical and space science STI in the world. The Program Office is also NASA's institutional mechanism for disseminating the results of its research and development activities. These results are published by NASA in the NASA STI Report Series, which includes the following report types:

- **TECHNICAL PUBLICATION.** Reports of completed research or a major significant phase of research that present the results of NASA programs and include extensive data or theoretical analysis. Includes compilations of significant scientific and technical data and information deemed to be of continuing reference value. NASA's counterpart of peer-reviewed formal professional papers but has less stringent limitations on manuscript length and extent of graphic presentations.
- **TECHNICAL MEMORANDUM.** Scientific and technical findings that are preliminary or of specialized interest, e.g., quick release reports, working papers, and bibliographies that contain minimal annotation. Does not contain extensive analysis.
- **CONTRACTOR REPORT.** Scientific and technical findings by NASA-sponsored contractors and grantees.
- **CONFERENCE PUBLICATION.** Collected papers from scientific and technical conferences, symposia, seminars, or other meetings sponsored or cosponsored by NASA.
- **SPECIAL PUBLICATION.** Scientific, technical, or historical information from NASA programs, projects, and mission, often concerned with subjects having substantial public interest.
- **TECHNICAL TRANSLATION.** English-language translations of foreign scientific and technical material pertinent to NASA's mission.

Specialized services that complement the STI Program Office's diverse offerings include creating custom thesauri, building customized databases, organizing and publishing research results...even providing videos.

For more information about the NASA STI Program Office, see the following:

- Access the NASA STI program home page at <http://www.sti.nasa.gov>
- E-mail your question via the Internet to help@sti.nasa.gov
- Phone the NASA STI Help Desk at 757-864-9658
- Write to:
NASA STI Information Desk
Mail Stop 148
NASA Langley Research Center
Hampton, VA 23681-2199, USA



Electrochemical, Polarization, and Crevice Corrosion Testing of Inconel X750

A Supplement to the Environmental Control and Life Support System Sustaining Metal Materials Compatibility Study

R.E. Lee

*Jacobs Space Exploration Group (JSEG)/Bevilacqua Research Corporation
Marshall Space Flight Center, Huntsville, Alabama*

Prepared for Marshall Space Flight Center
under Contract 80MSFC18C0011

National Aeronautics and
Space Administration

Marshall Space Flight Center • Huntsville, Alabama 35812

Available from:

NASA STI Information Desk
Mail Stop 148
NASA Langley Research Center
Hampton, VA 23681-2199, USA
757-864-9658

This report is also available in electronic form at
<<http://www.sti.nasa.gov>>

EXECUTIVE SUMMARY

In previous studies, electrochemical test results were experimentally acquired and then presented for several noble alloys in two specific solutions representative of waste liquids generated or present within the Environmental Control and Life Support System (ECLSS) aboard the International Space Station (ISS). Subsequently, another metal candidate, Inconel X750, has been submitted and was subjected to the same test routines in the same solutions and evaluated with the same statistical/analytical methodologies as those utilized in the earlier studies. Previous studies included three titanium grades, (Commercially Pure, 6Al-4V alloy, and 6Al-4V Low Interstitial alloy), two nickel-chromium alloys (Inconel® 625 and Hastelloy® C276), one high tier stainless steel (Cronidur® 30), and a nickel-titanium alloy (Nitinol 60). Thus far, all candidate alloys have exhibited excellent corrosion protection and galvanic compatibility attributes and have been deemed qualified materials for application within the ECLSS facility. Inconel X750 now joins that group. The titanium alloys gave the best results of all the metal candidates by demonstrating superior nobility and galvanic protection properties. It is worth noting that the corrosion performance properties for the three titanium alloys were essentially indistinguishable. As such and for expediency, this study and all future evaluations will refer only to the comparative properties already documented for Titanium 6Al-4V as this alloy is representative of all three alloys and considered to be more mainstream.

Now the measured corrosion properties for Inconel X750 were very similar to those determined previously for Inconel 625 and Hastelloy C276 which were also determined to be very high performers. For the current effort, the results have clearly shown that Inconel X750 possesses exceptional anti-corrosion attributes comparable to metals in the highest tier of the galvanic series. Overall, one can conclude that Inconel X750 is quite noble, highly corrosion resistant and galvanically compatible with the other metal groups from both an electrochemical perspective and a long-term exposure scenario. This was clearly demonstrated after utilizing the same techniques as those applied in previous studies which included linear, Tafel and cyclic polarization, galvanic coupling with each of the other metal candidates, and pitting/crevicing assessments after one full year of immersion in the subject test solutions. Attributes defining the nobility and anti-corrosion capabilities for X750 appear to be on par with all the other candidates thus far and this alloy can now be classified as ‘excellent’ exhibiting very high resistance toward general, localized, and galvanic corrosion in the subject test media.

TABLE OF CONTENTS

| | |
|---|----|
| 1.0 INTRODUCTION | 1 |
| 1.1 Polarization Concepts | 2 |
| 2.0 EXPERIMENTAL | 2 |
| 2.1 Test Sample Preparation | 2 |
| 2.2 Procedures and Techniques | 3 |
| 3.0 RESULTS OF CORROSION TESTING | 8 |
| 3.1 Crevice Corrosion Assessment | 8 |
| 3.2 Electrochemical Assessment | 10 |
| 3.3 Summary and Conclusions | 22 |
| APPENDIX | 23 |
| A.1 Electrochemistry Concepts | 23 |
| A.2 Test Configuration and Parameter Definition | 23 |
| A.3 The Polarization Curve | 25 |
| A.4 The Butler-Volmer Equation | 26 |
| A.5 Faraday's Law and Oxidation Rates | 28 |
| A.6 Estimation of Currents and Rates | 29 |
| A.7 Analysis of Cyclic Polarization Curves | 34 |
| A.8 Semi-Log vs. Normal Cyclic Polarization Plots | 37 |
| A.9 Special Method for Determination of Electron Exchange Equivalents | 39 |
| A.10 Model Development for Pitting Rates and Penetration Depths Over Time | 42 |
| A.11 Increasing Solution pH Over Time | 45 |
| A.12 Special Method for Estimating Corrosion Susceptibilities | 48 |
| A.13 Passive Films as Pseudo-Capacitors and Semiconductors | 52 |
| A.14 Anomalies on Nickel Alloys under Extreme Test Conditions | 53 |
| REFERENCES | 60 |

LIST OF FIGURES

| | | |
|------------|---|----|
| Figure 1. | Images of a (a) Gamry 3000 potentiostat test system, (b) ParStat 3000 potentiostat test unit, and (c) flat test cell which can be attached to either system. | 4 |
| Figure 2a. | Typical workstation and test cell configuration showing four Gamry 3000 ready for use. | 5 |
| Figure 2b. | Two views of a connected Flat Test Cell containing Pretreat solution and attached test sample during a polarization test run. | 5 |
| Figure 3. | Incremental flow sequence for polarization testing. | 7 |
| Figure 4. | Descriptive images of X750 crevice samples after one year immersion in the subject test solutions revealing clean, undisturbed surfaces corresponding to microscopic analysis. | 9 |
| Figure 5. | Linear polarization test plot and analysis for Inconel X750 sample 11b in pretreat. | 11 |
| Figure 6. | Tafel polarization test plot and analysis for Inconel X750 sample 9a in brine. | 12 |
| Figure 7. | Cyclic polarization test plot with parameter descriptions for Inconel X750 sample 15c in pretreat. | 13 |
| Figure 8. | Galvanic couple test plot for Inconel X750 (Test) and Hastelloy C276 (Counter) in pretreat. | 19 |
| Figure A1. | Simple diagram of the PAR potentiostat – and flat cell connections used in this project. | 24 |
| Figure A2. | Current versus potential plot for one of the Cronidur samples showing anodic and cathodic branches. | 25 |
| Figure A3. | Linear polarization test plot and analysis for Hastelloy C276 in Concentrated Pretreat. | 31 |
| Figure A4. | Semi-log Tafel polarization test plot and analysis for Titanium 6Al-4V in Diluted Pretreat. | 32 |

LIST OF FIGURES (Continued)

| | |
|---|----|
| Figure A5. Possible pathways of Titanium, Chromium and Nickel in acidic solution. | 33 |
| Figure A6. Cyclic polarization test results and analysis for Hastelloy in brine. | 35 |
| Figure A7. Cyclic polarization test results and analysis for Cronidur in pretreat. | 35 |
| Figure A8. Method for evaluation of critical pitting and repassivation parameters using semi-log and normal plots. | 38 |
| Figure A9. (a) Depth profile of the passive layer on Inconel 700 contrasting the relative metallic concentrations in the base metal and the passive oxide ^[11] . (b) Depth profile of the passive layer on 316 stainless steel contrasting the relative metallic concentrations in the base metal and the passive oxide ^[12] | 39 |
| Figure A10. Average model composition and equivalents for the Hastelloy-oxide system in acidic solution. | 41 |
| Figure A11. Example of modelled pitting penetration depths and rates for Cronidur 30 and Titanium LI. | 44 |
| Figure A12. Simplified depiction of passive layer formation on a chromium alloy in air. | 45 |
| Figure A13. Illustration of a passivated chromium alloy a few seconds after immersion in an acid electrolyte. | 46 |
| Figure A14. Illustration of a chromium alloy several minutes after immersion. | 46 |
| Figure A15. Example Open Circuit Potential curve obtained from previous studies. | 47 |
| Figure A16. Pitting initiation plots for three of the test metals in pretreat showing the respective active areas. | 49 |
| Figure A17. Cyclic plot for Titanium LI showing possible relationships between conductivity and susceptibility. | 50 |
| Figure A18. Cyclic plot for Cronidur 30 showing possible relationships between conductivity and susceptibility. | 50 |

LIST OF FIGURES (Continued)

| | |
|--|----|
| Figure A19. Possible reactions for a chromium substrate leading to conduction, oxide production and dissolution. Cr = metal atom in base metal, V_{Cr}^{3-} = cation vacancy in oxide lattice, Cr_{Cr} = metal cation at cation site in oxide lattice, v_{Cr} = vacancy in base metal, Cr_i^{3+} = interstitial cation in oxide lattice, $V_O^{\bullet\bullet}$ = oxygen vacancy in oxide lattice, Cr^{6+} (aq) = fully oxidized metal cation in solution, O_O = oxygen anion in oxygen lattice, and $CrO_{3/2} = \frac{1}{2} Cr_2O_3 = Cr_{Cr} + 1\frac{1}{2} V_O^{\bullet\bullet}$ | 52 |
| Figure A20. Hastelloy sample surface after cyclic polarization scan in pretreat with $-0.75V$ cathodic conditioning. | 53 |
| Figure A21. Illustration of possible polarization paths during and after primary passivation. | 56 |
| Figure A22. Illustration of possible processes during anodic passivation of Ni-Cr alloys under reverse bias. | 57 |
| Figure A23. Cyclic polarization scan for the anomalous Hastelloy sample shown in figure A20. | 58 |

LIST OF TABLES

| | | |
|-----------|--|----|
| Table 1. | Reduced data analysis and summary for linear, Tafel and cyclic polarization. | 15 |
| Table 2. | Reduced Data Summary for Galvanic Coupling Evaluations. | 20 |
| Table A1. | Average representative values utilized for ϵ_r and ΔE_f^0 during estimation of relative susceptibilities. | 51 |

CONTRACTOR REPORT

1.0 Introduction

On the ISS, potable water is generated from the ECLSS module as waste liquids are ‘pretreated’ with an acid stabilizer formula in a process that ultimately leads to the recovery of about 75-85% of the water. ECLSS construction materials must withstand long-term exposures to these aggressive solutions. Several alloys have successfully been evaluated over the last few years and the list of qualified materials continues to grow as Inconel X750 can now be included in that list. The Final Briefing for the Inconel X750 evaluation was given to the ECLSS project in March 2019. This Final Report can be considered as a concluding extension to that effort.

In retrospect, five metal groups underwent a year-long series of electrochemical, galvanic and crevice corrosion evaluations. Candidates included Titanium 6Al-4V, Inconel® 625, Hastelloy® C276, Cronidur® 30) and Nitinol 60. All of the alloys were qualified in two test liquids, simulated ECLSS waste solution after addition of pretreatment chemicals and then the associated brine concentrate. For the present work, the same test regime was implemented with samples of Inconel X750 in the same media. Specific electrochemical methods consisted of general and localized corrosion experiments utilizing DC polarization (which included Linear, Tafel and Cyclic polarization), and one-to-one Galvanic Coupling measurements (with reference to ASTM G102). As before, crevice evaluations utilized double plate, sandwich-type assemblies simulating both parallel and angled crevice configurations intended to assess long-term performance of the metals after 6 and 12-month immersion stays in both solutions. These techniques were based on ASTM G78.

The two test solutions utilized in this study consisted of:

- (1) Collected waste liquid containing pretreatment additions of chromic acid and phosphoric acid. This liquid may be referred to simply as the ‘pretreat’ solution.
- (2) The consolidated brine associated with solution (1) which may be referred to as the ‘brine’.

For the Final Briefing covering Inconel X750, the results revealed no visible signs of corrosion activity nor did they indicate any electrochemical activity associated with general corrosion, pitting or crevicing for any of the X750 samples evaluated in either of the test solutions. The current document wraps up these findings in greater detail by concluding that Inconel X750 is quite resistant to general and localized corrosion, and is also galvanically compatible with each of the other metals in both solutions. This was clear throughout the entire testing phase as no abnormal electrochemical indications or visible surface anomalies were noted during any of the test runs. Final reduction and analysis of the test data, along with the supporting correlation results confirm these observations. The high nobilities and low corrosion susceptibilities apparent for all the candidates studied thus far are in accordance with their established positions in conventional Electrochemical Tables and Galvanic Series published throughout the literature. As is well recognized, when exposed to the air, all of these metals spontaneously form tenacious, self-repairing, passive oxide layers on their surfaces which provide an extraordinary level of nobility and protection in very corrosive environments. Indeed, these naturally-forming oxide layers are exclusively responsible for their superior corrosion resistance and high positions in the galvanic series.

1.1 Polarization Concepts

Whenever the potential (voltage) and electric current (or current density) are measured and evaluated together, the potential becomes an indication of the metal's nobility which is related to the tendency, probability or susceptibility for corrosion to occur. The current is directly proportional to both the rate of metal oxidation and reductive oxide formation, and can be converted into values indicating how fast the base metal recesses and the oxide layer grows. In most cases, base metal recession (etching) and oxide growth (passivation) are mutually inclusive processes. In acidic media, the oxide layer is also slowly dissolving. Under true Steady State conditions, the rate of oxide formation is exactly equal to the rate of oxide dissolution. A high breakdown potential infers high nobility with low susceptibility to corrosion, while a large pitting current indicates a high pitting rate. A high corrosion potential typically implies a high susceptibility to general corrosion while a high repassivation current indicates a robust oxide-restoration and recovery process (repassivation) which, for these particular metals, is ready to 'kick into gear' the moment the oxide layer is breached.

2.0 Experimental

2.1 Test Sample Preparation

2.1.1 Machining and Finishing of Test Samples

All test samples were machined from bulk metal stock into approximately 3" X 3" X 1/3" plates. This size was deemed appropriate for all of the polarization, galvanic and crevice corrosion testing as mandated by the ECLSS project to satisfy the requirements for evaluating the performance and compatibility of each metal candidate of interest. All the metal samples were degreased, rinsed and dried, and then liberally rinsed with DI water, solvent rinsed and air dried in ambient atmosphere (68-72°F and 30-40% R.H.) to promote natural development of their native surface oxide layers prior to testing.

2.1.2 Crevice Sample Assembly Configuration

Samples for evaluating crevice corrosion effects were assembled in two different configurations. Even though the procedure loosely followed ASTM G78, the specific test approach utilized throughout these studies was developed in-house at Marshall Space Flight Center several years back.

Angled Crevice Sample Configuration

Sandwich-type assemblies consisted of two sample plates clamped together and separated by a small rectangular-shaped, single layer of filter paper near one side of the clamped assembly to create a tiny *angled crevice gap* between the two plates.

Parallel Crevice Sample Configuration

Sandwich-type assemblies consisted of two sample plates clamped together and separated by a larger square-shaped, single layer of filter paper centered on one of the plates to create a tiny *parallel crevice gap* around the edges between the two plates.

2.2 Procedures and Techniques

2.2.1 Crevice Corrosion Evaluations

Identified test assemblies of all metals were immersed in each of the two test solutions for up to one year. Samples were monitored periodically throughout. Half of the samples were removed after 6 months storage and were carefully cleaned and evaluated. At the end of the one year period, the other half was removed, cleaned and evaluated. After removal from the test solutions and thorough rinsing, each sample was subjected to visual and microscopic evaluation to check for signs of corrosion, surface growth, pitting, base metal degradation and/or any other outstanding anomaly.

2.2.2 Polarization Workstations and Equipment

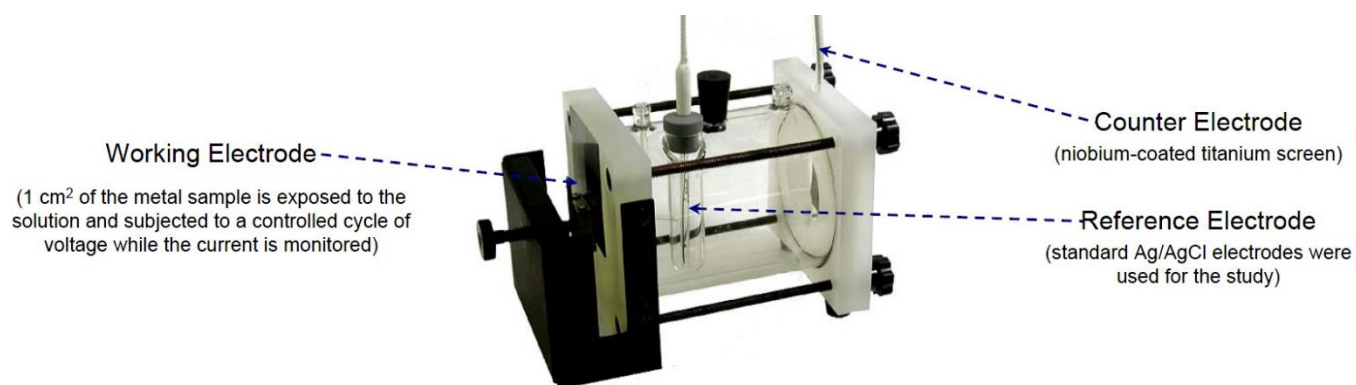
Electrochemical measurements were carried out utilizing computer-controlled potentiostat workstations supplied by Gamry Instruments and on occasion, units provided by Princeton Applied Research (PAR). Four Gamry 3000 models and two PARSTAT 3000's were available throughout the study. Both of these systems included their own proprietary software for data collection and analysis. Test solutions and metal samples were accommodated using simple Flat Test Cells throughout the project which included a single 1 cm² exposure hole on one end of the cell for polarization routines and a 1 cm² exposure hole on each end of the cell for galvanic coupling evaluations. Throughout all of these studies, a Ag/AgCl reference electrode has been utilized. The equipment, experimental configurations and workstations are depicted in Figures 1 and 2 below.



(a) Gamry 3000



(b) ParStat 3000



(c) Flat Test Cell

Figure 1: Images of a (a) Gamry 3000 potentiostat test system, (b) ParStat 3000 potentiostat test unit and (c) flat test cell which can be attached to either system.



Figure 2a: Typical workstation and test cell configuration showing four Gamry 3000 ready for use.

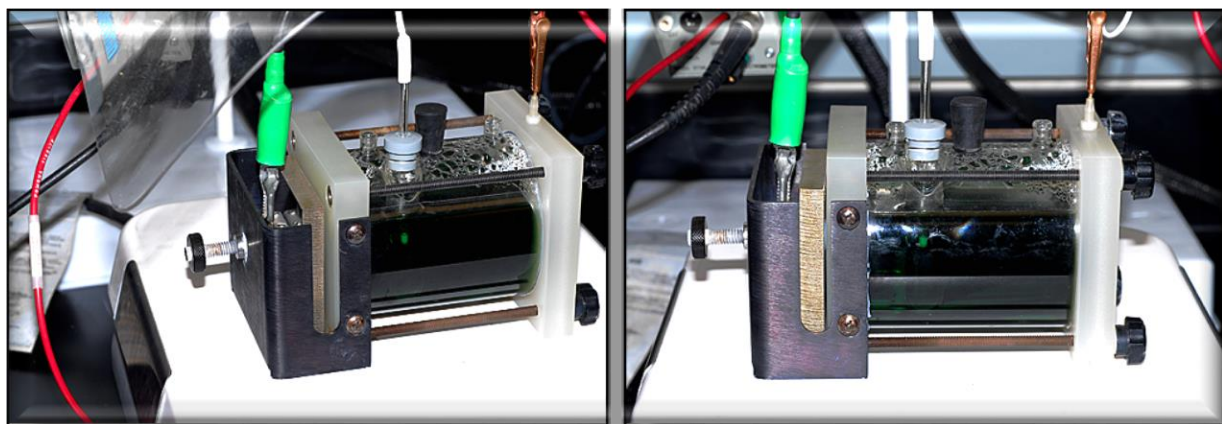


Figure 2b: Two views of a connected Flat Test Cell containing Pretreat solution and attached test sample during a polarization test run.

The flat cell offers flexibility for a variety of DC electrochemical studies including Open Circuit, Linear, Tafel, Cyclic polarization and Galvanic Coupling measurements. For Galvanic Coupling tests, the cell is re-assembled using a second 1cm² sample area end-cap for the other metal so that both samples are connected across the test solution. The second metal is grounded and interacts with the first metal which is monitored for voltage and current changes.

2.2.3 DC Polarization Test Descriptions

Electrochemical test descriptions employed for these studies are given below.

Open Circuit Analysis (OCP) – Nondestructively measures the steady state open circuit potential E_{OC} as a single metal is exposed to the solution over time with no power applied. Provides potentiostatic information regarding the relative nobility of a metal in terms of its open circuit voltage while being exposed to the test solution under static, nonpolarizing conditions.

Linear and Tafel Polarization – Nondestructively measures the resulting current response when a very small voltage is applied relative to the OCP. Provides the corrosion resistance R_{Cor} , corrosion current I_{Cor} , the beta Tafel parameters and the corrosion rate k_{Cor} . These results provide indications regarding the propensity for general corrosion to occur under steady state conditions. A very small, voltage ramp is applied from the cathodic region to the anodic region under slightly polarizing conditions (± 20 -200mV)

Cyclic Polarization – Measures the resulting current response over a wide voltage range with possible sample surface alterations. Provides potentiodynamic information regarding corrosion tendencies when the metal is exposed to the test solution while a complete voltage loop is applied from a preselected cathodic point across the entire anodic region. The ramp takes the metal beyond its Tafel zone and through its breakdown potential E_{Brk} to a preselected ‘vertex’ potential and then back down through the repassivation zone. A hysteresis loop is usually generated. Pitting phenomena, passive oxide growth and oxide destabilization as well as repassivation protection and recovery mechanisms are explored. Supplemental general corrosion information may also be obtained from cyclic polarization data.

Note: For clarity, it should be realized that the microstructures comprising the passive oxides on these metals are not always damaged catastrophically at E_{Brk} , but rather their electrical insulation properties undergo a rapid transformation as resistance drops off and conduction increases across the layer possibly allowing external corrosive agents to interact directly with the metal surface which could lead to pit initiation. This is due to the rapid increase in the mobility of charge carriers near E_{Brk} . As the voltage is further increased, tunneling of the electrons may occur and then at some point beyond E_{Brk} , the oxide structures may physically breakdown while the fractured remnants begin dissolving in the test solution.

Galvanic Coupling – Nondestructively measures the steady state galvanic potential E_{OCG} and galvanic current I_g as two metals interact across the test solution under open circuit conditions with no power applied. Provides information regarding changes in nobility (potential) and passivation response (via current) for the test metal relative to a counter metal in a simulated galvanic couple situation.

Many researchers may include, in their testing strategy, a cathodic conditioning step on the sample prior to or at the beginning of the test run by starting the scan at a potential far below the pre-measured open circuit potential (OCP). The effect of such conditioning is to cathodically strip the existing native oxide layer from the metal surface and then allow a new passive layer to form within the solution. This newly-formed (solution-driven) oxide layer may be very similar to the air-formed coating, but it is not necessarily the same. The intent of these current studies is to evaluate the material ‘as-is’ in their post-

machining state *and* with their air-formed oxide layers in their original condition. This is considered to be more representative of the material that is actually utilized to assemble the ECLSS structures.

In any event, the air-formed oxide layer will tend to adapt to the new environment over the first few minutes of immersion, possibly undergoing slight changes in surface composition and/or microstructure. Since pre-immersion cathodic conditioning is not applied to the actual ECLSS structures and components assembled for the ISS (and would probably be impossible to accomplish), such laboratory treatments are considered to be inapplicable and possibly misleading regarding the goals of these experiments. Alternatively, our preparation approach included vigorous rinsing steps for the samples in DI water and organic solvent followed by 24 hours of ambient air drying under common atmospheric conditions (68°-72°F, 40-60% R.H.) in order to encourage a clean, robust natural passive layer to form on the surfaces prior to testing. When available, a few complementary test samples were intentionally subjected to negative cathodic voltages during cyclic testing as part of the overall evaluation approach in order to better understand the effects of extreme corrosive applications.

2.2.4 Polarization Test Sequence

Metal candidates were subjected to the test sequence depicted in Figure 3 below. Depending on required data accuracy, 4 to 12 independent test sample areas were evaluated for each candidate metal in order to obtain the best averages possible.

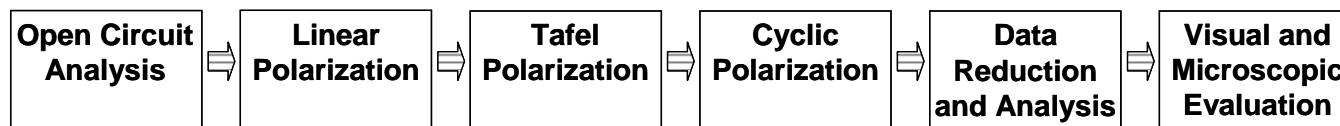


Figure 3: Incremental flow sequence for polarization testing.

2.2.5 Galvanic Coupling

In this phase of the testing, test cells were mounted with two metal samples, one acting as the ‘Test’ or ‘Working’ electrode and the other as the ‘Counter’ electrode. The test assembly is allowed to sit under open circuit conditions with no power applied while potential and current changes associated with the Test sample are monitored as it responds to the presence of the Counter sample over time. For all the metals in this study, galvanic potential changes were very small, most being in the nano-amp ranges. Observed increases in either potential, current or both indicate that the Test metal is anodic to the Counter metal (less noble). Increases in galvanic potential are typically relative to the Test metal’s Open Circuit Potential (OCP). Such increases are also often accompanied with slight increases in the rates for base metal recession and passivation as the Test metal’s self-protective mechanisms intensify (slightly). If the Working metal is cathodic to the Counter metal, the galvanic potential drops below the Test metal’s OCP while the rate of passivation decreases. Cathodic behavior indicates that the Working metal is nobler than the Counter metal as the Working metal’s corrosion protection requirements are relaxed. Since no power is applied to the cell during this test, no degradation on either of the exposed surfaces takes place (generally), at least for the noble metals evaluated during these studies. For galvanic coupling pairs, 4 to 12 independent test runs were conducted for each metal-to-metal pair during the primary testing phase. In addition, many ‘test repeats’ were conducted in order to obtain the necessary degree of accuracy throughout the averaging and analysis process.

3.0 Results of Corrosion Testing

3.1 Crevice Corrosion Assessment

As described previously, test samples for each metal were stored in each of the two test solutions for 6 months and 12 month time intervals. At 6 and 12 month intervals, designated samples were removed, carefully cleaned and visually inspected under magnification. Six month test results were presented at the Mid-Term Briefing and revealed no corrosion issues. Results of the twelve month samples were practically identical to the six month group with no anomalies noted on any sample surface for either of the test solutions. Group images showing one side of each angled and parallel sample surface for the 12-month run in both solutions are given in Figure 4.

The pH of each storage solution was measured at the start of the test and then at the end of the test period. In general, slight increases in pH were observed over time. Nevertheless, overall changes in solution pH indicated no anomalies which could be attributed to corrosion events since no corrosion was observed on any surface in any solution. Acidic solutions are generally anodic as they tend to dissolve the passive oxide. This intensifies the metal's anti-corrosion mechanisms by increasing the regeneration of protective oxide. Observed increases in pH are likely due to consumption of acidic hydrogens via reduction to form molecular hydrogen (which bubbles away) as metal ions comprising the oxide are dissolved into solution. An example of this scenario is graphically illustrated in the Appendix section of this report. For noble metals such as these, a steady state condition is established between the rates of passive layer dissolution and passive oxide regeneration shortly after immersion and persists throughout the remainder of the test.



Figure 4: Descriptive images of X750 crevice samples after one year immersion in the subject test solutions revealing clean, undisturbed surfaces corresponding to microscopic analysis.

3.2 Electrochemical Assessment

Compared to ‘localized’ forms of corrosion such as pitting or crevice formation, ‘general’ corrosion or etching involves larger areas of the base metal which interact with the environment via oxidation. A classic corrosion example is the rusting of iron alloys. Common use of the term ‘Corrosion Rate’ often refers to the rate of etching or recession into the base metal as a result of corrosive oxidation reactions which leaves a crater or recessed area loosely filled with frail oxidation fragments. For corroding metals, such as the low alloy steels, these oxide-hydroxide remnants are structurally unorganized as they quickly disintegrate and wear or wash away under ambient conditions. They provide no corrosion protection to the base metal. A similar situation applies to the aluminum alloys. Even though the aluminum alloys develop a passive layer, it is weak and easily breached providing little corrosion protection in most applications.

On the other hand, strongly passivating metals such as the noble candidates under study here rapidly form oxidation products that grow and evolve into structurally organized, semi-crystalline oxide layers which provide an astounding level of protection against further oxidation. In these cases, the base metal recession depth or inward volume becomes occupied with protective oxide. With this understanding, the terms ‘corrosion rate’ and ‘recession rate’ may sometimes be used interchangeably for metals protected by these types of self-propagated passivation layers. Even though the noble metals under study here did not undergo destructive corrosion, the base metal did recede inward as a protective oxide filled the recession volume thereby preempting sustained corrosive reactions to the metal. In short, recession rates for these metals are due exclusively to growth of the protective oxide layer rather than corrosive degradation of the base metal. Again, all metals evaluated thus far, including Inconel X750, have indicated very strong anti-corrosion properties in both of the solutions evaluated.

In terms of recession rate, X750, as well as all the other previously qualified candidates, appear to be at least one order of magnitude higher than the ‘Outstanding’ rating for general and localized corrosion which is the noblest rating recognized in the corrosion industry. All of these metals exhibited very low recession depths as spontaneous growth of their respective passive oxide layers rapidly became dominant. Overall, these findings are in good agreement with published Galvanic Series in seawater as mentioned earlier. Indeed, the corrosion-resistance properties for all of these metals was comparable to that of silver. The robustness, tenacity and protective nature of the passive layers associated with Inconel X750 resembled those of the previously investigated two nickel-chromium alloys, Inconel 625 and Hastelloy C276. The Titanium alloys indicated the best properties of all the candidate evaluated so far.

With respect to the measured polarization properties, Open Circuit Potential, Linear and Tafel polarization pertain largely to general (areal) corrosion while the primary benefits derived from Cyclic Polarization lead to insights associated with crevice and pitting phenomena. However, Cyclic results may also support some of the general corrosion information obtained during the previous Linear and Tafel analysis. Galvanic compatibility assessments involve coupling the subject metal with each of the previously qualified metals in both anode and cathode positions and then evaluating the subject metal for general or localized effects as well as any other anomalies that might indicate an incompatibility.

3.2.1 Linear and Tafel Polarization

Linear and Tafel Polarization measure the current response when a small voltage scan is applied relative to the OCP. Values for the corrosion potential E_{Cor} , corrosion current I_{Cor} and corrosion resistance R_{Cor} are extracted. These data permit estimation of the Steady State time-rates for base metal recession utilizing Faraday's law, the Stern-Geary method and Butler-Volmer's equations. Also, with application of special estimation techniques developed uniquely for these studies, time-rates for passive oxide thickness growth can also be derived. Figures 5 and 6 give specific examples representative of the Linear and Tafel polarization test runs conducted during the X750 evaluation.

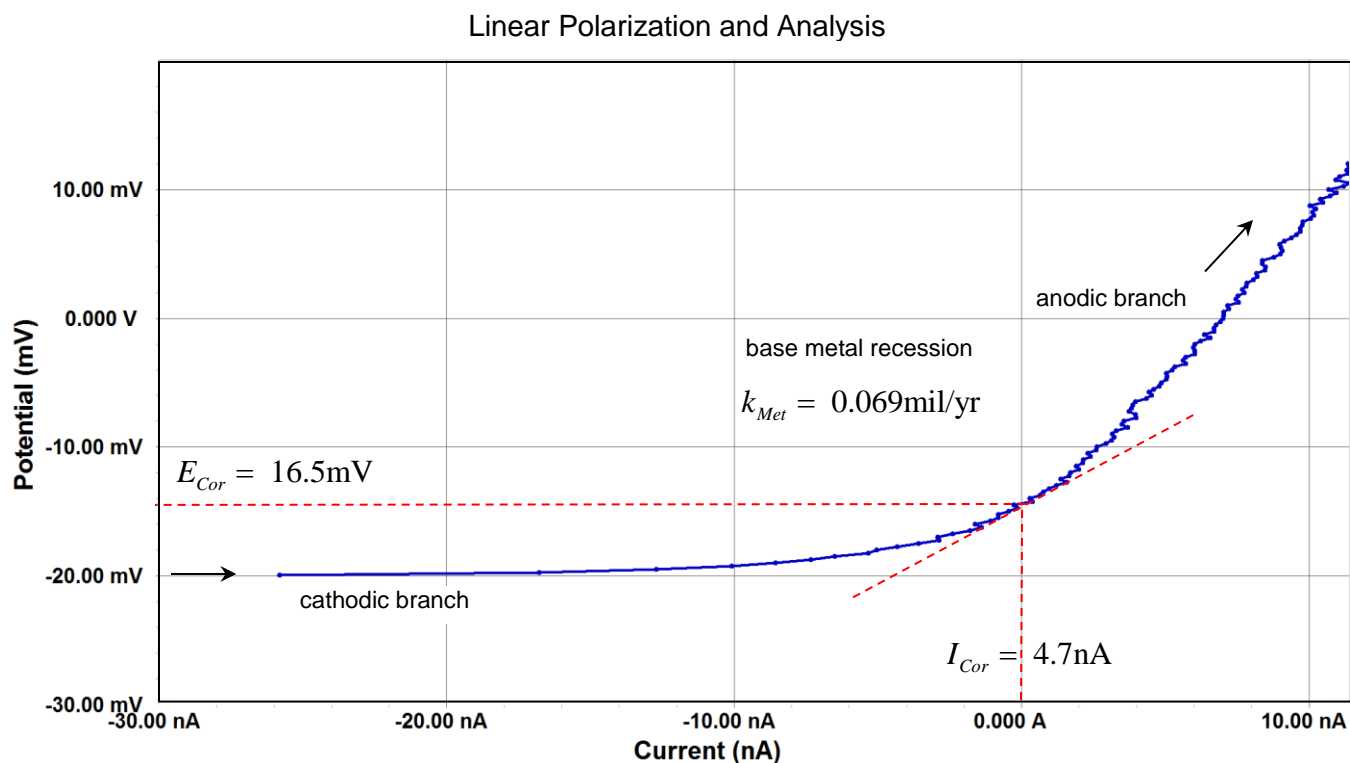


Figure 5: Linear polarization test plot and analysis for Inconel X750 sample 11b in pretreat.

* Estimation techniques, approaches and methodologies are covered in the Appendix

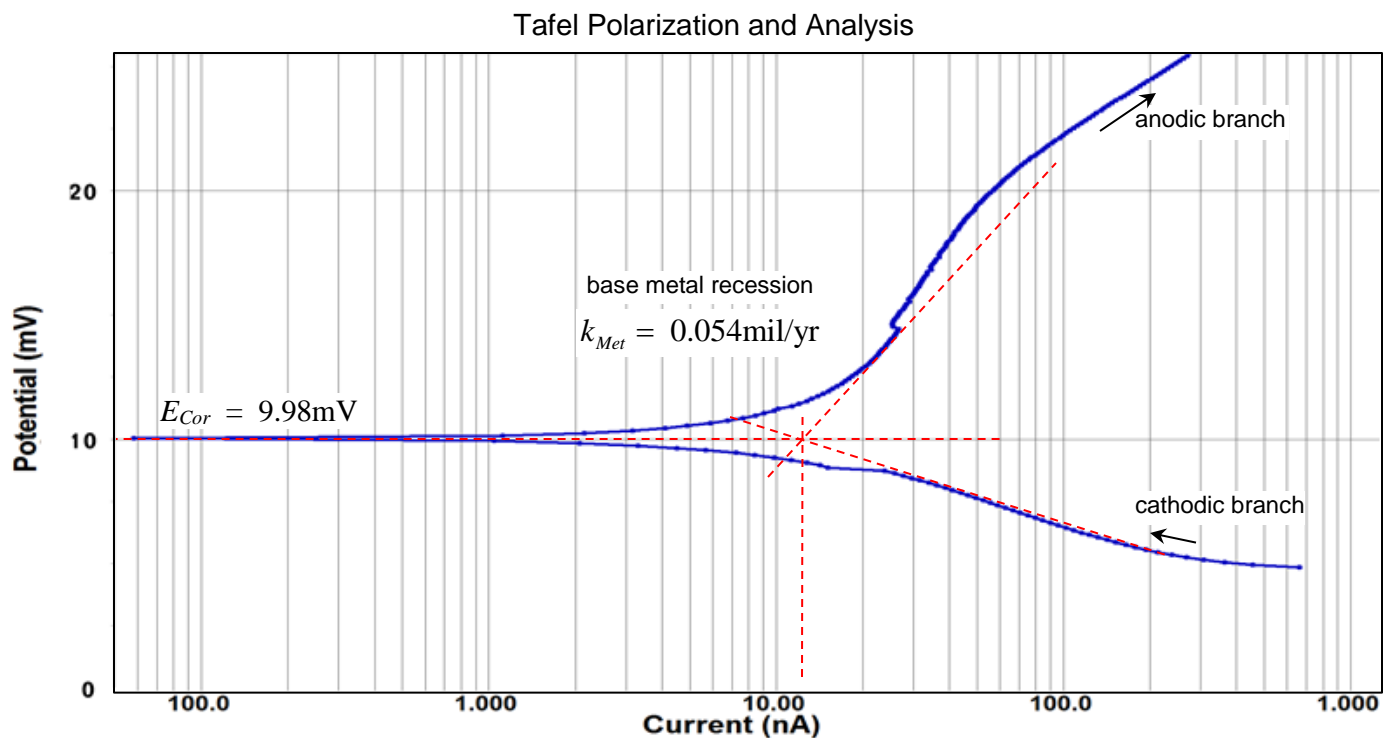


Figure 6: Tafel polarization test plot and analysis for Inconel X750 sample 9a in brine.

In general, electrochemical potential is an indication of the tendency or susceptibility for corrosion to occur, while the current (or current density) is directly proportional to the rates of corrosion or recession and passivation. Under ambient, open circuit conditions, acids will very slowly dissolve the passive oxide layer as new oxide is being generated. At the Steady State, the rate of dissolution and oxide growth are equal. Again, none of the metal candidates in this study, including Inconel X750, actually underwent destructive corrosion but instead, their natural oxide layers grew and strengthened (consuming base metal), until adequate protection is achieved at the Steady State. This typically defines the point in which the rates of metal recession, oxide growth and oxide dissolution reach equilibrium.

In the laboratory, the actual number of polarization tests conducted per metal candidate ranged from 4 to 12 depending on the degree of accuracy needed. This approach was followed throughout in order to obtain the most representative averages for each test. The refined results were then utilized during the procedures for data reduction, consolidation, and parameter correlation. Prior to the start of the polarization testing phase, the Open Circuit Potential (OCP) for each sample was obtained.

3.2.2 Cyclic Polarization

Cyclic polarization is an accelerated test that can sometimes impart a certain degree of damage to the exposed sample area since it is subjected to higher anodic voltages than Linear or Tafel polarization. For most noble metals, this damage is usually not apparent when cyclic test parameters are kept within moderate ranges. However, if applied voltages are intentionally or inadvertently carried to extreme limits, observed damages may reveal oxide failure followed by etching or pitting of the base metal. None of the metals evaluated throughout this study indicated any such anomalies under normal test conditions. However, for purposes of inquisitiveness, a few samples were taken to potentials well above their breakdown points in order to explore their properties under induced failure conditions.

Cyclic Polarization applies a complete hysteretic voltage loop to the sample surface from a starting potential that is cathodic to the original OCP, then across the primary corrosion potential, through anodic breakdown of the oxide, repassivation, recovery and finally, back down to a new stable cathodic point. A test run for one of the X750 samples is given in Figure 7.

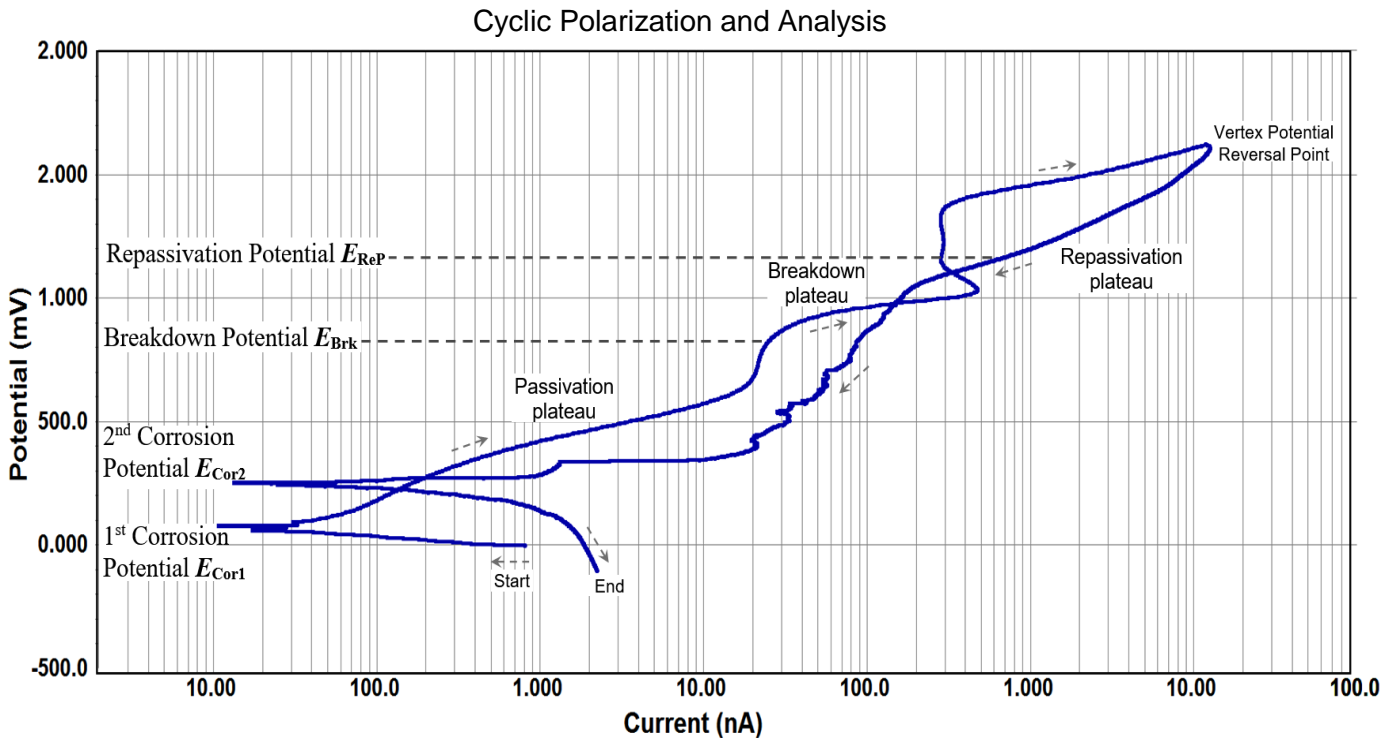


Figure 7: Cyclic polarization test plot with parameter descriptions for Inconel X750 sample 15c in pretreat.

The important test regions utilized in cyclic polarization, as indicated in Figure 7, provide the data required to fully evaluate the performance of passivating metals. These fields can be further defined to facilitate their understanding and to provide the links between the cyclic polarization data curve for each candidate and their reduced averages to be presented shortly.

First Corrosion Potential, E_{Cor1} – Pre-breakdown equilibrium point corresponding to kinetic-dominated, low level steady state oxidation. E_{Cor1} is roughly equivalent to the original open circuit condition.

Passivation Potential, E_{Pas} – Point of maximum oxide growth. Transition point where reactions become diffusion-controlled while the oxide layer thickens. Marks the beginning of the 'passive plateau'.

Breakdown Potential, E_{Brk} – Point corresponding to dielectric breakdown of the passive oxide layer. Transition point where kinetic-controlled metal recession prevails and the passive layer disintegrates.

Repassivation Potential, E_{ReP} – Point where repassivation subsides after recovery is complete prior to E_{Cor2} . Transition point where oxidation becomes diffusion-controlled due to regrowth of the oxide layer.

Second Corrosion Potential, E_{Cor2} – Post-breakdown equilibrium point corresponding to kinetic-dominated low level steady state oxidation. An elevated steady state open circuit condition that is attained at the end of the recovery process. The recovery E_{Cor2} is analogous to the ground state E_{Cor1} .

Throughout these studies, the analysis was conducted utilizing the traditional semi-log plots as shown in Figure 7 and normal plots (an example of this approach is given in the Appendix). During the first branch of the cycle shown in Figure 7, an increasing potential is applied at the beginning of the Up-Ramp and taken up to the Vertex (Reversal) Potential where the voltage begins to decrease. The First Corrosion Potential is often very close to the Open Circuit Potential measured previously. It is a stable equilibrium state in which the rates of chemical reduction and oxidation are exactly equal. Thus, the rates of base metal recession and passive oxide growth cannot be distinguished, directly measured or analytically derived at E_{Cor1} .

The Stern-Geary method is customarily used to estimate these rates and this technique is covered in the Appendix. Passive oxide growth is aggressively occurring at E_{Cor1} and beyond until the position marked as the Passivation Potential is reached (bend or elbow in the curve). At this point, oxide growth begins to level off and then becomes approximately constant along the Passivation Plateau where stable passive oxide growth occurs. As the region of Breakdown is approached, oxidation/reduction rates begin to waver while oxide stability diminishes and meta-stable pitting/etching become possible. At the Breakdown Potential, the applied voltage becomes high enough to cause the oxide to fail. Here, the protection properties of the oxide deteriorate and its microstructure may begin to disintegrate.

At and just beyond E_{Brk} , the base metal is unprotected and susceptible to attack by the solution. In some cases, this may result in obvious etching or pitting of the base metal. After the Vertex point, the potential reverses and begins to decrease along the second branch of the cycle while repassivation forces kick-in and the recovery stage begins to dominate. For Inconel X750 as well as all of the other metals previously studied, the onset of repassivation occurs almost instantly at the Vertex while re-growth of the oxide is very rapid and robust. This is indicative of the powerful protection mechanisms these noble metals possess. It is along this region where the maximum rate of repassivation occurs. At the point identified as the Repassivation Potential (bend or elbow in the curve on the linear plot), the recovery reactions begin to wind down as the system approaches a new stable point of equilibrium referred to as the Second Corrosion Potential. Thus, as the metal is powered up through Breakdown and Recovery, a higher point of stability is attained with respect to the original open circuit state.

The voltage-current hysteresis loop generated from a complete Cyclic polarization test run can reveal how well a metal either protects itself and recovers (most noble passivating metals) or fails as a result of the breakdown forces (most aluminum and steel alloys). To supplement the evaluation, a number of special factors and correlation ratios have been developed throughout these studies intended to reflect the relative performance characteristics between the candidates and to support the baseline polarization

data. Table 1 is an updated version of the reduced summary for the principal averages developed during the Linear, Tafel and Cyclic test phases of these studies. This is basically the same summary presented in earlier studies but has been expanded as each metal candidate series was evaluated and assimilated. Table 1 is the current version of reduced averages as Inconel X750 has now been incorporated into the summary (highlighted in green) allowing side-by-side comparisons of X750 with all the metals evaluated for the ECLSS Materials Compatibility Study thus far. Let us examine this table in greater depth.

Table 1: Reduced data analysis and summary for linear, Tafel and cyclic polarization.

| | Linear & Tafel Polariztion | | | Cyclic Polarization | | | | | | | |
|-----------------|----------------------------|--------------------|--------------------|---------------------|-------------------|--------------------|----------------|--------------------------------|-------------------------------------|----------------------------------|---------------------------------------|
| | Corrosion | Metal | Oxide | Corrosion | Breakdown | Recovery | Cyclic Loop | Breakdown | Susceptibilities | | |
| | Potential | Recession | Passivation | Potential | Potential | Potential | Hysteresis | Recovery | Initiation | Sustained | General |
| | E_{Cor} (mV) | Rate (mil/year) | Rate (mil/year) | E_{Cor1} (mV) | E_{Brk} (mV) | E_{Cor2} (mV) | Area (mV-A) | Ratio (k_{Rep}/k_{Pit}) | of Pitting $f(E_{Brk}, E_{Pas})$ | Pitting $f(E_{Brk}, E_{Rep})$ | Corrosion $f(E_{Cor1}, Cor2, Brk)$ |
| Pretreat | | | | | | | | | | | |
| Titanium 6Al-4V | 63.9 | 0.127 | 0.398 | 51.3 | 2157 | 1733 | -2.48 | 7.17 | 0.80 | 0.49 | 0.73 |
| Nitinol 60 | 24.7 | 0.103 | 0.347 | 22.6 | 1447 | 1403 | -0.93 | 5.80 | 1.00 | 0.45 | 2.56 |
| Inconel 625 | 15.7 | 0.114 | 0.551 | 12.4 | 996 | 911 | -0.33 | 2.17 | 5.85 | 1.02 | 5.29 |
| Hastelloy C-276 | 14.0 | 0.104 | 0.482 | 10.5 | 950 | 809 | -0.23 | 2.53 | 6.77 | 0.49 | 1.53 |
| Inconel X750 | 11.0 | 0.087 | 0.347 | 15.0 | 946 | 863 | -0.31 | 2.44 | 6.30 | 0.80 | 3.86 |
| Cronidur 30 | 17.3 | 0.088 | 0.447 | 14.5 | 653 | 196 | +22.6 | 0.47 | 9.18 | 0.46 | 4.98 |
| Brine | | | | | | | | | | | |
| Titanium 6Al-4V | 68.4 | 0.088 | 0.274 | 74.8 | 2302 | 1671 | -3.26 | 7.30 | 0.63 | 0.57 | 0.72 |
| Nitinol 60 | 31.1 | 0.091 | 0.306 | 34.2 | 1712 | 1695 | -0.69 | 7.97 | 1.03 | 0.15 | 2.15 |
| Inconel 625 | 22.7 | 0.062 | 0.302 | 41.1 | 1046 | 858 | -0.22 | 2.35 | 5.80 | 0.27 | 3.72 |
| Inconel X750 | 17.0 | 0.069 | 0.317 | 24.5 | 990 | 1011 | -0.45 | 1.67 | 4.80 | 0.50 | 5.07 |
| Hastelloy C-276 | 23.1 | 0.075 | 0.346 | 20.3 | 903 | 836 | -0.17 | 2.39 | 6.87 | 0.37 | 1.56 |
| Cronidur 30 | 20.9 | 0.056 | 0.283 | 12.2 | 766 | 261 | +17.6 | 0.19 | 11.48 | 0.81 | 4.10 |

Linear and Tafel data plots are essentially the same except that the applied potential range for the Tafel test run is wider ($\pm \sim 250\text{mV}$) and the analysis is taken from a semi-log version of the data. On the other hand, a Linear test run is only conducted across about $\pm 50\text{mV}$ and a quicker, simpler linear fit is applied at zero current. Both provide the Corrosion Potential (analogous to the OCP) and the Metal Recession Rate (analogous to the Corrosion Rate if corrosion occurred). Methods for determining the Oxide Passivation Rate are covered in the Appendix. Linear Polarization is rapid and completely nondestructive. Variations of this approach are applied throughout industry for real-time corrosion monitoring and in-field assessments.

Normal and semi-log plots for Cyclic Polarization test runs can often produce an abundance of qualitative and quantitative information. Figure 6 depicts regions and points along the Cyclic curve which are deemed significant or informative. The Corrosion Potential indicated from a Cyclic plot is analogous to that determined in the Linear/Tafel phase and the OCP. The Breakdown Potential (at the end of the Passive Plateau) may be the most important property as it quantitatively indicates the tenaciousness of the passive oxide layer in combination with its rapid ‘self-healing’ effects during exposed to the subject test

solution. The slope of the line segment immediately following the Reversal Point up to the Recovery Potential may be an indication of the regenerative self healing power associated with the passive oxide as the system either recovers after Breakdown or falters. The Recovery Potential is clearly seen on the *normal* plot.

As described earlier, during a typical Cyclic Polarization test run, a constantly increasing potential is applied to the sample up to a preselected potential where it is immediately reversed and then constantly brought back down to near the starting point. The up-ramp side of the plot is identified as the anodic branch while the down-ramp side is the cathodic branch. The anodic ramp is driven by a positive oxidizing voltage while the cathodic side is mapped out under a negative voltage where conditions supporting reduction become more favorable. At the point where the up-ramp transitions into the down-ramp (the Reversal point), the ever-increasing anodic stress is instantly relieved and continues to decline, directly or indirectly, until E_{Cor2} is reached.

When the Breakdown point is reached along the anodic up-ramp, the oxide layer has either (1) completely surrendered to the forces and ominously exposed the base metal leading to major pitting, (2) partially yielded to the oxidizing forces allowing restrained exposure of the base metal followed by metastable pitting, (3) weakened but remained intact while continuing to provide protection to the base metal, or (4) remained completely inert to the anodic forces and provided robust protection throughout the process. With these descriptions, the apparent order of nobility could be written . . . (4) > (3) > (2) > (1). Of the metal candidates studied so far, Inconel X750, along with Inconel 625 and Hastelloy C276 would appear to fall in category (3), while the Titanium alloys would be placed in (4) and Cronidur 30 in (2).

The net area of the Cyclic Polarization hysteresis loop is often presented in these types of analyses to provide a relative indication for the tendency of the passivated metal either to recover or succumb to the corrosive forces after the passive oxide layer has been subjected to the applied anodic potential. The sums of the relative proportions of negative and positive areas are a reflection of this tendency. Negative areal values infer strong repassivation/recovery forces while positive values indicate the likelihood for continued degradation after breakdown/reversal. Regions or segments along the cathodic branch in which the current is directed backwards (in a negative direction) and cross over the anodic branch form negative areas within the trace while regions or segments where the current continues to increase remain ahead of the anodic branch forming positive areas. The net areal value given for Inconel X750 in Table 1 is indicative of its moderately strong breakdown recovery properties and its similarities to Inconel 625 and Hastelloy C276 previously qualified. The highly negative area of the Titanium alloys are a semi-quantitative reflection of their superior nobility over all the other candidates.

Concepts associated with the Recovery Potential and the Repassivation Potential are equivalent since both are linked to the forces driving the repassivation process as the metal undergoes recovery after exposure to breakdown conditions. In any event, the higher the Breakdown and Recovery Potentials are, the nobler the metal is. Methods for approximating the Breakdown Recovery Ratio (BRR) and Susceptibilities for Pitting Initiation (S_I), Pitting Sustainment (S_S) and General Corrosion (S_G) are covered in the Appendix. The BRR is the maximum rate of oxide repassivation after the reversal point over the maximum rate of attainable pitting prior to reversal. If $BRR > 1$, resistance to oxide failure is enhanced as the repassivation/recovery forces prevail through and beyond the breakdown point. The larger this factor is, the stronger the repassivation attributes are. If $BRR < 1$, resistance to oxide failure may be less than desirable as the recovery forces tend to struggle just after E_{Brk} but eventually take over along the

repassivation plateau. If BRR is $\ll 1$, pitting may be prominent. Initiation of pits does not automatically imply that sustained pitting will follow. Pits may try to initiate (metastable pitting) but then are quickly overwhelmed by vigorous oxide regeneration, otherwise, they may continue to grow in a sustained manner. Sustained pitting events are by no means constant. S_I provides a relative indication of how well the original passive layer might prevent the onset of corrosion near the breakdown point. This is a modified Weibull function of E_{Brk} , E_{Pas} and ε_r (Section A12). S_S provides a relative indication of how well the repassivation repair mechanism might prevent sustained corrosion after breakdown has occurred and pits have initiated (a modified Weibull function of E_{Brk} , E_{ReP} and ε_r). S_G provides a relative indication of how well the repassivation repair mechanism might prevent general corrosion after recovery at E_{Cor2} (a modified Weibull function of E_{Cor1} , E_{Cor2} and ε_r .)

In contrast to the more active metals in the Galvanic Series, oxidation rates for these metals are extremely small and the relative consumption of base metal due to recession is minuscule. The tenacity of the passive oxide layers on these metals along with their capabilities to regenerate new oxide ‘at-will’ appear to be quite extraordinary. It should be noted that the data in these studies pertains to the Steady State condition when the reaction rates for metal oxidation, hydrogen reduction and oxide dissolution are all in equilibrium. The Steady State may or may not accurately reflect the behavior of the metals under aggressive oxidation conditions as it is more representative of static field situations when the system is in equilibrium with its surroundings. While corrosion rates are often characterized utilizing parabolic rate kinetics, $x = (kt)^{1/2}$, results from this studies have shown that depth and thickness time-rates due to metal recession, oxide growth and dissolution are sometimes better represented using modified Weibull functions, such as $x = A(B - Ce^{-kt})^D$, which can be empirically developed from the data.

As indicated in Table 1, Inconel X750 demonstrates high marks in terms of its relative nobility and rapid generation of protective oxide when subjected to strong anodic (acidic) environments. Thus, these studies have established that Inconel X750 exhibits superior corrosion protection properties which are indicative of its ability to counteract general and local corrosive forces by accelerating the process of passive oxide generation ‘on-demand’ as well as rapid oxide regeneration whenever the layer is threatened or breached by external forces. This is in accordance with the conclusion stated regarding all the metal candidates evaluated so far.

3.2.3 Results for Galvanic Coupling Analysis

Galvanic interactions between dissimilar metals across a conducting solution will typically cause voltage differences and current flows that alter the relative electrochemical behavior of the metals involved. In our case, the two acid pretreat solutions were the conducting media. For a galvanic coupling test set-up, a metal is attached to one end of the cell and monitored for voltage and current changes as it responds to the presence of a second metal attached to the other end of the cell. The metal that is monitored is designated as the ‘Test Metal’ while the opposite metal is referred to as the ‘Counter Metal’. Throughout these evaluations, each metal was individually evaluated in both the ‘Test’ position and ‘Counter’ position in each solution until galvanic measurements in both directions were accomplished. Many test repeats were conducted for each configuration and as the list of candidates expanded with each new project, the number of required coupling tests increased. Thus, Inconel X750 was evaluated against four other metals, Inconel 276, Hastelloy C276, Titanium 6Al-4V and Nitinol 60. Cronidur 30 was inadvertently passed over during the evaluations and subsequently omitted from the analysis.

It is now well established that Inconel X750, along with all of the previously qualified candidates, are strong passivating (self-protecting) metals. Galvanic changes measured for each one of the metals evaluated throughout these studies have been very small (generally in the nano-to-micro amp range). Environments which induce corrosion are considered ‘anodic’ to some degree or another, and the solutions under investigation in these studies are moderately strong acids which facilitate the formation of potent anodic fields. When two different materials form a galvanic couple under anodic conditions, one metal typically becomes the inferior anode of the pair while the other becomes the dominating cathode. For situations in which the Test metal is the anode, the cathodic influence from the Counter electrode may cause the galvanic potential on the Test electrode to increase to a value slightly above its original OCP $\sim E_{Cor}$ (which is regarded the baseline potential for reference). As the defense mechanisms on the Test metal intensify, slight increases in passive oxide generation may also occur. The opposite responses occur when the Test metal becomes the cathodic member of the couple. In this case, the potential on the Test metal will tend to drop below its baseline value and may be accompanied by a small decrease in passive oxide growth since its defense mechanisms are attenuated.

In general, when an active metal is placed into an anodic state whether galvanic or environmental, its protection mechanisms will ‘kick-in’, as the metal begins to generate additional oxide to counteract the oxidizing effects. In a galvanic couple situation, the passive layer on the cathodic member may actually start dissolving since its protection requirements are moderated as the presence of an anodic member stabilizes and relaxes the cathode’s self-protective attributes. In some instances, if metal ions are available in the local solution whose reduction potential becomes greater than that of the couple *and* that of water, plating or metallization onto the cathode surface can occur (the Standard Electrode Potential for the reduction of water is $-0.83\text{V} \dots 2\text{H}_2\text{O} + 2e^- \longrightarrow \text{H}_2 + 2\text{OH}^-$).

When two metals form a galvanic couple, several electrochemical processes are occurring simultaneously as the two metals adjust to the new condition. They eventually stabilize along a plateau which characterizes the Steady State. Figure 8 depicts one of the test plots for the X750 evaluation and may serve as good representation of the coupling interaction effects involved during this study. Recall that for a galvanic coupling test, no power is applied. However, interaction between the two metals produces a very small current and potential field. The current is directed from the anode to the cathode (opposite to the flow of electrons). As seen in Figure 8, from the point where the galvanostat is turned

on, the plot resembles a response function analogous to the charging up of a capacitor ($C = A(1 - e^{-kt})$). While the rates of chemical oxidation at the anode and reduction at the cathode are always equivalent, the rates for metal recession and/or oxide growth may be different on the two surfaces. Oxide growth is induced on the anode surface but growth is subdued on the cathode. Recession into the base metal occurs only on the anode. For a static galvanic couple, the rate of acid-induced dissolution of the passive oxide into the test solution is approximately constant throughout the exposure period, keeping in mind that the specific oxide on each metal dissolves at its own rate. At some point after the metals have been in galvanic contact for a while (anywhere from a few minutes to a few hours), a Steady State is achieved as seen with the plateau regions in Figure 8.

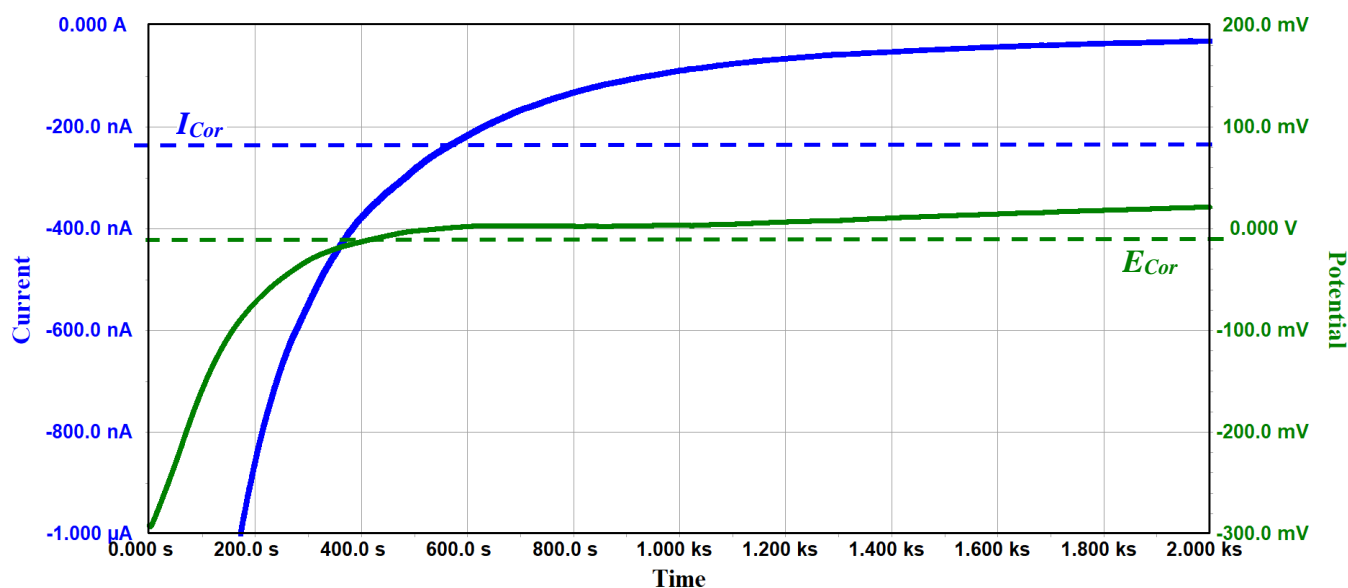


Figure 8: Galvanic couple test plot for Inconel X750 (Test) and Hastelloy C276 (Counter) in pretreat.

For this particular test run, the Inconel X750 sample (the Test metal) indicated a small level of subordination to the Hastelloy C276 sample (the Counter metal) as the resulting potential and current appeared to stabilize at levels slightly above the X750 baseline values. This could imply that the X750 was attempting to enhance or strengthen its defense mechanisms in response to the slightly superior presence of the C276. However, these changes are very small and in many runs, the changes were almost infinitesimal. Given the standards provided in NASA-STD-6012, these two metals are deemed to be very compatible. It is interesting to note that at the Steady State, the rates for base metal recession, passive oxide growth and oxide dissolution at the anode (X750) are all equal. On the cathode, the rate of oxide loss is simply equal to the dissolution rate. Thus, preexisting oxide on the cathode dissolves resulting in a negative growth rate.

The precise level of the plateau as well as the rates for oxide thickness change, recession and dissolution are dependent on the characteristics of the test solution (pH, ionic activity, polarity, etc.) and the properties of the oxide (solubility, type of bonding, heat of formation, etc.). Dissolution of the passive oxide layer on a metal surface takes place continuously as long as metal is in contact with an active solution regardless of whether the metal is isolated or coupled with other metals. Regeneration of new protective oxide (i.e., repassivation) and the corresponding recession of the base metal are driven by the dissolution

process. The reactions of dissolution occur simultaneously and in addition to any cathodic, reduction and polarization reactions which might be taking place whenever the metal is galvanically influenced by the activity of other surrounding metals.

Now for galvanic test runs where the test metal is forced into a less noble (more anodic) state under the influence of the counter metal, current is directed into the sample while electrons are flowing outward (indicated by positive current values). In these situations, the test metal is regenerating new oxide to ‘keep up’ with both the dissolution process and the cathodic influence of the counter metal. This is analogous to anodizing where the current-driven production of new oxide far outweighs the loss of oxide from dissolution. For cases where the test metal becomes more noble (more cathodic), current is directed out of the sample while electrons flow inward (indicated by negative current values). In these situations, the test metal needs less oxide for protection, so solution-driven oxide dissolution dominates as the oxide layer diminishes. This is analogous to cathodic stripping. These changes would be much larger for metal pairs with wide spreads between their E_{Cor} values such as aluminum alloys and stainless steels. For this analysis, negative current values translate into negative rates for passivation (with no base metal recession) which implies that the oxide layer is thinning out as its protection requirements are reduced. Likewise, positive currents (and rates) imply that new oxide is being generated as the process consumes base metal which recesses inward.

Table 2 gives a reduced summary of the change averages obtained during galvanic coupling analysis for all the metals evaluated thus far (as mentioned earlier, Cronidur 30 was inadvertently omitted from the analysis). The primary difference between Table 2 and the equivalent table from previous studies is that the data averages for Inconel X750 have been incorporated into the results. As opposed to polarization curve overlays which are sometimes used for galvanic compatibility analysis, this method utilizes direct one-on-one experimental measurements leading to a numerical approach for evaluating the relative compatibility attributes between the metals (although more time-consuming).

Table 2: Reduced Data Summary for Galvanic Coupling Evaluations

| Changes in Potential (V), Base Metal Recession (R) and Passivation Growth (P) Relative to Open Circuit Conditions | | | | | | | | | | | | | | | |
|---|-------------|----------|-------------------|----------------|----------|-------------------|-----------------|----------|-------------------|------------|----------|-------------------|--------------|----------|--------|
| V | R | P | V | R | P | V | R | P | V | R | P | V | R | P | |
| V _{AgCl} | mil/year | mil/year | V _{AgCl} | mil/year | mil/year | V _{AgCl} | mil/year | mil/year | V _{AgCl} | mil/year | mil/year | V _{AgCl} | mil/year | mil/year | |
| Pretreat | | | | | | | | | | | | | | | |
| Shifts in Potential and Current for the Test Metal Relative to its Original OCP | | | | | | | | | | | | | | | |
| Test Metal → | Inconel 625 | | | Hastelloy C276 | | | Titanium 6Al-4V | | | Nitinol 60 | | | Inconel X750 | | |
| ↓ Counter Metal ↓ | | | | | | | | | | | | | | | |
| Inconel 625 | | | | 0.0010 | 0.0072 | 0.0354 | -0.0164 | 0.0000 | -0.0967 | -0.0203 | 0.0000 | -0.0341 | 0.0060 | 0.0199 | 0.0921 |
| Hastelloy C276 | -0.0072 | 0.0000 | -0.0539 | | | | -0.0177 | 0.0000 | -0.1092 | -0.0148 | 0.0000 | -0.0106 | -0.0019 | 0.0160 | 0.0741 |
| Titanium 6Al-4V | 0.0431 | 0.0851 | 0.4483 | 0.0371 | 0.0928 | 0.4570 | | | | 0.0045 | 0.0013 | 0.0043 | 0.0233 | 0.0183 | 0.0847 |
| Nitinol 60 | 0.0158 | 0.0239 | 0.1156 | 0.0293 | 0.0280 | 0.1302 | -0.0097 | 0.0000 | -0.0053 | | | | 0.0126 | 0.0121 | 0.0559 |
| Inconel X750 | 0.0071 | 0.0066 | 0.0320 | 0.0168 | 0.0140 | 0.0649 | -0.0349 | 0.0000 | -0.0731 | -0.0228 | 0.0000 | -0.0514 | | | |
| Brine | | | | | | | | | | | | | | | |
| Shifts in Potential and Current for the Test Metal Relative to its Original OCP | | | | | | | | | | | | | | | |
| Test Metal → | Inconel 625 | | | Hastelloy C276 | | | Titanium 6Al-4V | | | Nitinol 60 | | | Inconel X750 | | |
| ↓ Counter Metal ↓ | | | | | | | | | | | | | | | |
| Inconel 625 | | | | -0.0021 | 0.0000 | -0.0444 | -0.0199 | 0.0000 | -0.0902 | -0.0264 | 0.0000 | -0.0341 | 0.0115 | 0.0427 | 0.1975 |
| Hastelloy C276 | 0.0452 | 0.0017 | 0.0093 | | | | -0.0449 | 0.0000 | -0.1155 | -0.0338 | 0.0000 | -0.0271 | 0.0064 | 0.0431 | 0.1994 |
| Titanium 6Al-4V | 0.0541 | 0.0750 | 0.4238 | 0.0660 | 0.0836 | 0.4120 | | | | 0.0028 | 0.0007 | 0.0023 | 0.0319 | 0.0486 | 0.2247 |
| Nitinol 60 | 0.0292 | 0.0265 | 0.1283 | 0.0463 | 0.0428 | 0.1989 | -0.0118 | 0.0000 | -0.0095 | | | | 0.0151 | 0.0461 | 0.2129 |
| Inconel X750 | -0.0055 | 0.0495 | 0.2394 | 0.0132 | 0.0651 | 0.3023 | 0.0008 | 0.0000 | -0.0406 | -0.0502 | 0.0000 | -0.0198 | | | |

Recall that currents are a measure of the rates associated with the chemical oxidation and reduction reactions occurring during the corrosion process, which are then converted into dimensional rates representing growth or loss of the passive oxide layer and corresponding recession of the base metal on the anode. In short, positive rates reflect metal recession and oxide growth while negative rates indicate dissolution of oxide. In cathodic states, oxide loss may occur but these reactions are not accompanied by any metal thickness changes so recession rates are nil.

Potential Shifts: Negative potential shifts (relative to baseline) imply that the Test Metal is noble (cathodic) to the Counter Metal as the Test Metal tends to relax its defense mechanisms. Positive potential shifts imply that the Test Metal is inferior (anodic) to the Counter Metal as the Test Metal increases its defense mechanisms to compensate.

Rate Shifts: Negative rate shifts (relative to baseline) imply that the Test Metal is less active than the Counter Metal as the rate of passivation on the Test Metal is relaxed. Positive rate shifts imply that the Test Metal is more active than the Counter Metal since the Test Metal must generate additional protective oxide in order to compensate. The rate change of base metal recession is regulated by the rate change in oxide production as more protection is required.

Overall, throughout these studies, shifts in potential and rate (or current) were quite small indicating good compatibility between the metals. It should be noted that many of these changes are often within the margin of error in which case, galvanic differences between metal pairs are essentially insignificant or irrelevant. Undoubtedly, they are well within the 250mV limit required in Table 2 of NASA-STD-6012. In conclusion, Galvanic Coupling analysis has demonstrated that Inconel X750 is galvanically compatible with all the previous metals qualified. Indeed, all of these metals are compatible with each other as the data has revealed only minute shifts in potential and oxidation rate for each metal when paired up (coupled) with each of the other metals, one at a time. The Titanium alloy seems to be the most noble of all the candidates while Inconel X750 appears to reflect properties similar to Inconel 625 and Hastelloy C276. From the previous studies, Cronidur 30 was at the bottom of the nobility ranking list and can be assumed to be about as inferior to Inconel X750 as Hastelloy C276 indicated.

3.3 Summary and Conclusions

Crevice Corrosion Evaluations:

Visual and microscopic examination of Inconel X750 samples revealed no signs of pitting, crevicing, corrosion, surface growth, discolorations, patterns or surface anomalies on any of the angled or parallel plate test assemblies on any of the surfaces in either of the subject test solutions after 6-month and 12-month immersion/storage at ambient conditions.

The appearance of all sample surfaces after 12 months was essentially identical to that for the pre-immersion surfaces. Also, neither of the test solutions indicated any signs of metal dissolution or abnormal corrosion products. Since these metals generally produce colored ions in solution, this would be further evidence that acid etching of the metal surface did not occur either locally or generally after long-term exposure to these solutions.

Potentiostatic Polarization Evaluations:

Linear and Tafel polarization tests indicated that Inconel X750 exhibited corrosion-resistance properties that were in the ‘Outstanding’ category according to industry standards. Cyclic polarization analysis revealed no tendencies for pitting or etching on X750 or any of the other metal candidates under standard testing conditions. The Titanium alloy appeared to be the best performer of all the candidates in terms of resistance to passive oxide breakdown and regeneration of the passive layer while Inconel X750 (a nickel-chromium alloy) exhibited corrosion protection properties similar to those of the other two nickel-alloys (Inconel 625 and Hastelloy C276).

Thus, it has been demonstrated that the general anti-corrosion protection properties, mechanisms for passivation, self-healing repassivation and breakdown recovery back to a stable protective state are exceptional for Inconel X750 in both test solutions. The same conclusion applies to all the previously evaluated metals. Even though Cronidur 30 sometimes indicated substandard corrosion defense properties relative to the other metals, it is still considered to be in excellent category. Overall, these results correspond well with their established nobilities indicated throughout the literature.

Galvanic Coupling Evaluations:

Galvanic Coupling analysis revealed that Inconel X750 is compatible with all of the metal candidates evaluated previously in both test solutions (as noted earlier, Cronidur 30 was mistakenly omitted from the galvanic coupling phase of the X750 evaluation). Changes in galvanic potential and oxidation rate (shifts relative to their original corrosion potential values) were very small, indicating strong compatibility attributes. These conclusions support the fact that all of these metals are close in proximity to each another at the upper end of the Galvanic Series.

Appendix

Most the topics provided in this Appendix are based on data acquired during previous evaluations of metal candidates which have already been qualified as discussed earlier. However, the analytical methods covered here were also utilized for the current candidate, Inconel X750, so the principles applied are the same. This template was generated in order to present specific concepts that are relevant or supportive to the objective of the overall ECLSS Materials Compatibility Assessment. The intent in the Appendix is to focus on the analytical, statistical and theoretical techniques which have been applied throughout all of these studies - including the Inconel X750 evaluation.

A.1 Electrochemistry Concepts

The following few sections give a brief summary of the classical methodology employed throughout industry and academia regarding the analysis of polarization techniques which have long been established to understand and evaluate DC polarization corrosion investigations. These same principles and experimental approaches have also been utilized throughout all the electrochemical corrosion studies conducted at MSFC. Sections A.1 through A.7 cover rudimentary concepts which have been well documented throughout the corrosion industry for decades and/or centuries. Parts of section A6 and then section A7 through the end of the Appendix includes discussions of concepts developed specifically from and for the more recent MSFC investigations. While many of these unique tools have been successfully applied throughout these studies, no outside collaboration or corroboration has taken place.

A.2 Test Configuration and Parameter Definition

For the situations of interest here, anodes refer to positively charged sites on an electrode (the test metal) which attract anions, while cathodes refer to negatively charged sites which attract cations. Oxidation reactions occur at the anode sites as electrons are extracted into the solution causing the sites to become positive. Likewise, reduction reactions take place at cathode sites leading to negatively charged sites. Anodes invite oxidation processes such as anodizing, passivation and rust, while cathodes facilitate reduction reactions which promote metal deposition and chemical reduction of the protective oxide layer as it tends to dissolve cathodically in the adjacent solution. Thus, during electrochemical reactions, electrons flow from anodic sites to cathodic sites while the electric current technically flows from cathodic sites to anodic sites. Once the electrical double layer (EDL) forms, anodic surfaces become negative due to the accumulation of departing electrons at the solution interface while the local interfacing solution becomes more positive as a result of dissolved metal ions.

On a larger scale, a common three-electrode test configuration was employed for this study in which electrons are supplied by the potentiostat to a counter electrode (comprised of platinum). The counter electrode polarizes the working electrode (the test sample), causing oxidation at that electrode which loses electrons to the solution. This results in an overvoltage between the working electrode and a selected reference electrode placed in close proximity to the working electrode surface. A simplified diagram of the current-voltage measurement configuration used in this work is provided in Figure A1.

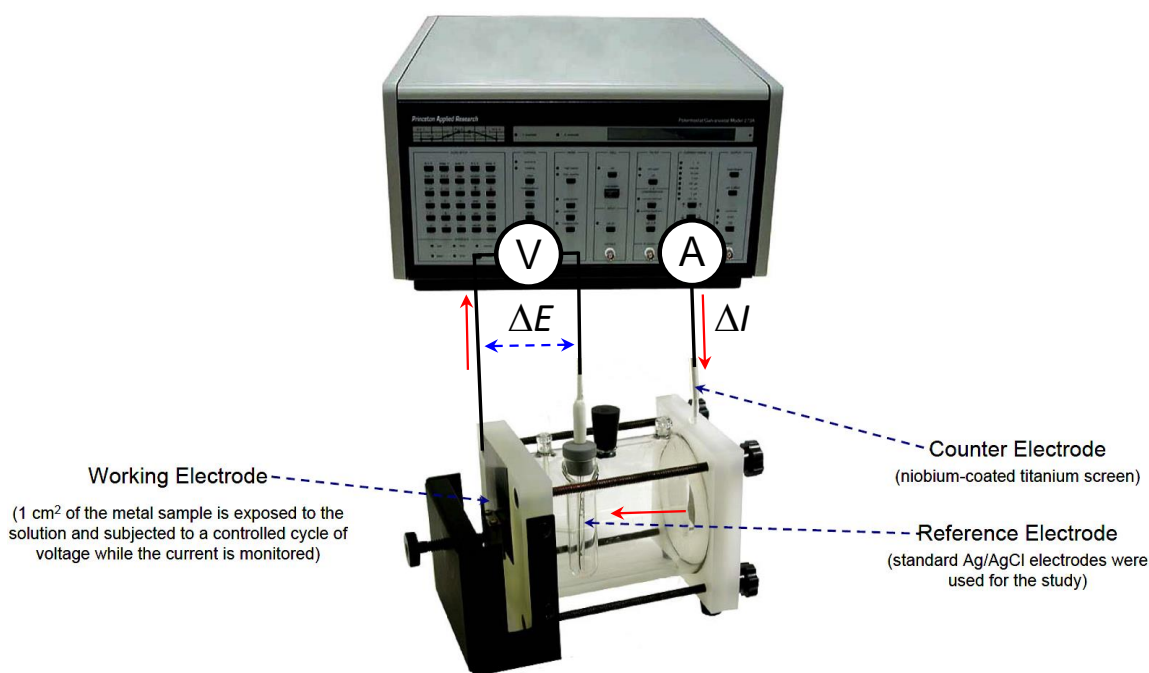


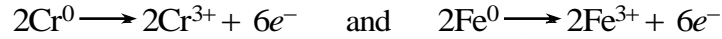
Figure A1: Simple diagram of the PAR potentiostat – and flat cell connections used in this project.

Since there is no absolute potential reference, the quantitative meaning of the measured voltage is dependent on the specific reference electrode that is used to make the measurement. The most common reference electrodes for electrochemical testing include the standard hydrogen electrode (SHE), the standard calomel electrode (SCE) and the silver/silver chloride electrode (Ag/AgCl) with the latter being used throughout these studies. In most electrolytic test cells, the resistance of the test solution skews the measurements. In order to minimize the ohmic drop due to solution resistivity, a special Luggin capillary tube was utilized which connected the reference electrode chamber to within a couple of milliliters of the sample surface. This configuration was standard as provided with the PAR Flat Cell apparatus. Also, the exposed sample test area in the flat cell configuration utilized throughout this work was exactly 1 cm^2 . With this understanding, the terms current and current density are sometimes used interchangeably.

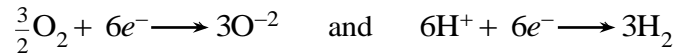
Within the test cell and throughout every DC polarization test cycle, the current is always directed from the counter electrode to the working electrode (the sample) while electrons are always flowing out of the working electrode. If a small voltage E is applied that is below the OCP (or E_{OC}), the sample becomes cathodically charged with an excess of electrons and a corresponding cathodic current I_c . This overpotential can be represented as $\eta = E - E_{OC}$. As the applied voltage is increased back toward E_{OC} (which is representative of E_{Cor}), the sample becomes less cathodic and the outflow of excess electrons diminishes. This is not chemical oxidation since the departing electrons are provided by a pool of excess conduction electrons, not valence electrons. At E_{Cor} , the net electron flow becomes zero as the anodic and cathodic currents are exactly equal. When the voltage continues above E_{Cor} , valence electrons begin leaving the sample which changes polarity and starts to anodically oxidize as it is driven by the anodic current I_a . In either case, the sample becomes polarized when its potential is forced away from its equilibrium value at OCP and the net current I_{net} becomes a mixture of I_c and I_a .

A.3 The Polarization Curve

At the steady state defined by E_{Cor} , the net current is zero since $I_a = I_c$. On either side of zero, I_a is difficult to measure directly. This current is also referred to as the exchange current I_e , (equivalent to I_{Cor}) which is a measure of the rate of electron transfer from metal to either oxygen molecules, hydrogen ions or other electrophiles within the test solution. The exchange or corrosion current is proportional to the oxidation rate (the corrosion rate) at the steady state where equilibriums exist between oxidation of metal atoms at anodic sites,



and reduction of molecular oxygen and/or hydrogen ions at cathodic sites,



Since the forward oxidation and reduction rates cancel each other at E_{Cor} , it becomes impossible to directly determine I_e or I_{Cor} as well as the desired recession, corrosion and oxide growth rates. Beyond about 50mV on either side of I_{Cor} , the process becomes dominated by either the anodic or cathodic reactions. These concepts are illustrated in Figure A2 showing a linear polarization data plot (in blue) for one of the Cronidur 30 samples (a high Fe-Cr alloy) which was conducted from -15V to +15V (vs. Ag/AgCl) relative to the OCP in brine solution. As will be demonstrated shortly, linear polarization techniques permit the determination of I_{Cor} and hence the desired oxidation/recession rates.

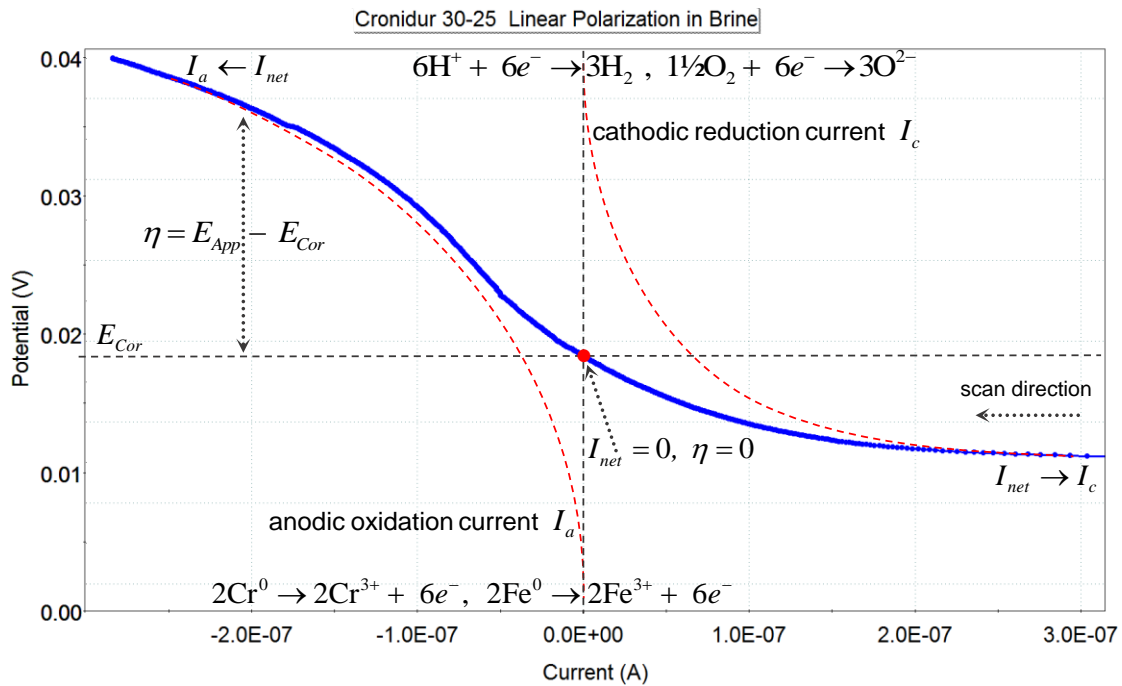


Figure A2: Current versus potential plot for one of the Cronidur samples showing anodic and cathodic branches.

Molecular congestion caused by the concentration of reactants and products along the metal-solution or oxide-solution interface may limit the current (and the transfer of electrons) since entities entering and leaving the reaction sites must diffuse through a thickened layer of solutes, reactants and products in a mass-transfer process across the adjacent solution. This is often referred to as ‘concentration polarization’ and the redox reactions are said to be diffusion-controlled. This should not be confused with the type of diffusion that occurs within the barrier and porous layers where other factors contribute to or affect the ion transfer process. The interfacial solution region of heavy concentration is referred to as the Nernst diffusion layer which can vary in thickness, composition, diffusivity and current-limiting attenuation anywhere along the polarization curve, or it may not be significant at all if the reactions are activation-controlled. Activation polarization is predominant when the redox reactions are not impeded by diffusional phenomena but proceed strictly in a charge-transfer process. In many cases, the actual process may be a mixture of activation and concentration polarization.

The symmetry of the anodic and cathodic segments relative to the point E_{Cor} , $I_{net} = 0$ in Figure A2 may imply a small level of diffusion-controlled processes in the anodic region (where the passive layer is re-forming). A symmetry coefficient of 0.5 for both branches indicates an ideal activation-controlled situation which gives a perfect *sinh* curve form. The flat cell configuration in heated solution was pursued in this study in accordance with conditions utilized in previous studies. A rotating test sample would have facilitated a more uniform Nernst layer thickness with improved results. The apparent symmetry effects noted in Figure A2 may be more reflective of diffusional influences associated with the transport of species across the porous and barrier layers rather than concentration-limited transport within the adjacent solution. While the restricted transport of species through the fixed barrier and porous layers would likely be a combination of Darcy flow and Fickian diffusion, transport through the mobile Nernst layer would be exclusively Fickian in nature in accordance with Fick’s first law. However, widespread diffusional attenuations in this work appeared to be minimal in many cases.

A.4 The Butler-Volmer Equation

Examination of all the linear, Tafel and cyclic plots generated for this study indicated that the majority of redox reactions occurring in both branches for all six metals was heavily influenced by activation-dominated processes. Figure 5 in the body of the report actually gives a plot of the well-known Butler-Volmer (BV) equation^[5] which is applicable to activation-controlled redox reactions occurring on the same electrode. The BV equation expresses the measured current density I_{net} in terms of the exchange current density I_e ($\equiv I_{Cor}$), the overpotential $\eta = E_{App} - E_{OC}$ (or $E - E_{Cor}$), the number of electrons transferred during the redox reactions n , the cathodic and anodic symmetry coefficients s and $(1 - s)$ respectively, the absolute temperature T (which is $37^\circ\text{C} = 310\text{K}$ for our study), the gas constant $R = 8.314 \text{ Jmol}^{-1}\text{K}^{-1}$) and the Faraday constant $F = 96,485 \text{ C-Vmol}^{-1} \dots$

$$I_{net} = I_c + I_a = I_c - |I_a|$$

$$I_{net} = I_e \exp\left(\frac{-snF}{RT}\eta_c\right) - I_e \exp\left(\frac{(1-s)nF}{RT}\eta_a\right) \quad (1)$$

Note: The negative sign for the anodic current is due to physics sign conventions. For single metal polarization, the current is always flowing from the counter electrode to the test metal regardless of whether it is in the cathodic or the

anodic region. The current in these configurations is understood to be positive throughout. However, in two metal galvanic coupling configurations, the current can flow in either direction depending on which metal is the cathode and which is the anode. As will be shown later, the direction of current flow in these situations has special significance.

The left term in Eq(1) defines the cathodic current while the right term defines the anodic current. Together, they make up the entire polarization curve. To be precise, this expression would contain terms for each reaction occurring in the process but is shown in this incremental form for simplicity as it may apply to either redox reaction set indicated in Figure A2. If the overpotential η is greater than about $\pm 50\text{mV}$ in either direction, one term dominates while the other becomes insignificant. Thus, the currents in the cathodic and anodic branches for large overpotentials are described respectfully by . . .

$$I_c = I_e \exp\left(\frac{-snF}{RT} \eta_c\right) \quad \text{and} \quad I_a = I_e \exp\left(\frac{(1-s)nF}{RT} \eta_a\right) \quad (2)$$

These expressions can be rearranged to give the well-known Tafel parameters for each branch. For the cathodic current . . .

$$\begin{aligned} \ln(I_c) &= \ln(I_e) - \frac{snF}{RT} \eta_c \\ 2.303 \log_{10}(I_c) &= 2.303 \log_{10}(I_e) - \frac{snF}{RT} \eta_c \\ \log_{10}\left(\frac{I_c}{I_e}\right) &= -\frac{snF}{RT} \eta_c \end{aligned}$$

from which . . .

$$\eta_c = \beta_c \log_{10}\left(\frac{I_c}{I_e}\right) \quad (3)$$

where the cathodic Tafel constant in volts is defined . . .

$$\beta_c = -\frac{2.303RT}{snF} = -\frac{0.0262}{sn}$$

Using Figure A2 as a rough guideline, if we let $n = 3$ and $s = \sim 0.75$, (where $s_c + s_a = 1$), the value of $|\beta_c|$ comes out to 116 mV/decade compared to a value of 142 mV obtained for this particular sample during the experimental Tafel test run. Likewise, the anodic current becomes . . .

$$\ln(|I_a|) = \ln(I_e) + \frac{(1-s)nF}{RT} \eta_a$$

which leads to . . .

$$\eta_a = \beta_a \log_{10}\left(\frac{|I_a|}{I_e}\right) \quad (4)$$

where the anodic Tafel constant is defined . . .

$$\beta_a = \frac{2.303RT}{(1-s)nF} = \frac{0.0262}{(1-s)n} = 349 \text{ mV/decade}$$

This compares to a value of 416 mV obtained for this sample during the actual Tafel test run. Admittedly, there was a wide variation in the Tafel constant values determined throughout this work. Thus, in order to obtain good representative averages for each of the data components under investigation, many test runs and test repeats have been incorporated into the experimental plans for every metal and series of metals evaluated thus far.

Now the Tafel expressions Eq(3) and Eq(4) are the so-called high-field approximations and can be written in slope-intercept form for future use . . .

$$\eta_c = a_c + \beta_c \log_{10}(I_c) \quad \text{where } a_c = -\beta_c \log_{10}(I_e)$$

and

$$\eta_a = a_a + \beta_a \log_{10}(|I_a|) \quad \text{where } a_a = -\beta_a \log_{10}(I_e)$$

By definition, β_c and β_a are the activation-controlled cathodic and anodic Tafel slopes or ‘beta’ values respectively and will become important parameters during Tafel analysis. Note that β_c represents a negative (cathodic) slope while β_a is a positive (anodic) slope.

And finally, the BV equation can be written in a more concise form . . .

$$I = I_{Cor} \left[\exp\left(\frac{2.303\eta}{\alpha_a}\right) - \exp\left(\frac{2.303\eta}{\beta_c}\right) \right] \quad (5)$$

where $\eta = E - E_{Cor}$ can represent the overvoltage in either direction.

A.5 Faraday’s Law and Oxidation Rates

At the Steady State, oxidation and reduction rates are equal and the current associated with either reaction (the exchange current or so-called corrosion current $I_e = I_{Cor}$) is a direct measure of the rates for these reactions. With strongly passivating metals such as the ones under evaluation here, I_e can be translated into the rates for base metal recession (penetration depth) and oxide thickness growth. While chemical reaction rates measure the mass quantity of products generated, recession and growth rates are volumetric in dimension. They share the same number of transferred electrons but different geometrical densities which results in unique weight and volumetric changes associated with recession into the base metal and the accompanying oxide growth which then occupies both the recessed metal volume and a certain protrusion height above the original metal line. While the total oxide volume occupies both of these areas, its height above the original metal surface is often the parameter of interest.

Since I_e (and hence the dimensional rates) cannot be measured directly they must be surmised by one of the linear methods covered in the next section. Once the exchange current is ascertained, a

modification of Faraday's famous law can be used to estimate the rates associated with weight and volume changes during the oxidation process. The premise can be stated that for a given reaction, the current I is directly proportional to the sample weight gained or lost over time W_{Δ}/t , as well as the number of electrons n transferred during the reaction, and is inversely related to the molecular weight M_w of the electroactive species involved, where F is Faraday's constant . . .

$$\frac{IM_w}{nW_{\Delta}/t} = F$$

Recognizing that M_w/n is the equivalent weight W_{Eq} of the reacting species and utilizing its density ρ , weight and volume changes can be written respectfully in terms of the associated current, the equivalent weight and the density . . .

$$\frac{W_{\Delta}}{t} = I_{Cor} \frac{W_{Eq}}{F} \quad \text{and} \quad \frac{V_{\Delta}}{t} = I_{Cor} \frac{W_{Eq}}{F\rho}$$

The second expression is of importance in our study as it will permit determination of the respective metal recession and oxide growth rates k_{Met} , k_{Ox} (both volumetric rates). By ascertaining the measured current, the equivalent weight of the base metal and composite oxide (which may be comprised of many components), and the mass density of the composite oxide, these rates become . . .

$$k_{Met} = I_{Cor} \frac{W_{Eq,Met}}{F\rho_{Met}} \cdot c \quad \text{and} \quad k_{Ox} = I_{Cor} \frac{W_{Eq,Ox}}{F\rho_{Ox}} \cdot c \quad (6)$$

where c is a conversion factor incorporated to express the rates in the desired units.

For this study, weight constituents are given in grams and densities in g/cm^3 while the rates reported throughout this work are often given in Angstroms per day ($\text{\AA}/\text{day}$) and mils per year (mil/year) whose c values are respectfully, $8.9588 \times 10^7 \text{ Eq-sec-}\text{\AA}/\text{C-cm-day}$ and $1.2874 \times 10^5 \text{ Eq-sec-mil}/\text{C-cm-yr}$. While the number of exchange electrons transferred from the metal must exactly equal the number of electrons transferred to the oxide, the equivalent weights (and volumes) of these two phase are definitely not equal. During the course of these studies, special approaches were formulated for estimating the W_{Eq} associated with the base metals *and* their corresponding composite oxides. Of particular interest here is determination of the oxide W_{Eq} values which is unconventional. These concepts will be covered later.

A.6 Estimation of Currents and Rates

Before leaving Figure A2, one last concept should be explored centering on the point E_{Cor} at $I = 0$ (the red marker). Below E_{Cor} , the sample acts as a cathode, above E_{Cor} , the sample becomes an anode as it changes polarity. A technique developed by Stern and Geary (SG) many years ago provides a simple approach for estimating the exchange current (density) and hence, the rates for corrosion, metal recession and oxide growth. They introduced the term of 'polarization resistance' R_{Pol} (or R_{Cor}) in analogy to Ohm's

law or more precisely, they demonstrated that an inverse relationship exists between I_{Cor} and R_{Cor} when very small overpotentials are applied relative to E_{Cor} (scan ranges such as -20mV to $+20\text{mV}$ or smaller are typical) and that the slope of the polarization curve in this region $dE/dI = R_{Pol}$ describes a straight line as it passes through $I_{Cor} = 0$ (for cases with minimal linearity, the tangent line at this point can be used). Their work resulted in the following simple but very useful relationship . . .

$$I_{Cor} = \frac{B}{R_{Cor}} \quad (7)$$

where B is a proportionality parameter based on the Tafel constants in units of volts.

Historically, the SG equation has been utilized and experimentally validated many times since its introduction in the early 1900's. Validation of this approach can also be demonstrated mathematically through its relationship with the BV equation, and then the constant B can be determined. Utilizing the series expansion identity, $e^x = 1 + x + x^2/2! + x^3/3! + \dots$, and neglecting the higher terms for low overpotentials, Eq(5) can be written and rearranged . . .

$$I = I_{Cor} \left(\frac{2.303\eta}{\beta_a} - \frac{2.303\eta}{\beta_c} \right)$$

from which . . .

$$\frac{dI}{dE} = 2.303(\beta_a^{-1} - \beta_c^{-1})I_{Cor} \quad \text{where we let } \eta = dE \text{ and } I = dI$$

and then . . .

$$I_{Cor} = \frac{1}{2.303} \left(\frac{\beta_a \beta_c}{\beta_a + \beta_c} \right) \frac{dI}{dE} = \frac{B}{R_{Cor}}$$

where . . .

$$B = \frac{1}{2.303} \left(\frac{\beta_a \beta_c}{\beta_a + \beta_c} \right)$$

The SG method is the so-called low-field approximation since only a very small scan range is applied. The approach is based on the assumptions that (a) all the reactions are reversible, (b) they are activation-controlled, (c) the energy barriers for the forward and reverse reactions are symmetrical, and (d) the results pertain only to general corrosion/oxidation events, providing no information regarding activity associated with localized pitting or crevice corrosion. The range of applied potential is so small that the test is nondestructive and results are obtained very quickly. This method is useful for long-term continuous corrosion monitoring in field structures. An example of the SG technique applied to one of the Hastelloy C276 samples in Concentrated Pretreat solution was given in Figure 5 earlier and is reproduced here for convenience in Figure A3.

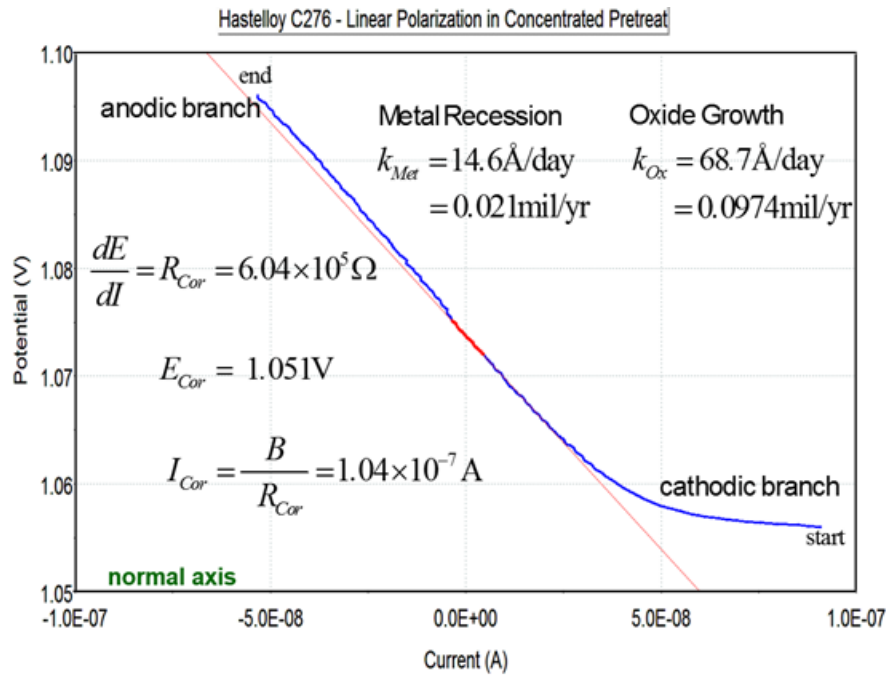


Figure A3: Linear polarization test plot and analysis for Hastelloy C276 in Concentrated Pretreat.

Again, the total oxide thickness includes recession depth plus outward growth. The Tafel constants applied to the Linear calculations in A3 were taken from subsequent Tafel testing. Note that the plot in Figure A3 utilizes normal ordinate or linear axes for both dimensions. If this same data were re-plotted in semi-log form, converting the x axis (the current) into the corresponding \log_{10} values, a low-field Tafel plot would be obtained. Thus, a Tafel test run is essentially a Linear test that is applied over a wider potential range and plotted on semi-log axes. Since the Current (or x -axis) can often change magnitude over several orders in a single run, the log version of this data field is useful for examining variations in the plot. It is standard industry practice to plot both Tafel and Cyclic data on semi-log axes during each experiment run. Later on, it will be shown how specialized information can be extracted from just the normal Tafel and Cyclic plots, but for the present, classical Tafel evaluations utilizing the SG and BV approaches are provide an abundance of information, including the rates for corrosion, recession and passivation. An example of one of the Tafel experiments with analysis was given in Figure 6 earlier and is reproduced here for convenience in Figure A4.

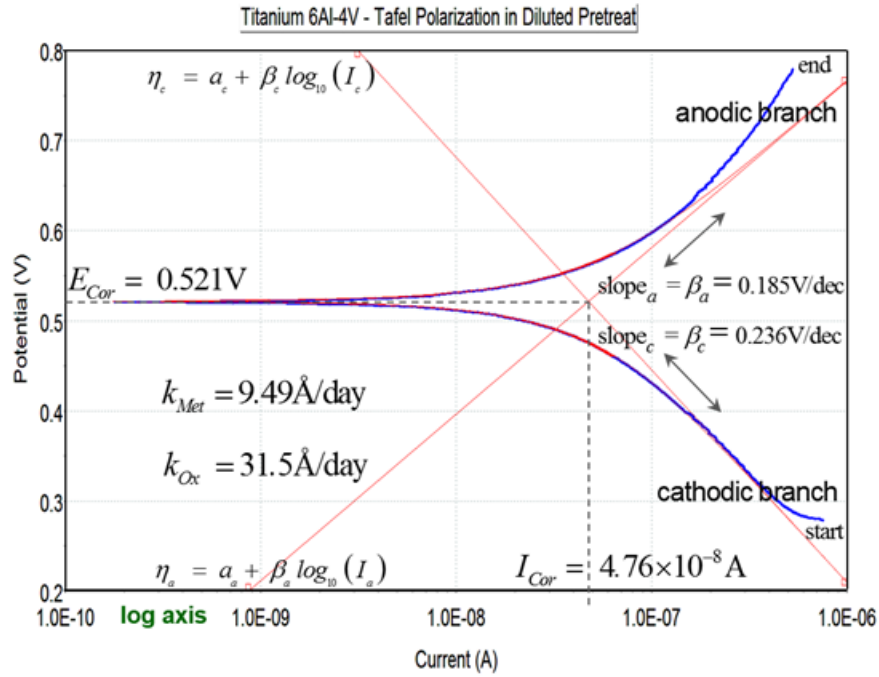


Figure A4: Semi-log Tafel polarization test plot and analysis for Titanium 6Al-4V in Diluted Pretreat.

In practice, a typical Tafel test run is scanned over a wider potential range than Linear scans in order to capture a greater portion of the anodic and cathodic branches. In this format, $I_{Cor} = 0$ coincides with the log inflection point and provides the key to determining all the other critical parameters in the Tafel plot. In essence, both of these techniques can be considered linear polarization, and they both provide essentially the same results. However, when the semi-log version is utilized, the Tafel method utilizes a different analytical approach by applying linear fits along the straight portions of each branch, which together form a basic Evans diagram, and whose intersection analytically identifies both E_{Cor} and I_{Cor} , and then the desired recession-oxidation rates can be computed from I_{Cor} . This approach is illustrated in Figure A4. For the UWMS study, in all cases, the results obtained from Linear analysis were essentially identical to those derived from Tafel analysis. Thus, the two techniques employ different approaches for analysis but provide complimentary outcomes that reinforce the confidence level of the data obtained.

The primary dominating metal constituents in the three alloy candidates evaluated in this study included Titanium (Ti) in the Titanium 6Al-4V candidate, and Chromium (Cr) and Nickel (Ni) in both the Inconel 625 and Hastelloy C276. While a number of reactions are possible with the alloying components, the fate of primary constituents within acidic media will generally involve oxidation of the metal, reduction of hydrogen ion and molecular oxygen, precipitation of the metal oxide and hydrolytic dissolution of the oxide in the acidic test solution. These processes are illustrated in Figure A5 for the three metal constituents of interest.

Unless noted or apparent, analytical proposals, theories, mechanisms and illustrations from this point on are the perception and handiwork of the author with no outside corroboration. Correctness or accuracy has not been confirmed.

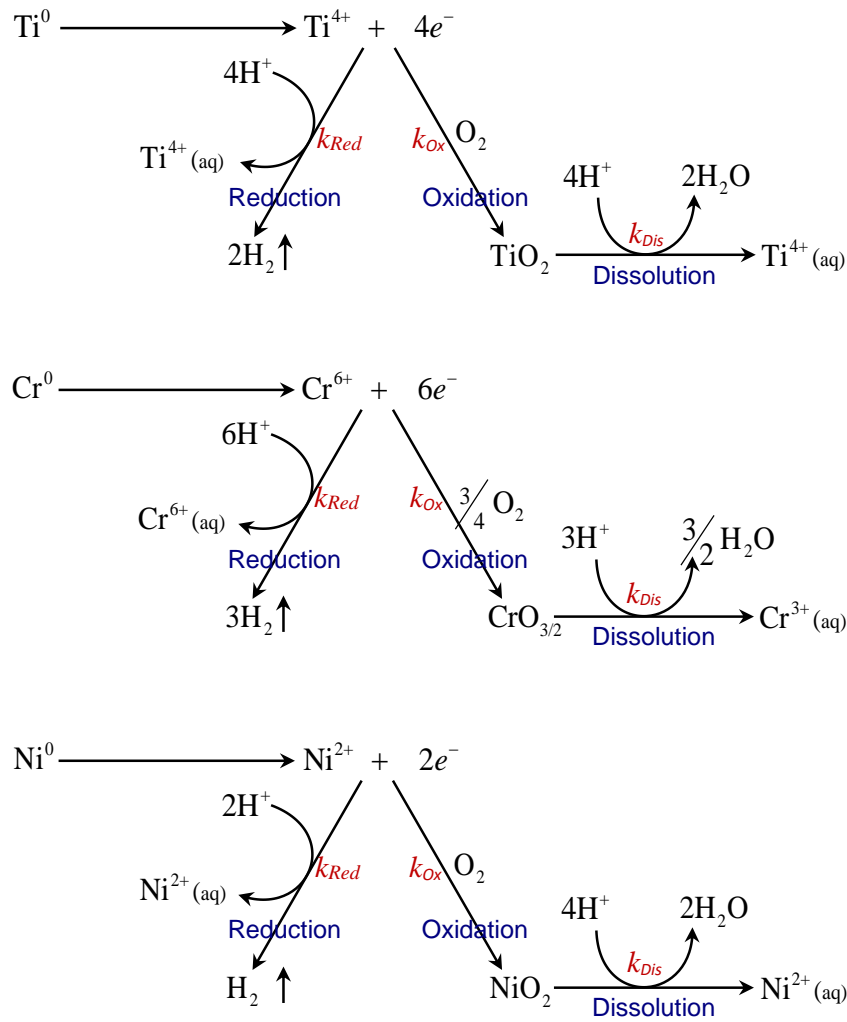


Figure A5: Possible pathways of Titanium, Chromium and Nickel in acidic solution.

Figure A5 depicts a simplified summary of the reactions for oxidation, reduction and dissolution across the metal-oxide/hydroxide-solution interface for the three metals of interest in this study, Ti, Cr and Ni. The diagrams illustrate the specific reactions associated with (A) the reduction of H^+ to form H_2 (resulting in a pH increase), (B) oxidation of the base metal to form its passive oxide utilizing aqueous oxygen within the media, and (C) dissolution of the passive oxide product via acid hydrolysis which ejects metal ions into the solution. At a Steady State equilibrium condition, the rates for oxidation, reduction and dissolution are all equal, $k_{\text{Ox}} = k_{\text{Red}} = k_{\text{Dis}}$. Under dynamic anodic conditions, electrons are flowing out of the metal-oxide system as the rate of metal oxidation increases which in turn increases the rate of passive oxide generation while the rate of steady state oxide dissolution remains about the same. During cathodic situations, electrons are flowing into the metal-oxide system. In this case, oxidation of the base metal does not occur so the rate of oxide generation either becomes dormant or goes negative as it begins to undergo reduction, resulting in the production of water and molecular hydrogen as the rate of steady state dissolution remains about the same. However, the removal of oxide is greatly accelerated as it undergoes both reductive dissolution and hydrolytic dissolution resulting in cathodic stripping of the

oxide. In any given cathode-anode situation, if the pH of the media decreases (becoming more acidic), the rate of oxide dissolution increases which in turn increases the rate of oxide generation and base metal oxidation. Conversely, these decrease as the pH becomes less acidic.

A.7 Analysis of Cyclic Polarization Curves

Information pertaining to general corrosion and oxidation is obtained during the linear methods previously covered. While general corrosion/oxidation aspects can be acquired or substantiated during subsequent cyclic test runs, the most valuable information obtained is related to the tendency for corrosive pitting, crevicing or etching. In general, cyclic polarization is a destructive test as the surface of the sample is disturbed, sometimes with visible results. Most cyclic polarization test runs start out by applying a linearly increasing voltage ramp that begins in the negative cathodic area (same as a Tafel scan), increasing through the Tafel region and then up into the anodic region, beyond the passivation zone and through the breakdown potential of the passive oxide to a pre-selected potential where the voltage scan reverses as it ramps back down toward the cathodic region. A hysteresis loop is usually generated. Several key points and regions are realized in the cyclic scans conducted on the subject metals.

- (a) E_{Cor1} – As covered earlier. This is the primary polarity switching point from cathode to anode when passivation just begins during the up-scan and pertains to general corrosion/passivation.
- (b) The Tafel region – As covered earlier, E_{Cor1} and I_{Cor} are represented by the intersection of the Tafel beta line slopes pertaining to possible general corrosion/oxidation events.
- (c) E_{Pas} – The primary passivation potential taken at the apex (the tangent) of this curve section provides E_{Pas} and sometimes I_{Pas} which represent the maximum passivation potential and passivation rate attained before oxide growth begins to end or level off.
- (d) The passive region or plateau – The passive oxide may strengthen a little after passing through E_{Pas} but then weaken with possible metastable pitting as the breakdown point is approached.
- (e) E_{Brk} – The oxide breakdown potential is analogous the dielectric strength of the oxide and pertains to the point where the oxide structure can be breached possibly followed by pitting initiation or general etching (depending on the solution composition). Behavior of the plot just after E_{Brk} may be indicative of the metal's susceptibility to pitting/etching initiation.
- (f) E_{Ver} – The scan reversal potential or so-called vertex is a user-selected point where the increasing voltage ramp reverses and begins to decrease (same rate as the up-ramp). Behavior of the plot just after E_{Ver} can provide unique insight regarding the metal's repassivation capability to provide protection against sustained pitting or etching.
- (g) E_{Rep} – The repassivation potential is represented by the apex of the return curve where repassivation is winding down and the recovery process is near completion. Techniques to surmise maximum rates for pitting penetration and repassivation growth will be discussed later.

The repassivation region provides further information regarding the repassivation process and the degree of protection attainable. The direction and area of the hysteresis loop reflects the strength or robustness of the metal's self-protection mechanism against sustained pitting. For strong passivating metals, the instant E_{Ver} is passed, any signs of possible pit initiation immediately vanish as the metal rapidly begins repassivation, oxide regeneration and system recovery at a maximum repassivation rate.

(h) E_{Cor2} – This is the polarity switching point from anode back to cathode during the down-scan after repassivation is complete. Pertains to general corrosion/oxidation and general repassivation.

Cyclic plots and graphical analysis for one of the Hastelloy and Cronidur samples are given in Figures A6 and A7 as examples to help illustrate some of these parameters and concepts.

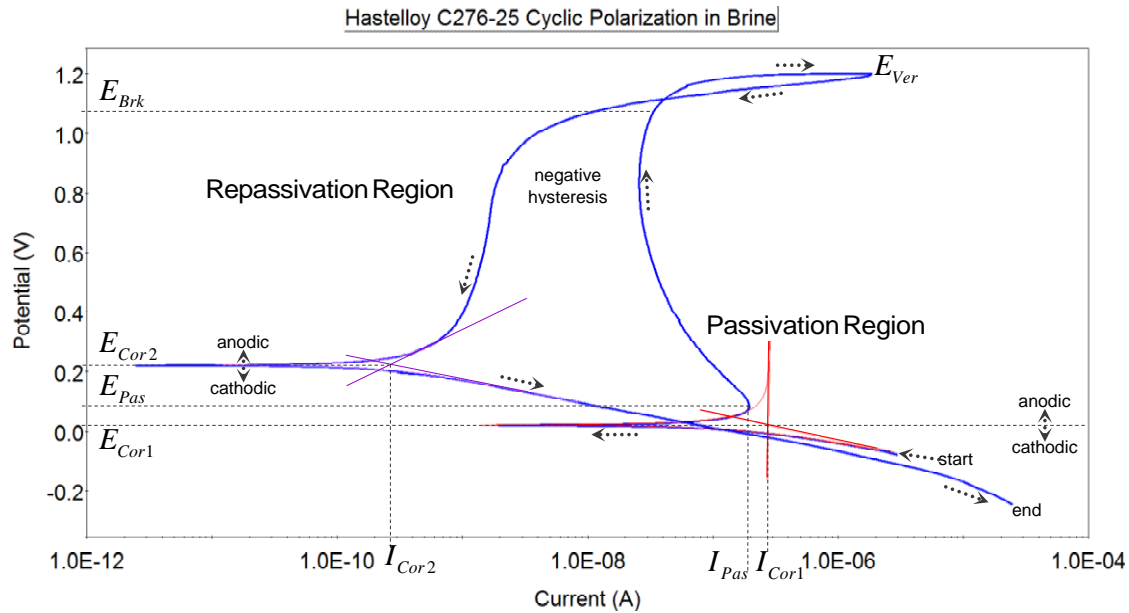


Figure A6: Cyclic polarization test results and analysis for Hastelloy in brine.

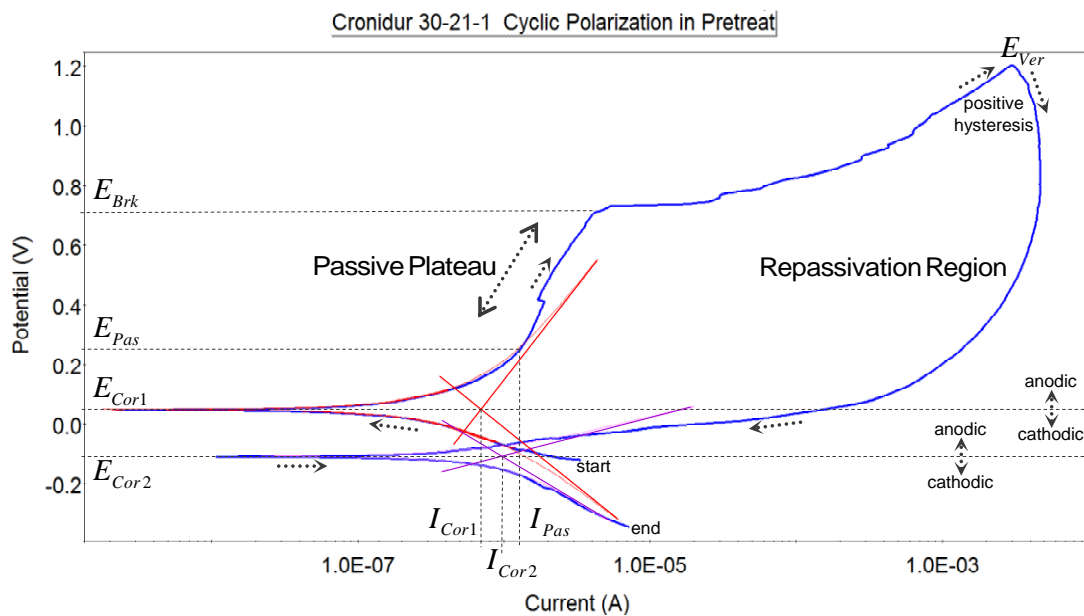


Figure A7: Cyclic polarization test results and analysis for Cronidur in pretreat

The cyclic curve form displayed for Hastelloy in Figure A6 is reflective of most of the plots for the other Hastelloy samples as well as most the Inconel samples in both solutions. It also bears significant similarity to most of the Titanium plots. While the Cronidur plots contain the same parameters, regions and points, the curve shapes and ranges were notably different than the other metals. Approaching E_{Brk} , metastable pitting becomes possible. Between E_{Brk} and E_{Ver} , the oxide might be compromised and active pitting could be taking place. After passing E_{Ver} , the oxide either (a) repairs itself very rapidly and all vestiges of pitting completely vanish or (b) the oxide repairs itself slowly while sustained (or metastable) pitting attempts to survive. Case (a) describes all the Inconel, Hastelloy and Titanium samples where the slope of the curve following E_{Ver} immediately rebounds as the current decreases sharply and the repassivation forces completely overwhelm any possible traces of pitting that may have existed. This also results in negative hysteresis (since the down-ramp data is now tracking behind the up ramp).

On the other hand with case (b), there is a forward component observed in the Cronidur plot just after E_{Ver} is passed (positive hysteresis) which implies that pitting may still be occurring after the voltage reversal point. This is depicted in Figure A7. In general, E_{Ver} is likened to a sort of relief point in the voltage-driven breakdown process where a robust self-repairing mechanism has the opportunity to swiftly rebuild broken structural links in the oxide lattice, but Cronidur shows weaknesses in this aspect with a very high positive hysteresis area. Thus, negative hysteresis implies strong repassivation protection forces while positive hysteresis is indicative of poor pitting protection. This is one of the primary differences between Cronidur and the other metals. There are other disparities.

Note: Many of the techniques and concepts introduced in this and the following sections were empirically developed as extensions to ASTM G102 and may be considered as original approaches for evaluating and characterizing corrosion, pitting and oxidation phenomena. While these techniques have seemed to work well throughout these studies, no guarantee can be given regarding their validity or accuracy in other applications.

The higher the potential required to locally damage or breakdown the passive oxide E_{Brk} , the higher the resistance to pitting. Consider the potential height of E_{Brk} or rather the potential difference between E_{Brk} and the primary passivation potential E_{Pas} in Figures A6 and A7. For the Hastelloy sample, the difference $E_{Brk} - E_{Pas}$ is over one volt, while this same distance on the Cronidur plot is about a half a volt. In the pretreat test solution, this potential ranged from about 800-900mV for the Inconel, Hastelloy and Cronidur samples. In the Brine test solution, a similar range was obtained for the Inconel and Hastelloy samples but the Cronidur samples were lower, ranging from about 400-700mV. The Titanium materials ranged from about 1300-1500mV in both solutions. These results tend to support the evidence that Cronidur is relatively more susceptible to pitting in the brine solution than the other metals and that all the Titanium metals are superior in both solutions. The potential difference $E_{Brk} - E_{Pas}$ provides insight regarding the tendency of pits to form that is, the susceptibility of pitting initiation which is a unique characteristic for each of these metals. Special methods for estimating initiation and sustainment susceptibilities are covered later.

Now, examine the relative locations of E_{Cor1} and E_{Cor2} with respect to the potential axis in Figures A6 and A7. Note that E_{Cor1} (same as E_{Cor} in previous discussions) and E_{Cor2} are both dominated by general corrosion effects, but E_{Cor2} may also be influenced by events associated with pitting which can lead to a general repassivation regeneration process terminating at E_{Cor2} . Also, recall that E_{Cor1} marks the beginning of the primary passivation process when the sample switches from cathode to anode and oxide growth accelerates in order to protect the metal from the solution, while E_{Cor2} marks the end of the repassivation growth process after the oxide has completed all the rebuilding and repair steps, switching from an anode

back to a cathode. The higher that E_{Cor2} is on the potential axis (and the closer it is to E_{Brk}), the sooner the oxide regeneration process is completed and the more resistant the base metal becomes to general and pitting corrosion, even though it is adequately protected well before reaching E_{Cor2} . Nevertheless, note that for the Hastelloy plot, E_{Cor2} is higher than E_{Cor1} while on the Cronidur scan, E_{Cor2} is lower than E_{Cor1} . Indeed, for all the Inconel, Hastelloy and Titanium samples, E_{Cor2} is above E_{Cor1} , but for all the Cronidur scans, E_{Cor2} is below E_{Cor1} in both solutions. For most of the Titanium samples in this study, E_{Cor2} was very high and very close to E_{Brk} , further supporting the premise that Titanium and its alloys are extremely resistance to both pitting and general corrosion in these solutions.

A.8 Semi-Log vs. Normal Cyclic Polarization Plots

Behavior of the curve in the E_{Brk} - E_{Ver} - E_{ReP} region is critical. If the experimental scan is tailored appropriately so that the E_{Brk} region is captured well below E_{Ver} , the net current along the slopes preceding and following E_{Ver} can be evaluated. Along the slope preceding E_{Ver} , the current balance may be dominated by pitting tendencies (which would result in recession into the base metal). At maximum pitting, this current might correspond to a resistance R_{Pit} . Along the slope following E_{Ver} , the current may be dominated by repassivation (oxide regeneration) with a resistance R_{ReP} . Since E_{Brk} is associated with R_{Pit} and E_{ReP} is associated with R_{ReP} , the following rudimentary expressions can be suggested . . .

$$\left| \frac{dE}{dI} \right|_{Pit} \sim R_{Pit} \sim \frac{E_{Brk}}{I_{Pit}} \quad \text{and} \quad \left| \frac{dE}{dI} \right|_{ReP} \sim R_{ReP} \sim \frac{E_{ReP}}{I_{ReP}}$$

These ideas are illustrated in Figure A8 for one of the Inconel 625 samples showing how characteristic values for E_{Pit} , and E_{ReP} can be acquired along with semi-quantitative representations for the maximum pitting rate and the maximum repassivation rate via slope and tangent analysis using the normal plots. These concepts allow estimation of some other quantities which could be helpful in assessing the anti-corrosion properties in this critical region along the cyclic polarization plot. For instance, the ratio of the rates for repassivation to pitting could indicate relative differences between the metals regarding their abilities to ‘recover’ after passing through breakdown and repassivating. We can define this simple quantity as the Breakdown Recovery Ratio . . . $BRR = k_{Rep}/k_{Pit}$. The BRR factor has been employed throughout most of these studies to provide corroborating support and perhaps help improve insights into the relative properties of the metal candidates investigated.

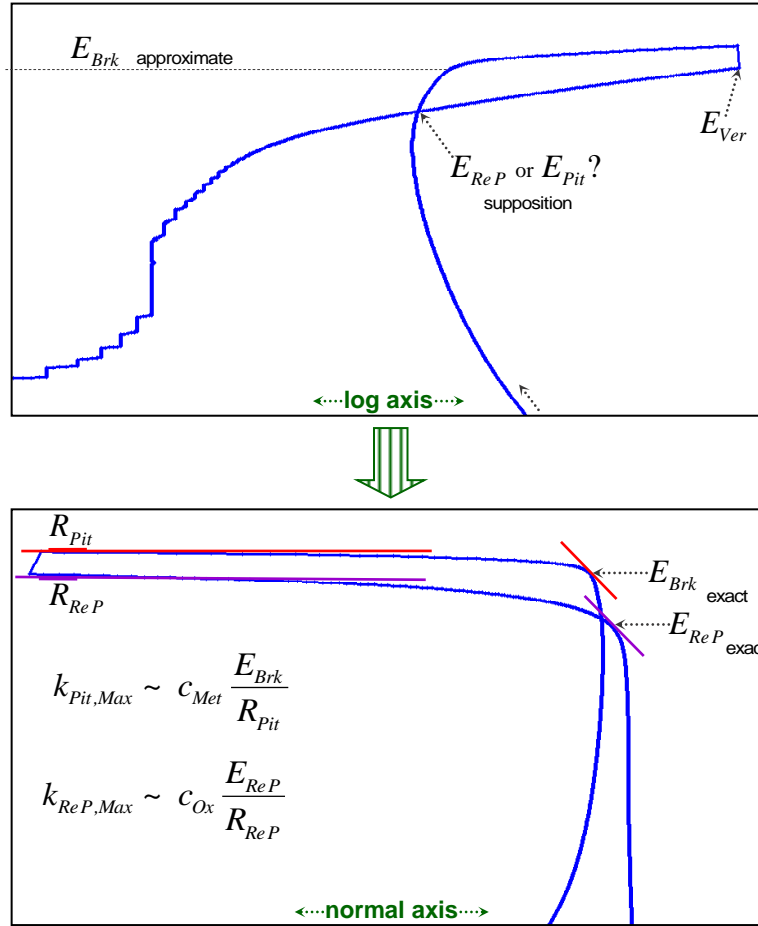


Figure A8: Method for evaluation of critical pitting and repassivation parameters using semi-log and normal plots.

Note from Figures A6 and A7, the point representing E_{Brk} is skewed in semi-log space while E_{ReP} is not visible at all. In the normal log plots shown in Figure 8, the tangent points for both E_{Brk} and E_{ReP} are precisely defined. On typical semi-log cyclic plots, the intersection of the scan lines is often misinterpreted by many workers to represent the pitting or repassivation current. For most of the Cronidur samples, the maximum pitting rate exceeded the maximum repassivation rate, but for all the other metals, any possible inclinations for pitting were completely subdued by the oxide regeneration process almost instantly after reversal. Indeed, physical pitting into the base metal of these samples likely never even occurred while base metal pitting on the Cronidur samples could be significant. As revealed during the earlier evaluations, pitting was visibly evident in many of the Cronidur samples after cyclic polarization especially under extended test conditions. With the exception of Cronidur, none of the other metals evaluated thus far have indicated any signs of pitting either visibly or during analysis. The BRR tool seems to have reflected these findings quite accurately.

A.9 Special Method for Determination of Electron Exchange Equivalents

Calculation of equivalent weights (W_{Eq}) for metals and alloys subjected to polarization measurements is required in order to determine corrosion/oxidation rates. Estimation of W_{Eq} values derived purely from base metal compositional ratios is common practice. However, this may not be the best approach due to selective oxidation of the various alloy components. The concept of selective oxidation is mentioned in ASTM G102 but not elaborated on. In fact, there has been ample data published utilizing depth profiling via XPS (ESCA), SIMS and Auger analysis confirming that selective oxidation does indeed occur. Clearly, differences in oxidation susceptibilities between the alloying elements in a metal mixture are substantial, and the relative fractions of metals comprising cation sites within the oxide lattice are rarely the same as those in the base metal itself. In most cases, the ratio of metals in the substrate and the oxide phase are not even close. Estimation of electron equivalents and equivalent weights utilizing base metal compositions is inaccurate. Depth profiling results of the oxide layers for a couple of relevant alloys are given in Figure A9. There are many more such analyses throughout the literature.\

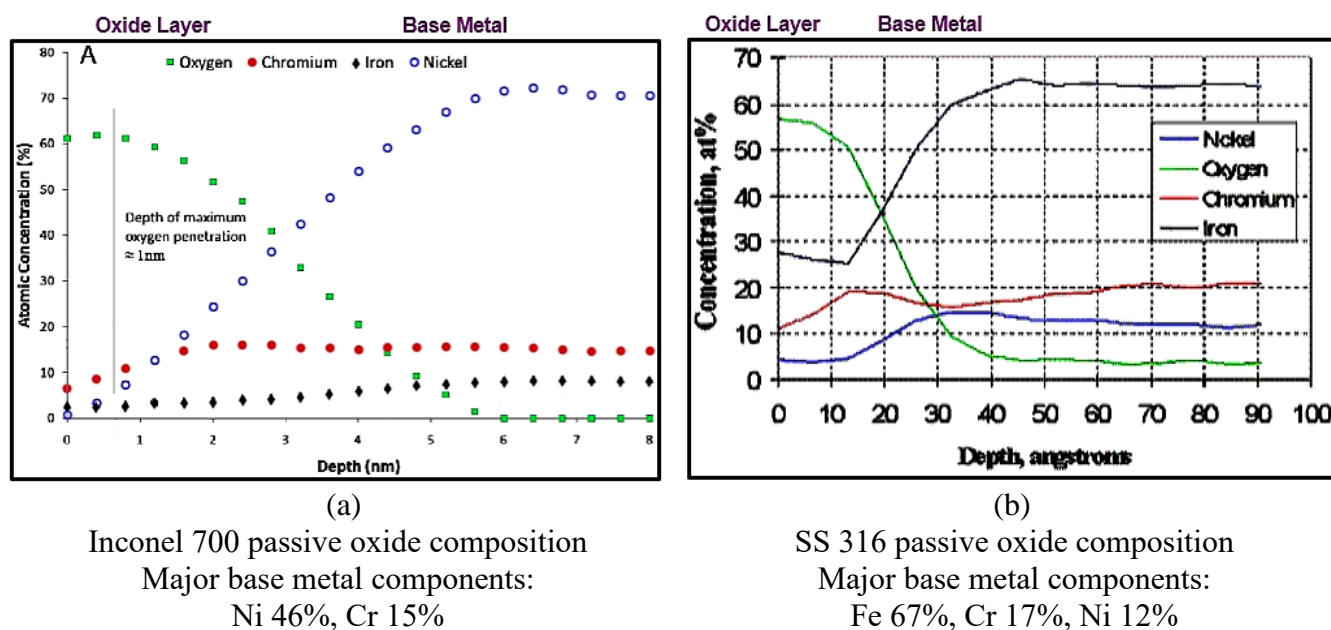
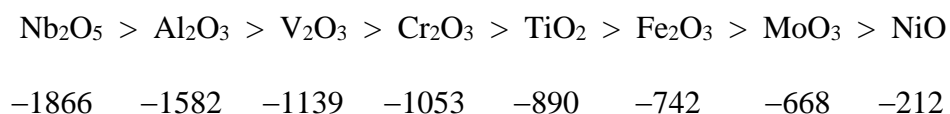


Figure A9: (a) Depth profile of the passive layer on Inconel 700 contrasting the relative metallic concentrations in the base metal and the passive oxide^[11]. (b) Depth profile of the passive layer on 316 stainless steel contrasting the relative metallic concentrations in the base metal and the passive oxide^[12].

The intersection points between oxygen and the primary base metal constituent roughly indicate the center of the metal-to-oxide transition zone. When comparing the percentages of metal components in the oxide (particularly the outer layers of the oxide) and deep within the base metal, it becomes obvious that, at least for passivating metals, estimations involving the transfer of electron equivalents during the oxidation process cannot be precisely represented by assuming that the base metal constituents adequately represent the metallic constituents in the oxide layer. Indeed, in order to be specific, the net number of electrons extracted from the metal during the oxidation process must equal the net number of electrons consumed to form the oxide.

The following approach is proposed as an extension to ASTM G102. Reiterating, the number of electrons transferred from the base metal during corrosive oxidation must equal (exactly) the number of electrons transferred to produce the alloy oxide (in accordance with the conservation laws). Recognition of certain factors associated with the formation and composition of the oxidation product are key to estimating how many exchange electrons are actually generated. It is well known that the various metals in an alloy will oxidize at different rates according to their Gibbs free energy of formation. For example, Cr_2O_3 , with a known formation energy of $\Delta G_f = -1053 \text{ kJ/mol}$ is five times more likely to form than NiO whose formation energy is documented to be $\Delta G_f = -212 \text{ kJ/mol}$. The ΔG_f values clearly reflect this. Thus, we can state that the Relative Ease of Oxide Formation according to the respective free energies of formation can be tabulated and ordered. For example . . .



The more negative the value, the more likely the oxide will form from its elements. A rather extensive database was compiled for this study by tabulating, averaging and evaluating established Handbook values and a multitude of historically documented experimental values obtained throughout the research industry to obtain average representative values for the formation energies, bulk densities, skeletal densities, dielectric constants, and various other material properties for the composite oxides of interest in this study. There would be perhaps too many citations to note here and each input available was taken under consideration only as part of the surmised average, not utilized directly. While bulk compositions and electrochemical properties of the solution-formed oxides are different than the simpler passive layers that form in the air, metal contents are not all that different. Much research, supplementary estimations and educated guesswork were put into this effort in order to better understand, semi-quantify and ascertain the most likely composite oxide compositions and associated net property estimates expected for each of the six metals under evaluation in the subject test solutions. An spreadsheet example of one of the metals processed in this manner is illustrated in Figure A10

Hastelloy C276 **Base Metal** Wrought Composition, As-Received – In Air

| | Raw Wt% | Est Wt% | Mol. Wt. | Atomic % | # Eq. e ⁻ | N _{ae} ⁻ /g |
|---------|-----------|-----------|----------|----------|----------------------|---------------------------------|
| Ni | 58.9% | 59.3% | 58.69 | 63.1% | 0.67 | 1.14E-02 |
| Cr | 16.1% | 16.2% | 52.00 | 19.5% | 2.72 | 5.24E-02 |
| Mo | 15.3% | 15.4% | 95.94 | 10.0% | 0.55 | 5.75E-03 |
| Fe | 5.6% | 5.6% | 55.85 | 6.3% | 0.39 | 6.92E-03 |
| W | 3.4% | 3.4% | 183.84 | 1.2% | 0.10 | 5.18E-04 |
| <hr/> | | | | | | |
| | 99.3% | 100.0% | | 100.0% | 4.42 | 13.0 g/mol |
| | | | | | | Net Equivalent Weight |
| Density | 8.89 g/cc | 8.77 g/cc | | | | |
| | measured | estimated | | | | |



Hastelloy C276 **Composite Oxide** Composition – In Acidic Test Solution

| | Mole % | Atomic % | Less H ₂ O | # Eq. e ⁻ | N _{ae} ⁻ /g |
|------------------------------------|---------|----------|-----------------------|----------------------|---------------------------------|
| Cr ₂ O ₃ | 32% | Cr 21% | 23% | 2.031 | 1.34E-02 |
| CrO ₃ | 8.9% | | | 0.558 | 5.58E-03 |
| CrOOH | 0.48% | | | 0.015 | 1.79E-04 |
| CrOOH ₂ ⁺ | 3.7% | | | 0.118 | 1.37E-03 |
| NiO | 10.5% | Ni 6.8% | 7.2% | 0.221 | 2.96E-03 |
| Ni ₂ O ₃ | 4.1% | | | 0.259 | 1.57E-03 |
| NiOOH | 0.60% | | | 0.019 | 2.06E-04 |
| NiOOH ₂ ⁺ | 5.3% | | | 0.168 | 1.82E-03 |
| MoO ₃ | 6.6% | Mo 2.5% | 2.6% | 0.416 | 2.89E-03 |
| MoO ₂ | 0.53% | | | 0.022 | 1.73E-04 |
| MoO ₂ (OH) ₂ | 0.20% | | | 0.012 | 7.70E-05 |
| MoO(OH) ₂ ⁺ | 1.6% | | | 0.102 | 6.24E-04 |
| Fe ₂ O ₃ | 4.6% | Fe 3.5% | 3.7% | 0.289 | 1.81E-03 |
| FeO | 0.08% | | | 0.002 | 2.28E-05 |
| Fe ₃ O ₄ | 0.94% | | | 0.074 | 3.20E-04 |
| FeOOH | 0.08% | | | 0.002 | 2.68E-05 |
| FeOOH ₂ ⁺ | 0.60% | | | 0.019 | 2.11E-04 |
| WO ₂ | 0.61% | W 0.47% | 0.50% | 0.026 | 1.18E-04 |
| WO ₃ | 0.87% | | | 0.055 | 2.37E-04 |
| WO ₂ (OH) ₂ | 0.03% | | | 0.002 | 6.59E-06 |
| WO(OH) ₂ ⁺ | 0.21% | | | 0.013 | 5.25E-05 |
| | | | | | 4.42 Total Metal Equivalents |
| H ₂ O | 17% | O 65% | 63% | 4.42 | Total Oxygen Equivalents |
| <hr/> | | | | | |
| | 100.00% | 100.00% | 100.00% | | 29.8 g/mol |
| | | | | | Net Equivalent Weight |
| | | | | | 4.00 g/cc |
| | | | | | estimated density |

Figure A10: Average model composition and equivalents for the Hastelloy-oxide system in acidic solution.

Note in Figure A10 that the total number of electrons transferred from the base metal to the proposed metal oxide mixture are identical, as they should be. Identifying this value effectively permits estimation of the corresponding equivalent weights involved for both the base metal and its unique composite oxide. Also note that the metallic atomic concentrations in the oxide mixture are compliant with expectations via XPS, SIMS, Auger, etc... If the calculations were conducted utilizing strictly base metal compositions and the typical number of valence electrons one normally assumes, estimated equivalent weights for this metal would be on the order 23-25g/mol. However, the proposed approach provides equivalent weights which are unique to both the base metal and the composite oxide and which are connected by the net number of electron equivalents transferred between the two phases. This opens the door to more elaborate endeavors regarding oxide growth phenomena and passivation mechanics that are specific and exclusive to a given alloy under study. At present, estimation of electron and weight equivalents via oxide formation is complex, tedious and time-consuming. Even with the aid of Pourbaix and Ellingham diagrams, certain assumptions must be made and errors are likely without due diligence, but it is the correct way to determine the number of electrons transferred during the oxidation process.

Finally, note that most of the oxides of interest here are amphoteric in nature with pendant hydroxyl groups protruding along the surfaces prior to immersion into the acidic solution. Immediately upon immersion, these hydroxyl groups become protonated (positively charged) during formation of the electrical double layer (EDL). Then, as the EDL evolves, positive sites along the surfaces of the porous and barrier layers begin to attract anions that are present in the solution such as chlorides, sulfates, phosphates, carboxylates, urates, hydrolases, etc... These associations may comprise the outer Helmholtz plane or slip layer as steric hindrance increases diffusivity factors while disrupting access of reactants and products into the oxide/hydroxide macrostructures and ultimately to the base metal. This activity plays a role in the actual levels of specific secondary and tertiary oxides and oxyhydroxides that initially develop from each metallic component as it interacts with the solution.

A.10 Model Development for Pitting Rates and Penetration Depths Over Time

The variety of shapes, depths and surface openings characterizing pits are essentially infinite, and attempting to account for the density of pits across a given surface at any given time can make the measurement of pitting events even more complex. There is an abundance of resources available that cover pitting phenomena and several standards providing instruction pertaining to pit measurement and characterization (ASTM G46 provides an excellent description of pitting morphologies). Those concepts will not be explored here at this time. It is not the intent here to delve into all the intricacies of pitting science, but rather to explore a simplistic approach to envision how pitting rates and penetration/recession depths that might vary under certain circumstances, should pitting corrosion occur.

While general recession/oxidation rates sometimes appeared to be higher in the pretreat environment, pitting susceptibilities seemed to be more prominent in the brine solution. In all likelihood, this is a result of the higher chloride content in the concentrated brine media. It should be emphasized that under normal operating conditions, it is believed that pitting is highly improbable in either solution with any of these metal candidates, including Cronidur. The observed pitting on Cronidur samples during polarization testing occurred under aggressive and accelerated test conditions where damaging voltages were applied. While small voltages may simulate accelerated life conditions to a degree, higher voltages

tend to promote side reactions, degradation effects and anomalies not associated with actual corrosion events and would not occur normally occur under average field conditions.

Caution must be applied when interpreting pitting and repassivation information from the upper anodic regions of cyclic polarization curves. As presented in previous reports, the maximum achievable pitting recession rates can be extrapolated from the lowest possible slopes in the region following the breakdown point E_{Brk} prior the vertex (assuming the vertex is tailored into the test run appropriately). Additionally, relative time periods from E_{Brk} to the maximum pitting slope can be extrapolated from the scan data and are unique for each metal. In short, these extrapolated values become critical factors in simulating how pitting rates and recession depths might change or evolve over time. If pitting happens to initiate and sustained growth follows, what would the growth profile look like?

Early on, it was envisioned that pitting recession rates rise rapidly after initiation, reach a peak rate (that is, a maximum pitting rate) and then decline slowly to zero as oxide product increasingly blocks the pit entrances, while penetration/recession depths increase pseudo-parabolically over time and then level off at some maximum plateau. Hard field data has confirmed that this perception is indeed what happens. There are a number of published works over the last 40-50 years in which sample weight losses and penetration depths were physically measured at regular time intervals over several years. In particular, field data presented in a couple of interesting studies examining low alloy steels, stainless steels and an Inconel alloy were utilized for the work efforts in the current project. These results have revealed some very compelling curve forms or profiles describing the evolution of recession depths and rates over longer time periods which are believed to be characteristic of essentially all metals.

It has been established during these efforts that changes in penetration depths p over time t closely follow a modified exponential or Weibull-type function which starts out at zero and increases to a plateau as the maximum penetration depth is achieved and pitting ceases . . .

$$p_{pit} = p_{\infty} - a_1 \exp(-b_1 t^{c_1})$$

where p_{∞} becomes the theoretical maximum pit depth attainable and a_1 , b_1 and c_1 are constants that control the shape of the profile. The time derivative of this function gives the penetration rate over time k_{pit} which ascends to a maximum rate under activation control and then decreases to zero under diffusion control. It has been found to closely correspond to a Hoerl power function . . .

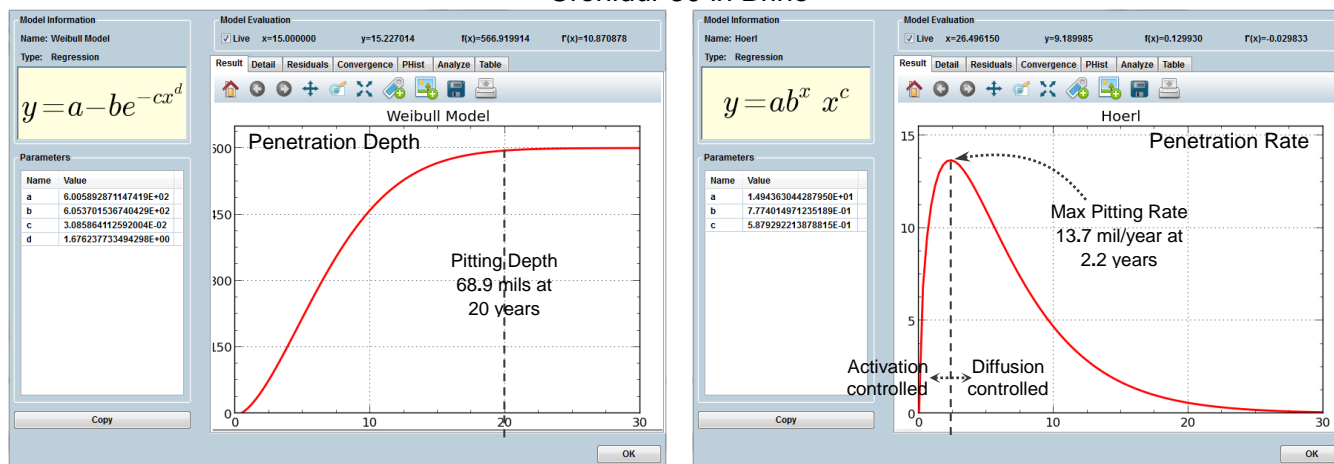
$$\frac{dp}{dt} = k_{pit} \cong a_2 b_2' t^{c_2}$$

where a_2 , b_2 and c_2 are profile shaping constants.

Model profiles describing penetration depths and rates were established for each of the six metals in both test solutions utilizing the maximum pitting rate estimates and E_{Brk} times obtained from the polarization scans. In addition, average pitting shapes were based on conic-type volumes (for simplicity) which penetrate about 5 times deeper than general recession. These results are considered only to represent possible depths and rates in an unlikely worst-case scenario in which the repassivation protection

mechanism for each metal is overcome, inhibited or otherwise ignored. Graphical results for two of the subject metals are given in Figure A11 as examples of the technique applied to all candidates.

Cronidur 30 in Brine



Titanium LI in Pretreat

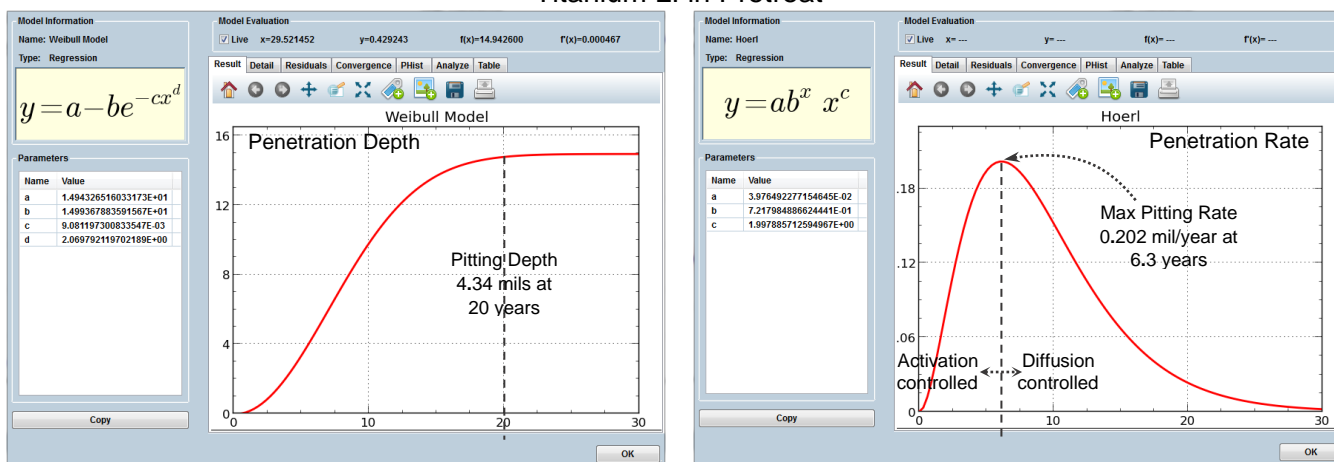


Figure A11: Example of modelled pitting penetration depths and rates for Cronidur 30 and Titanium LI.

Maximum penetration rates and the corresponding time periods estimated for six previously tested metals in Pretreat media were (1) Titanium CP: 0.181 mpy at 5.4 years, (2) Titanium LI: 0.202 mpy at 6.3 years, (3) Titanium 6-4: 0.268 mpy at 7.2 yrs, (4) Inconel 625: 2.47 mpy at 3.2 yrs, (5) Hastelloy C276: 2.08 mpy at 3.2 yrs, (6) Cronidur 30: 6.0 mpy at 2.5 yrs, and in Brine media, (1) Titanium CP: 0.326 mpy at 6.0 yrs, (2) Titanium LI: 0.296 mpy at 6.7 yrs, (3) Titanium 6-4: 0.332 mpy at 6.8 yrs, (4) Inconel 625: 3.19 mpy at 3.2 yrs, (5) Hastelloy C276: 3.67 mpy at 3.1 yrs, and (6) Cronidur 30: 13.7 mpy at 2.2 yrs (where mpy = mil/year).

It should be noted that the current corresponding directly with E_{Brk} on a typical Cyclic polarization plot can often be identified as the 'metastable pitting current' where pitting (metal recession) and repassivation (oxide regeneration) may be occurring simultaneously at the same opposing rates. Unfortunately, a correct interpretation of pitting rates cannot be obtained from some coincidental point

where the scan lines happen to intersect on a cyclic polarization plot. More importantly, there is no ‘average’, ‘stable’ or ‘constant’ pitting rate and there is no single value that represents the pitting rate because . . . pitting rates are always changing! A pitting rate life cycle goes from zero up a long ramp over time, through a momentary maximum, and then back down over even longer ramp to an asymptotic zero. In a cyclic run, pitting rates vary from a low metastable condition around E_{Brk} to a maximum rate somewhere from 0.05-0.5V beyond E_{Brk} . In real world situations, after pits have initiated and the conditions are favorable for continued (sustained) pitting, rates increase exponentially, reach a peak (a maximum pitting rate $I_{Pit,Max}$) and then gradually diminish to zero as corrosion products fill the pit volume and diffusional blockage eventually inhibits further reactions into the active pit area.

A.11 Increasing Solution pH Over Time

What happens when a passivating metal is immersed in an acidic solution and why does the pH increase over time? Prior to immersion, these metals develop very thin, highly protective oxide layers on their surfaces within seconds after fresh machining, surfacing or etching as peripheral metal atoms rapidly interact with atmospheric oxygen. Typical layer thicknesses are 2-5 nanometers. Transition zones comprise the bondlines between metal substrate and oxide layer. For a constant environment, the process is self-limiting as O₂ molecules diffuse through the oxide structure where they oxidize Cr atoms leading to inward recession of the base metal and inward/outward growth of the oxide phase. A simple illustrated of passivation in air is given in Figure A12.

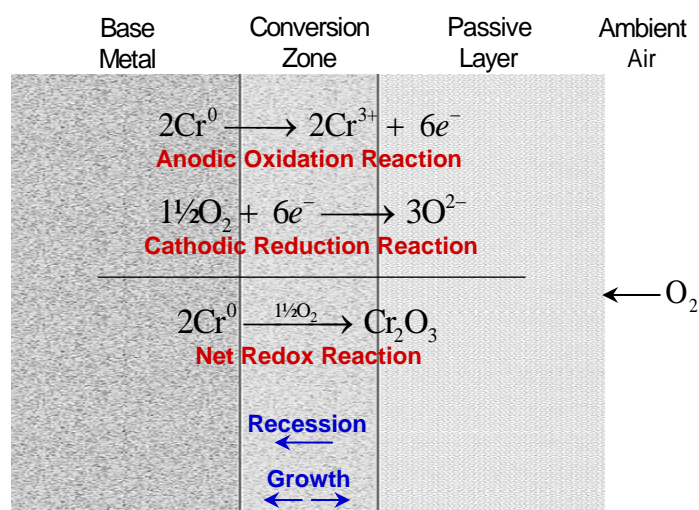


Figure A12: Simplified depiction of passive layer formation on a chromium alloy in air.

Upon immersion in electrolytic media, an electrical double layer (EDL) quickly forms as the oxide surface adapts to the new environment. In addition, oxygen-rich, acidic media begins to slowly dissolve the oxide layer while Cr⁶⁺ ions are ejected into the solution and H⁺ ions are reduced to H₂, which bubbles away. This more advanced situation is shown in Figure A13.

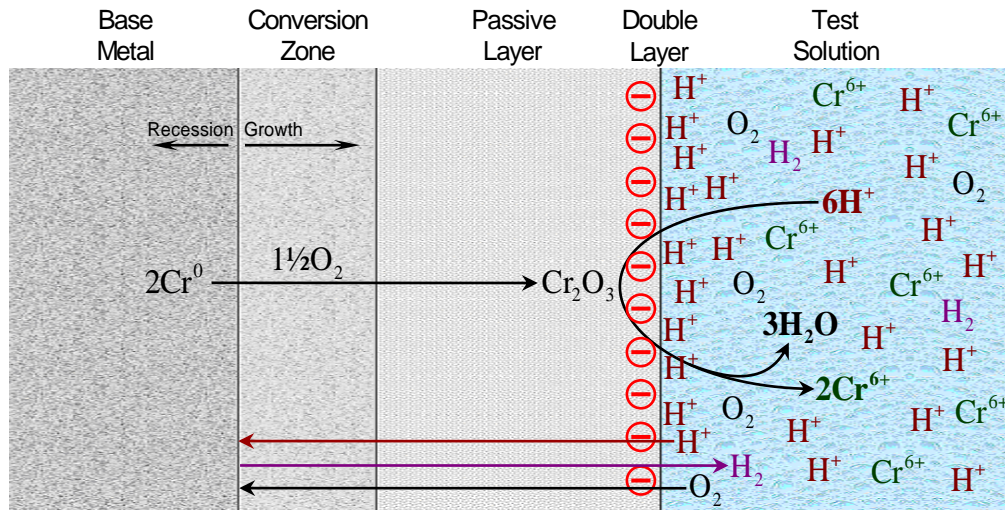
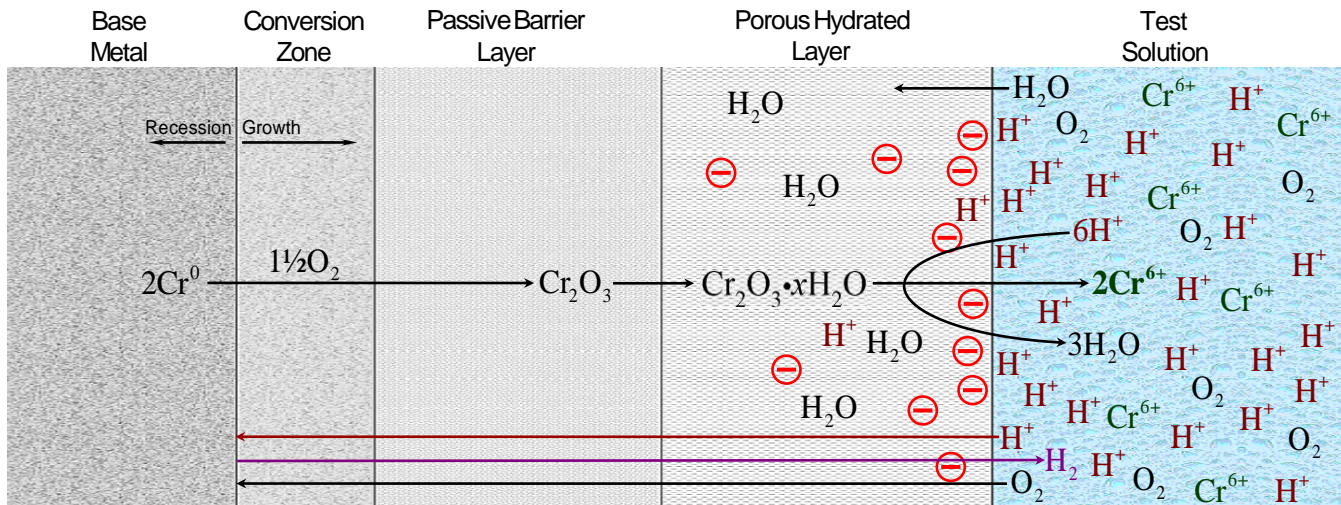


Figure A13: Illustration of a passivated chromium alloy a few seconds after immersion in an acid electrolyte

In response, the oxide regenerates itself very quickly and it also develops a thick, porous, hydrated layer on the outside facing the solution which tends to generalize the EDL across space. The system remains neutral throughout. This is depicted in Figure A14.



A14: Illustration of a chromium alloy several minutes after immersion

Relevant reactions include (A) anodic oxidation of the base metal (resulting in metal recession and oxide growth), (B) cathodic reduction of hydrogen ions H^+ to H_2 in the local solution, and (C) dissolution of the metal oxide. All three reactions eventually reach equilibrium along a plateau at Steady State where $k_A \Gamma k_B \Gamma k_C$. During the reduction and dissolution reactions, H^+ ions are consumed to form molecular H_2 and water as shown in reactions B and C. The H_2 bubbles away as a gas while H^+ ions are depleted. Thus,

the concentration of H^+ ions in the solution decreases as the passive layer dissolves and replenishes. The rates for hydrogen reduction and oxide dissolution are both kinetically-favored. However, these reactions are attenuated due to the diffusion-controlled rate of oxidation in the metal-oxide conversion zone as reactants and products must travel through the nonporous oxide barrier to reach the metal surface. It should be noted that in a large, flowing ECLSS reservoir, slight pH changes would likely be trivial. In contrast, the small test bins used in our experiment were configured to contain minimal amounts of test solution and the exposure was conducted under entirely stagnant conditions at room temperature. In this case, the pH drop is expected to be more noticeable. Due to its high viscosity, reactions within the concentrated stabilizer will tend to be diffusion-limited while those in the diluted version will tend to be kinetic-controlled.

Dispersed charges in the growing conductive porous layer decrease the capacitance of the system while contributions associated with the insulative barrier layer (primary barrier) become negligible. The differential capacitance can be defined as a function of the change in charge build-up at the EDL interface, $dq = Idt$, to the change in voltage dE and is inversely related to the thickness L of the coating (roughly) which is comprised mostly of the porous layer . . .

$$C_d = \frac{Idt}{dE} \propto \frac{1}{L}$$

Initial slopes in the original Open Circuit Potential plot may provide clues regarding the relative growth rates for these two layers. As an example, consider the plot given in Figure A15. At the onset, the relative rate of the porous layer (as reflected by dE/dt) increases substantially at the expense of the primary barrier layer (indicated by dI/dt).

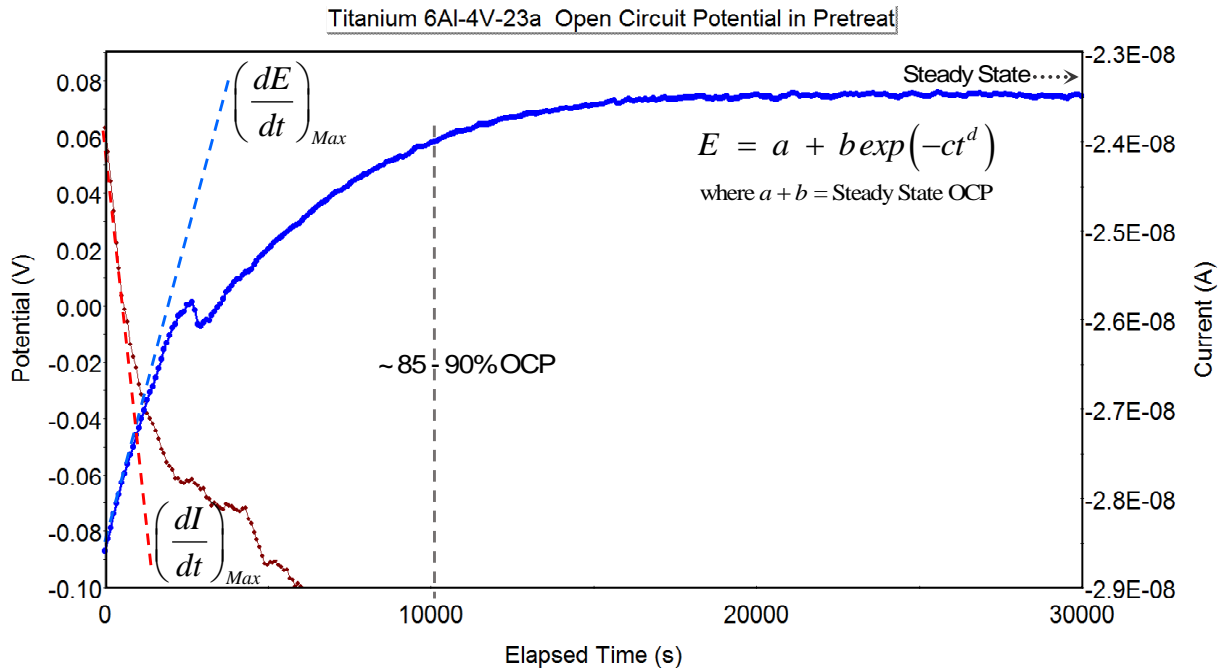


Figure A15: Example Open Circuit Potential curve obtained from previous studies.

A.12 Special Method for Estimating Corrosion Susceptibilities

The concepts of susceptibility defined for this study are rudimentary and should be considered as extensions to the topics covered in ASTM G102. They are purely creations of the author which seemed to work well for the current study. No guarantee is given regarding their validity, correctness or accuracy in any other application. Since these are evolving concepts at this point, it is perhaps best to consider all susceptibility definitions as ‘relative’ to the group of metals under evaluation in this study.

Before the porous layer precipitates and coats the solution-oxide surface, an electrical double layer (EDL) develops which contributes the majority of the capacitance exhibited by the combined surface layers. As the porous layer grows and widens, contributions from the EDL capacitance decrease, and when positive (anodic) voltage is applied, the EDL charges up as the capacitance increases. Now the barrier oxide layer itself also produces a small capacitance due to the separation of charges at the barrier-porous interface and charges along the metal surface (or within the conversion zone) with the barrier oxide acting as the dielectric. Generally, the oxides studied here are all ceramic dielectric insulators, but most of them exhibit point defects characteristic of *n*-type semiconductivity where cation interstitials (Cr_i^{3+} , Ti_i^{4+} and Fe_i^{3+}) and oxygen vacancies ($\text{V}_o^{\bullet\bullet}$) become the primary charge carriers leading to metal ion ejection into the solution as hydrolytic dissolution takes place. When the applied voltage exceeds a threshold voltage, which is generally prior to the breakdown potential E_{Brk} , the behavior transitions over to *p*-type conductivity. Beyond E_{Brk} , conduction may occur by tunneling or avalanche effects (nickel oxide NiO itself is a *p*-type conductor throughout and will be addressed later).

During open circuit exposures and external polarization fields, the dielectric barrier layer evolves in thickness along with corresponding changes in barrier layer capacitance $C = q/E_{App} = \epsilon_0 \epsilon_r A/t$, surface charge density, $\sigma = q/A = \epsilon_0 \epsilon_r E_{App}/t$ and electric field strength, $\mathcal{E}_{Pol} = \sigma/\epsilon$ (in accordance with Gauss’ law). Here, q is the charge transferred from the base metal to the oxide to the solution, E_{App} is the applied test voltage (the potential difference across the oxide), A is the sample test area (fixed at 1 cm^2 throughout), t is the barrier layer thickness, ϵ_0 is the vacuum permittivity constant and ϵ_r is the relative permittivity of the oxide (that is, ϵ_r is the dielectric constant of the oxide while $\epsilon_0 \epsilon_r = \epsilon$ is the absolute permittivity).

Now recognize that $\mathcal{E}_{Pol} = \sigma/\epsilon = CE_{App}/A\epsilon$, or $E_{Pol}\epsilon = CE_{App}t/A$, from which a representative breakdown indicator specific to that oxide layer can be envisioned. The product $E_{Brk} \cdot \epsilon_r$ carries a special significance indicating the tendency of the oxide to resist the breakdown forces and protect itself by virtue of its inherent properties. The value of the breakdown potential E_{Brk} provides information regarding the propensity of the oxide to fail with subsequent pitting into the base metal, while ϵ is a relative indicator of the oxide’s dielectric capability. If both of these factors are high, there is a very low probability that the oxide will succumb to the breakdown forces. One factor can compensate for the other. If one is high and the other low, the oxide can still be protected. But if both factors are low, the susceptibility is high and breakdown is imminent. To be more proper, consider the height of E_{Brk} above another potential of interest, say the primary passivation potential, that is . . . $(E_{Brk} - E_{Pas})\epsilon_r$. This is reasonable since the greater the voltage difference between E_{Brk} and E_{Pas} , the lower the propensity that breakdown will occur. Conversely, an argument can be made regarding the repassivation potential, since the higher and closer it is to E_{Brk} , or rather the smaller the difference between E_{Brk} and E_{Rep} , the higher the chance that repassivation will protect the recovering metal surface, that is . . . $(E_{Brk} - E_{Rep})/\epsilon_r$. These insights are consistent with real world perceptions and are in accordance with recognized interpretations of cyclic polarization curves.

In a more comprehensive and decorous approach it is proposed that the relative susceptibilities for the initiation (nucleation) and sustainment (unabated growth) of pitting can be represented respectively by the following arguments . . .

$$(E_{Brk} - E_{Pas})\epsilon_r \quad \text{and} \quad (E_{Brk} - E_{ReP})\epsilon_r^{-1}$$

Formal definitions can then be proposed for the relative susceptibilities to Pitting Initiation S_{PiI} and Pitting Sustainment S_{PiS} in exponential form, respectively . . .

$$S_{PiI} = 1 - \exp\left[\left((E_{Brk} - E_{Pas})\epsilon_r\right)^{-1}\right] \quad \text{and} \quad S_{PiS} = 1 - \exp\left[\left((E_{Brk} - E_{ReP})\epsilon_r^{-1}\right)^1\right]$$

Thus, when S_{PiI} is low, E_{Brk} and E_{Pas} are far apart, and when S_{PiS} is low, E_{Brk} and E_{ReP} are close together. Likewise, the higher the relative permittivity constant for a given oxide ϵ_r , the lower the susceptibility. Figure A16 shows example susceptibility plots for three of the subject test metals which indicates the stark differences between these metals in terms of pitting initiation. Delta potentials for Cronidur in pretreat solution ranged from about 0.5 to 1V while those of Inconel ranged from about 0.7 to 1.1V and for Titanium CP, 1.4 – 1.7V. These potential ranges are numerically descriptive of the estimated susceptibilities for each of the metals and are emphasized in Figure A16. As one might expect, the Titanium metals possess strong protection mechanisms across the board, especially in the measured test range, while Cronidur appears to exhibit an elevated level of susceptibility towards pitting, and the Inconel samples indicate susceptibilities that are in between but closer to Cronidur. These results were also reflected in the actual data summary and results for those studies.

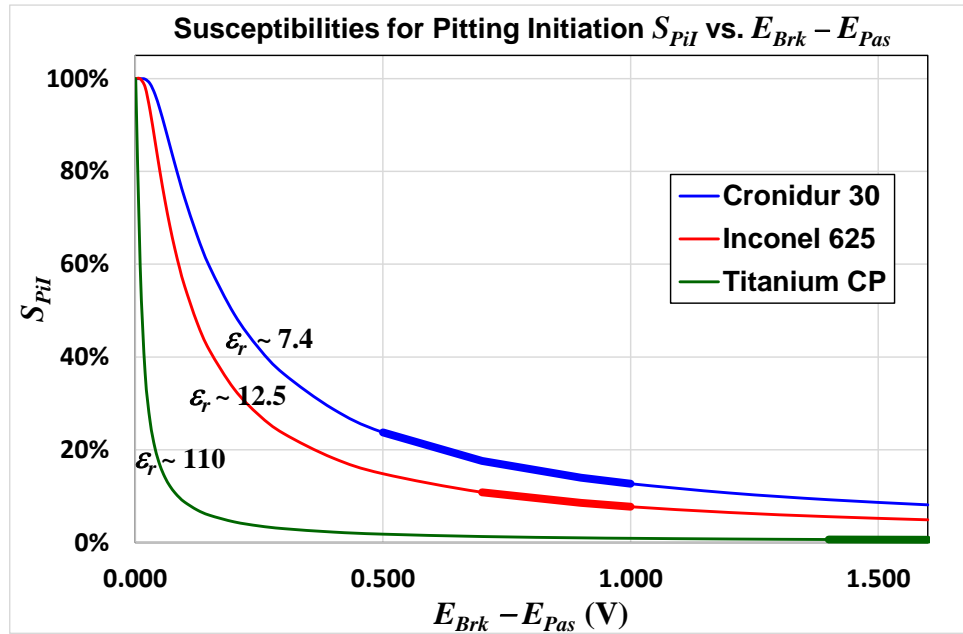


Figure A16: Pitting initiation plots for three of the test metals in pretreat showing the respective active areas.

For further consideration, consider two contrasting cases taken from typical Titanium and Cronidur cyclic runs obtained during previous studies. These are depicted in Figures A17 and A18 which illustrate a few key factors associated with susceptibility, hysteresis and semi conductivity.

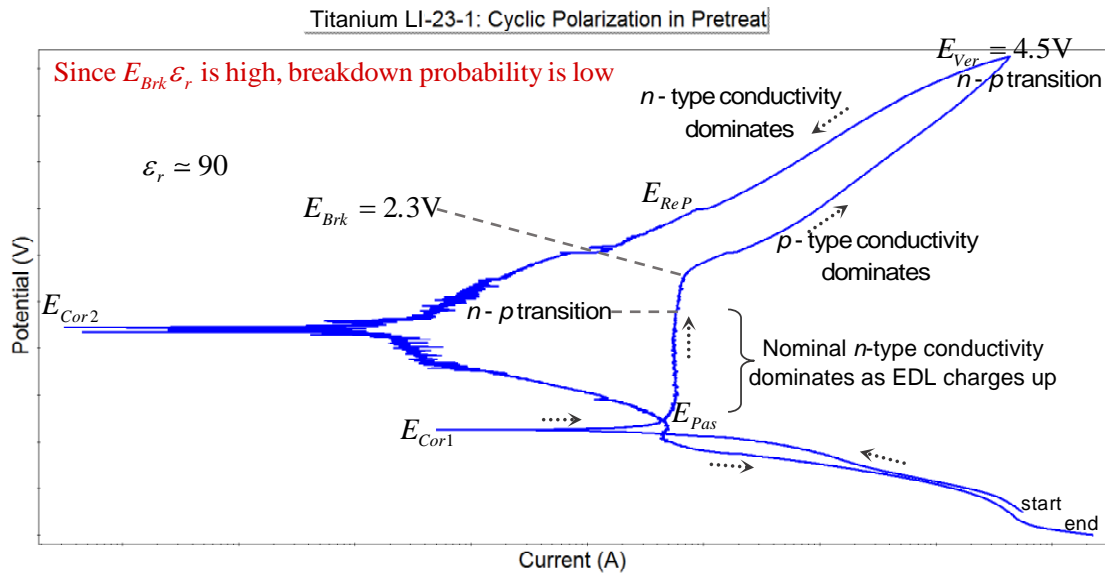


Figure A17: Cyclic plot for Titanium LI showing possible relationships between conductivity and susceptibility.

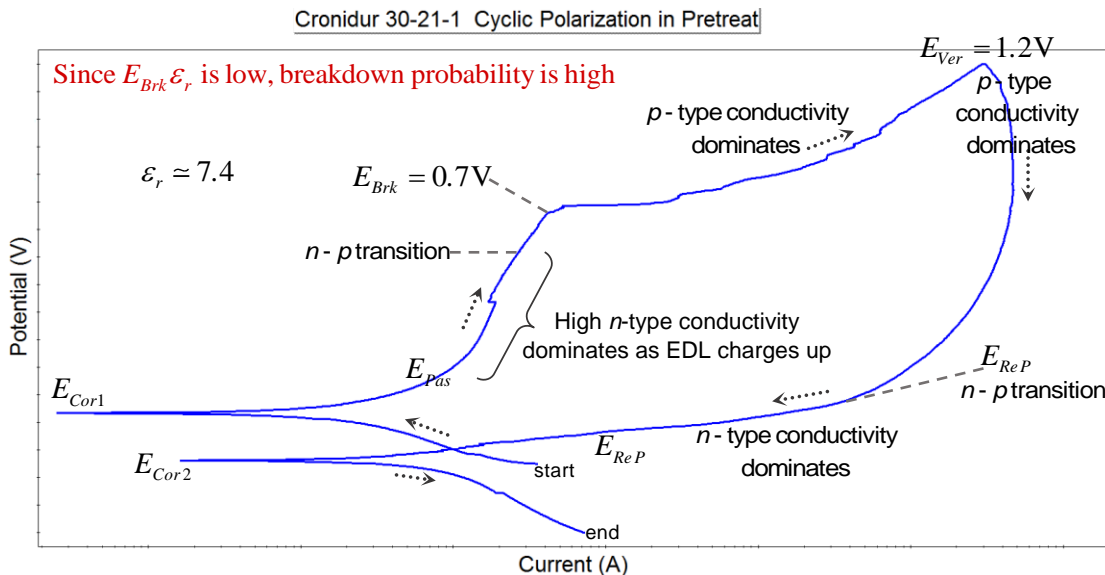


Figure A18: Cyclic plot for Cronidur 30 showing possible relationships between conductivity and susceptibility.

After the potential changes polarity (from cathodic to anodic) at E_{Cor1} , the passivation rate accelerates. When most of the growth is complete at E_{Pas} , the curve passes ‘onto the passive plateau where n -type conductivity accommodates the charge accumulation along the EDL. At the threshold voltage, conductivity switches from n -type to p -type as metal cations are ejected into the solution and cation vacancies become the major charge carriers. After E_{Ver} , oxide regeneration is accompanied by restoration of n -type conduction. The greater the regions of n -type behavior during anodic charging, the lower the corresponding S_{PiI} , and the smaller the n -type range during anodic discharging, the lower the S_{PiS} .

The methods outlined earlier for estimating S_{PiI} and S_{PiS} can be extended to provide similar representations possibly representing general corrosion susceptibility pertaining to E_{Cor} by making use of certain thermodynamic equivalences. Again, standard values for the Gibbs free energy change of formation ΔG_f^0 have been utilized for each component comprising the passive oxide layers on the metals evaluated. From these results, complex averages were developed for each composite oxide, all of which are part of the special materials property database developed for this study. With this approach, the relative susceptibility for general corrosion during OCP measurements and Linear polarization analysis can be roughly estimated . . .

$$S_{Cor} = 1 - \exp \left[\left((E_{Cor} - E_f^0) \varepsilon_r \right)^{-1} \right]$$

where E_f^0 is the corresponding potential change associated with the free energy change of formation ΔG_f^0 which follows from the Nernst equation, that is . . . $G_f^0 = -nFE_f^0$.

Values for S_{Cor} were provided earlier in the report when the data for OCP and Linear/Tafel analysis was presented. During analysis of the galvanic couple configurations, differences between the couple potential E_{OCG} and original open circuit potential E_{OCI} were computed utilizing the factor $(E_{OCG} - E_{OCI})\varepsilon_r$. Overall, while these susceptibility concepts may seem simplistic, they appear to have work quite well for these studies, providing good representations of the relative corrosive tendencies for each test metal as they combine inherent material properties with actual test data. For informational purposes, average values developed for the dielectric constants and the Gibbs free energy potentials associated with each of the composite oxides examined in this study are given in Table A1.

Table A1: Average representative values utilized for ε_r and ΔE_f^0 during estimation of relative susceptibilities.

| | Inconel 625 | Hastelloy C276 | Titanium CP | Titanium 64 | Titanium LI | Cronidur 30 |
|-----------------|-------------|----------------|-------------|-------------|-------------|-------------|
| ε_r | 12.46 | 11.43 | 110.0 | 90.22 | 90.40 | 7.38 |
| ΔE_f^0 | -2.68 V | -2.35 V | -2.91 V | -3.17 V | -3.18 V | -2.89 V |

A.13 Passive Films as Pseudo-Capacitors and Semiconductors

Several models have been developed to describe the oxide growth process on passive metals including the High Field Model, the Place Exchange Model and the Point Defect Model. Of these, the Point Defect Model (PDM) developed by D.D Macdonald appears to account for all the experimental observations regarding the structure and behavior of passive films. The methodologies and calculations involved in the PDM are intensive, and it is beyond the scope of this paper to present all the associated concepts here. However, for qualitative purposes, it will be interesting to explore some of the possible reactions responsible for the conduction of ions across the oxide layer as well as growth and dissolution of the layer itself. A representative scenario is illustrated in Figure A19 utilizing chromium as an example and making use of Kröger-Vink notation.

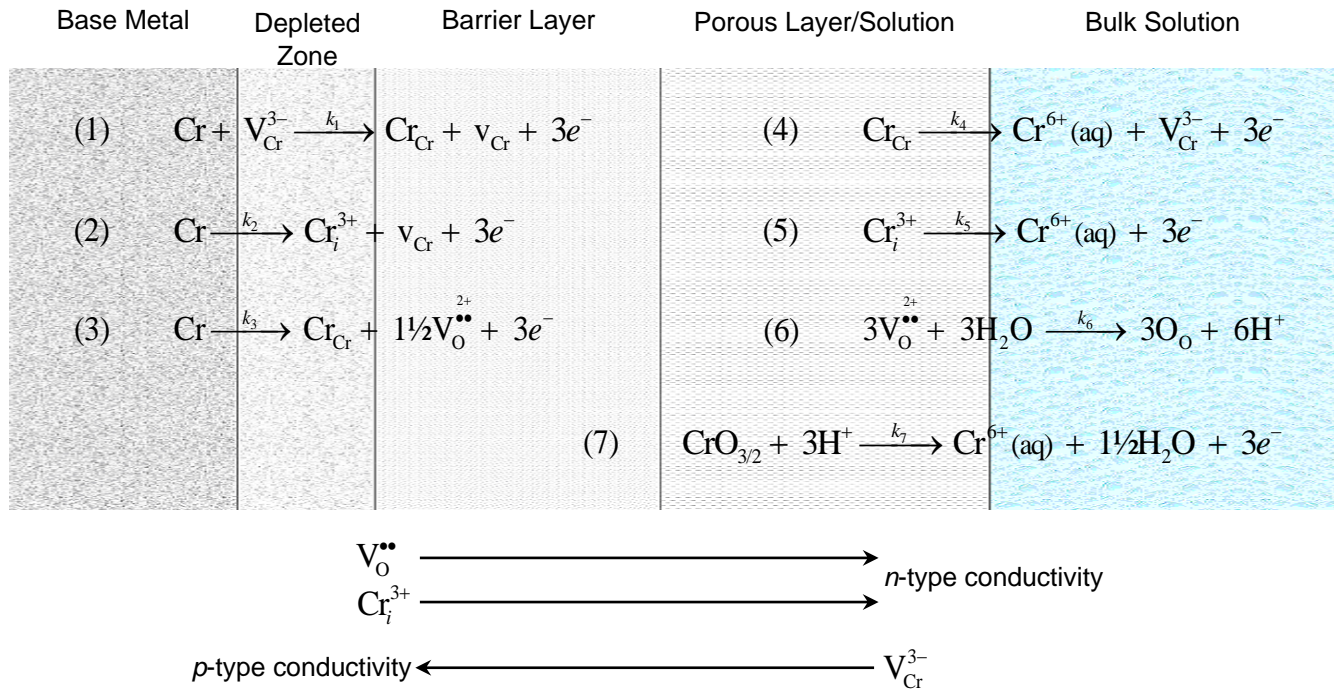


Figure A19: Possible reactions for a chromium substrate leading to conduction, oxide production and dissolution. Cr = metal atom in base metal, $\text{V}_{\text{Cr}}^{3-}$ = cation vacancy in oxide lattice, Cr_{Cr} = metal cation at cation site in oxide lattice, v_{Cr} = vacancy in base metal, Cr_i^{3+} = interstitial cation in oxide lattice, V_{O}^{2+} = oxygen vacancy in oxide lattice, $\text{Cr}^{6+}(\text{aq})$ = fully oxidized metal cation in solution, O_{O} = oxygen anion in oxygen lattice, and $\text{CrO}_{3/2} = \frac{1}{2} \text{Cr}_2\text{O}_3 = \text{Cr}_{\text{Cr}} + 1\frac{1}{2} \text{V}_{\text{O}}^{2+}$.

The theory is based on the activity of Schottky point defects associated with *n*-type conductivity as described by reactions (2) and (5), and reactions (3) and (6), and Frenkel point defects associated with *p*-type conductivity as described by reactions (1) and (4). Furthermore, transmission of ions through the barrier layer are inferred to occur exclusively by the motions or fluxes of vacancies and interstitials which are created at one of the interfaces (either the metal-oxide interface or the oxide solution interface) and then annihilated or depleted at the opposite interface. The nonconservative reactions (3) and (5) lead to growth and dissolution of oxide respectively and are responsible for movement of the oxide boundaries. At steady state, certain reactions are in equilibrium, that is, $k_1 = k_4$, $k_2 = k_5$ and $k_3 = k_6 = k_7$.

The barrier layers on Cronidur, Titanium and its alloys are known to exhibit *n*-type conductivity at lower potentials and then transition to *p*-type at some point just prior to E_{Brk} . This implies that conduction across these oxides is accomplished by the movement of oxygen vacancies $V_O^{\bullet\bullet}$ (or holes) and cation interstitials Cr_i^{3+} , both of which become electron donors that are annihilated (or depleted) at the solution interface. However, in the nickel-based alloys Inconel 625 and Hastelloy C276, the nickel oxide (NiO) component behaves as a *p*-type conductor throughout and is characterized by the movement of cation vacancies V_{Ni}^{2-} which become electron acceptors that would be depleted at the metal interface. If phase separation happens to occur between the Cr_2O_3 and NiO fractions, a *p-n* heterojunction is established along their common interface. This phenomena is explored further in the next section.

A.14 Anomalies on Nickel Alloys under Extreme Test Conditions

During previous testing in ECLSS brine solutions, some of the Inconel and Hastelloy samples exhibited unusual effects during abnormal cyclic polarization in pretreat media when cyclic starting voltages were significantly cathodic (negative). Some of the test samples were pre-conditioned at strong negative potentials during the beginning of the cyclic scan in order to test the extremes and to explore the possible ramifications. Figure A20 gives an image of one of the Hastelloy samples evaluated during these prior tests which was conditioned at $-0.75V$ for five minutes at the beginning of the cyclic polarization scan. Observational notations are also given.

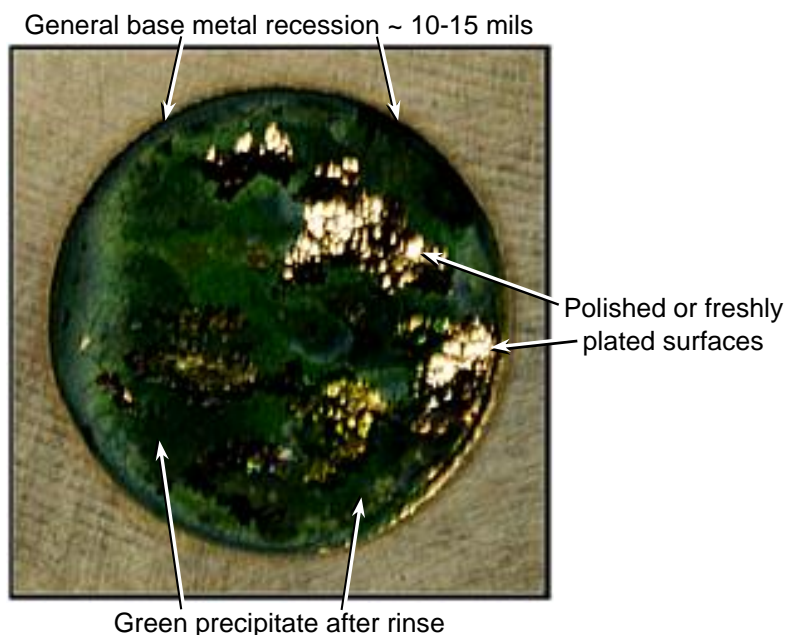


Figure A20: Hastelloy sample surface after cyclic polarization scan in pretreat with $-0.75V$ cathodic conditioning.

It should be realized that these types of results were obtained only under very extreme test conditions during exposure to brine solution concentrate. This could be related to the lower level of associated ion pairs in the fresh acid solution along with a condition of high activation-controlled access to the metal surface as compared to the viscous brine media in which chemical reactivity may be limited

by concentration diffusional effects. Testing showed that cathodic stripping can begin at potentials as high as -0.2V . Likely causes for the green precipitate will be addressed first.

It is suggested that at the end of the polarization scan, the concentration of dissolved nickel ions near the sample surface is very high. When the sample was quickly removed from the solution and gently rinsed in pH 7 water, regions of green precipitate remained. It was shown that continued rinsing and/or more aggressive rinsing would wash away these precipitated remnants. It is believed that the green precipitates are comprised of nickel hydroxide $\text{Ni}(\text{OH})_2$, nickel oxyhydroxide NiOOH and complexed nickel hydroxide/hydrates derived from the semi-organic brine test solution. While $\text{Ni}(\text{OH})_2$ crystals are generally light-to-pale green in form, the organic complexes in this precipitate are believed to be responsible for the rich green appearance. Factors leading to recession of the base metal, electrolytic polishing and/or metallization ('back-plating') on the interim surface require a more intensive analysis.

In short, it is surmised that following cathodic stripping of the air-formed passive layer, anodic regeneration of the new passive layer facilitated migration, concentration and/or separation of the nickel oxide (NiO) phase toward the periphery of the layer placing it in direct contact with the solution. The NiO outer layer acted as a barrier to inward oxygen flow and began to trap electrons within the Cr_2O_3 core which underwent reduction (cathodic weakening of the crystal structure) until the outer NiO barrier layer failed at or after E_{Brk} . This condition exposed the unprotected base metal to the acid solution at high anodic voltage inducing rapid etching into the metal. Metallization effects could have been facilitated by the high concentration of Ni^{2+} ions local to the surface following the voltage reversal at E_{Ver} , and/or electrolytic polishing effects could have taken place during the repassivation process following E_{Rep} .

There are standard industry practices for stripping the passive layers from metal surfaces which can be performed under cathodic voltages or in acid solutions or both. Mixtures of phosphoric and chromic acid have been used for this purpose (same acids in the pretreat solution). Thus, it is reasonable to understand how cathodic conditioning prior to or at the beginning of a polarization scan can easily result in stripping of the passive layer. If left under cathodic control in an acid solution for very long, etching of the base metal will begin. In weak chromic/phosphoric etching solutions at ~ -0.75 to -1V , the oxide layer may be completely stripped away in a matter of a seconds or minutes. After the passive layer anodically re-forms up to E_{Pas} and along the passive plateau, electrolytic polishing of the oxide surface may take place. Again, such concepts are common practice in the metal finishing industry.

Unfortunately, chemical analysis of the samples and Electrochemical Impedance Spectroscopy (EIS) were not conducted during these studies due to scheduling and cost constraints. Surface compositional analysis may have provided information regarding the nature and possible factors leading to formation of the observed products, while Mott-Schottky capacitance-potential plots obtained via EIS would have facilitated estimations of the respective charge carrier concentrations during the voltage sweep. Thus, the mechanisms proposed in the descriptions and explanations given in the following paragraphs are primarily hypothetical at this time.

A number of researchers have confirmed the formation of p - n type barrier bilayers under anodic conditions on nickel-rich alloys consisting of chromium oxide Cr_2O_3 cores underneath nickel oxide NiO outer layers. Furthermore, it has been historically recognized that NiO films act as diffusion barriers, effectively preventing the inflow of reactive species. More recently, it has been experimentally

demonstrated that that NiO layers completely block the electrochemical reactions and the transmission of charge carriers in the depletion region. These findings help to corroborate the proposed theory.

In general, the subject metals with their passive layers are analogous to pseudo-*n*-type Schottky diodes or barriers in which the oxides act as lightly doped *n*-type semiconductors due to the intrinsic impurities present from natural contaminants when the layer initially develops. Under steady state conditions, no current is drawn (the diffusion current and drift current are equal and opposite) but a small voltage drop is established across the metal-oxide junction, the so-called ‘built-in’ voltage V_{bi} . This is analogous to the larger galvanic potential difference exhibited between dissimilar metals which are in contact and is proportional to the difference between their work functions. The built-in voltage that electron energies must surpass in order to flow corresponds to the Schottky energy barrier height qV_{bi} . For a metal-*n*-type interface or junction, the depletion region occurs only in the oxide phase which creates a space charge electric field where charges q can be stored and hence, a small level of pseudo-capacitance exists. When the passivated metal is placed in an electrolyte, an electrical double layer (EDL) forms and the capacitive space charge widens along with the depletion region as discussed earlier.

In a typical potentiodynamic scan, current is always flowing into the sample while electrons are always flowing outward. When the immersed sample is first subjected to a negative cathodic voltage, an excess of electrons flows outward weakening and disintegrating the initial passive oxide layer in the process as it dissolves in the acidic solution. If held too long in this region, general etching of the base metal will occur. As the potential is increased toward E_{Cor} , the number of excess electrons diminishes and finally goes to zero at E_{Cor} . When the applied potential begins to increase above E_{Cor} into the anodic region, valence electrons are then extracted from the metal as the oxide starts to re-form on the surface. As the anodic (positive) voltage continues to increase, the new oxide layer grows under a ‘reverse bias’ condition through E_{Pas} and into the passive region.

A reverse bias is imposed on the metal-*n*-type junction since the energy barrier for current flow through the oxide layer is increased and the potential across the junction increases. Under this condition, the depletion region expands and the diffusion of electrons attempting to cross the junction is greatly reduced. As long as the applied reverse voltage is in effect and continuing to increase, the total potential across the junction continues to increase toward the built-in voltage while the electric field also increases. A small reverse saturation current is maintained during this segment of the process (for a while). The almost constant reverse current is sustained across the passive plateau as a nominal diffusion of charge carriers continues until the E_{Brk} region is approached. This is representative of the Titanium example given in Figure A21 which depicts four possible responses during anodic polarization of metals. With the Cronidur example in Figure A21, the diffusion current overwhelms the reverse current. For nonpassivating metals, there is no resistance to electron flow and the process is activation-controlled with ideal Tafel behavior. The nickel fraction in the passive layer of alloys such as Inconel and Hastelloy can produce some interesting effects not seen with the other metals.

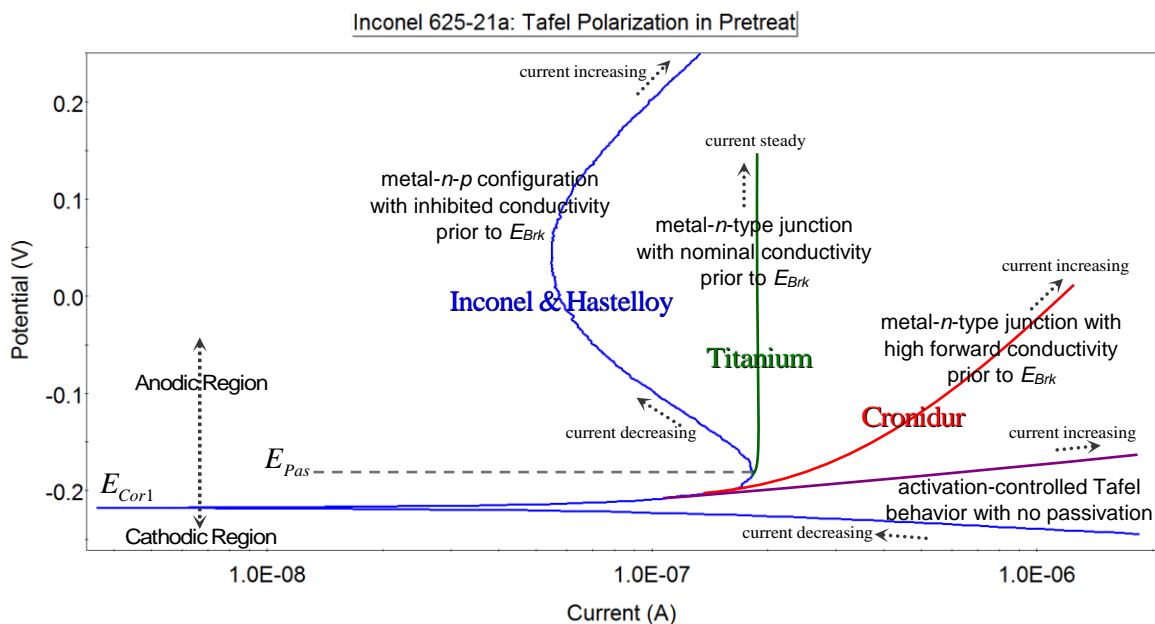


Figure A21: Illustration of possible polarization paths during and after primary passivation.

A couple of points should be emphasized here. The arrows indicate the direction of the scan. However, changes in the value of the current at any given time are not reflective of the direction that the current is flowing. As stated earlier, throughout all these polarization scans, current is always flowing into the sample while electrons are always flowing outward. This is due to the fact that the applied voltage drop across the cell is always forcing electrons to flow out of the sample. In cathodic regions (prior to E_{Cor1} and after E_{Cor2}), excess conduction electrons are flowing outward while during the anodic segments (after E_{Cor1} and prior to E_{Cor2}), valence electrons flow outward. For corroding metals, the current is generally increasing throughout the passive zone (however, forward current does not necessarily mean that corrosion is taking place). A steady current after E_{Pas} implies that the oxide layer is a tenacious semiconductor with a high E_{Brk} while an increasing current could infer a lower E_{Brk} . In single metal scans, particularly for rate estimation purposes, current values are always treated as positive quantities. Outside of the $\pm 50\text{mV}$ linear range, the slope of the scan may be an indicator of whether the current is increasing or decreasing. In general, whenever the current is directed away from the log inflection point, it is increasing and whenever the current is directed toward the inflection point, it is increasing.

The polarization behaviors depicted in Figure A21 for Titanium and Cronidur are well substantiated. However, due to the high nickel content in Inconel and Hastelloy, conduction and electrochemical activity throughout the passivation region is quite different. The 'bowing' feature shown in this plot seems to be characteristic of high nickel alloys as it reflects the abrupt and opposite changes in current that occur after E_{Pas} . The degree of bowing has been seen to vary during different test runs with the largest exaggerations occurring for samples which were cathodically conditioned. While the other metals are known to exhibit single metal- n -type Schottky junctions, the nickel alloys are believed to possess a multi-layer or multi-junction film which possess the characteristics of a bipolar metal- n - p -type barrier configuration. This feature is believed to be directly associated with the extent of phase separation that occurs within the Cr_2O_3 - NiO layer.

While Cr_2O_3 -NiO bilayers likely form to some degree in almost all electrochemical situations, the effects of cathodic conditioning appear to exacerbate the phase separation process as indicated throughout this work. Under ambient conditions, undoped NiO is more of an insulator than a semiconductor with a resistivity on the order of $10^{-13} \Omega\text{-cm}$ and very few charge carriers. These properties are key in determining the extent that NiO will behave as a diffusion barrier. Consider the activities illustrated in Figure A22 as a high Ni-Cr metal undergoes anodic passivation under reverse bias conditions.

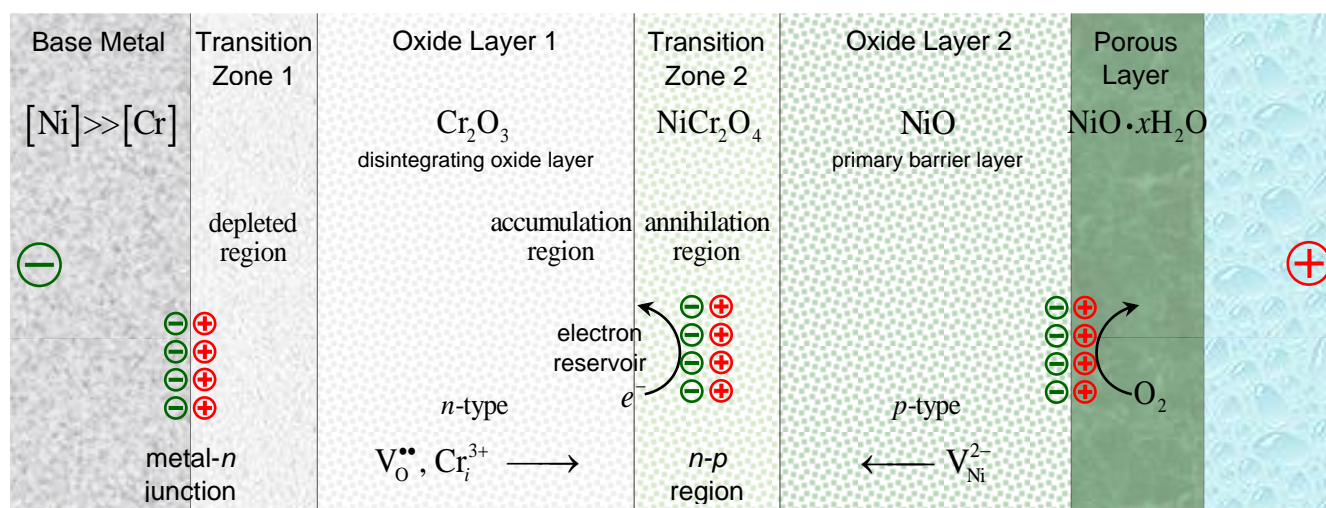


Figure A22: Illustration of possible processes during anodic passivation of Ni-Cr alloys under reverse bias.

The Ni-Cr substrate is highly conductive metal that provides a Schottky-type ohmic contact to the *n*-type Cr_2O_3 oxide region (which includes Transition Zone 1 for the most part). However, the applied negative potential to metal side causes an increase in the energy barrier against electron flow through the metal-*n*-type junction into the Cr_2O_3 layer. This leads to the accumulation of electrons on the other side of the Cr_2O_3 layer. Transition Zone 1 is the gradient transition region between metal and oxide. Electrons are also depleted in this zone so creation of the primary charge carriers is restricted. As iterated earlier, the majority carriers in the *n*-region are electron donors which have been identified as oxygen vacancies $V_{\text{O}}^{\bullet\bullet}$ and interstitial chromium cations Cr_i^{3+} that flow toward Transition Zone 2. This zone is first created by reactions between Cr_2O_3 and NiO during the initial passivation process, and it is shrinking as the NiO outer layer increases in thickness.

In the *p*-type NiO phase, the majority carriers are nickel cation vacancies which flow toward Transition Zone 2 from the other direction. Collisions between opposing charge carriers creates an annihilation region which prevents the flow of electrons into the NiO phase. Thus, inbound current and outbound electron flow are essentially cut off, similar to a *p-n-p* bipolar transistor in ‘cut-off’ mode where very little current flows. Since the number of donors and acceptors in both regions is severely limited, annihilation activity is minimal while an excess of electrons become trapped within the Cr_2O_3 layer. In essence, the external NiO layer acts as a barrier, limiting the diffusion of oxygen from the outside and trapping the outflow of electrons from the inside. This condition creates a chemical reduction environment within the Cr_2O_3 region that destabilizes the oxide structure with increasing detrimental effects as the

applied voltage continues to increase (analogous to cathodic disintegration). For additional clarity, Figure A23 gives the cyclic polarization semi-log scan for the sample depicted in Figure A20.

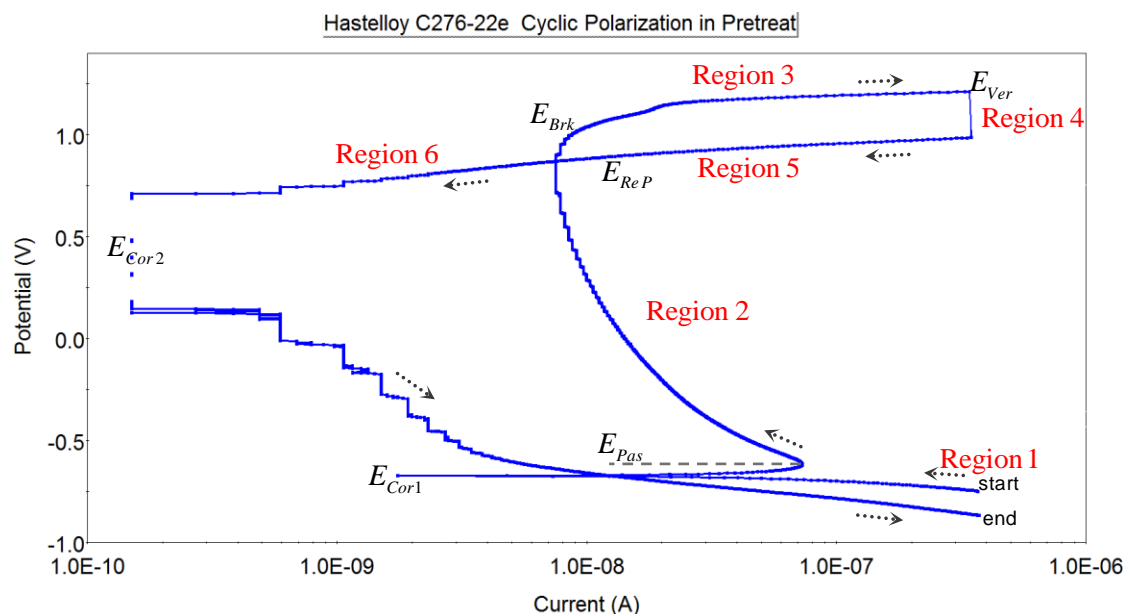


Figure A23: Cyclic polarization scan for the anomalous Hastelloy sample shown in Figure A20.

As iterated earlier, current is always flowing inward while electrons are always flowing outward. The arrows map-out the scan direction but they may also indicate the relative increases and decreases in electron flow. When polarization starts in the cathodic region, the sample is a positively charged cathode that is becoming less cathodic as the potential increases and approaches E_{Cor1} . At E_{Cor1} , the sample reverses polarity and becomes a negatively charged anode. For metals containing semiconductive passive layers, this corresponds to an applied reverse bias on the sample throughout the anodic branch. Forward bias occurs during the cathodic branches (prior to E_{Cor1} and after E_{Cor2}) where reductive cathodic dissolution of the oxide layer is possible.

Region 1 in Figure A23 marks the beginning of this test at $-0.75V$ just after constant cathodic conditioning was applied for five minutes. The applied potential (vs. $Ag/AgCl$) is negative in this region. It is suspected that most, if not all, of the original air-formed oxide layer was removed before the forward scan begin. At the start, there was an abundance of free electrons (excess conduction electrons) supplied by the power source. As the potential is increased, these electrons are rapidly ejected as E_{Cor1} is approached. At E_{Cor1} , the sample polarity reverses and becomes positive while all the excess electrons are depleted. As E_{Cor1} is surpassed, the current continues increasing while anodic oxidation (passivation) of the metal surface commences and valence electrons (bound atomic electrons) begin to flow outward. The specific value of E_{Cor} attained is unique to the metal and its interaction with the particular solution. Between E_{Cor1} and E_{Pas} , the Cr_2O_3 layer begins to form almost immediately followed by formation of the $NiCr_2O_4$ and NiO layers. Under increasing reverse bias conditions, the actual time lapse between development of the Cr-rich sublayer and the Ni-rich outer layer is greatly reduced. By the time E_{Pas} is reached, a heavy Ni-rich layer has developed in the outer regions of the passive layer which leads to the ‘bowing’ effect seen on the plot.

In Region 2, just beyond E_{Brk} , the current decreases as the applied voltage continues to increase up to the threshold potential just prior to E_{Brk} . This indicates that the outflow of electrons has become blocked by the outer NiO barrier. Additionally, the NiO layer inhibits the inflow of oxygen from the outside which reduces the passivation reactions at the metal substrate and essentially ‘cuts off’ the growth of protective Cr_2O_3 . This imposes strong reduction forces on the Cr_2O_3 layer as the outer NiO layer then becomes the primary protection barrier. The NiO layer is essentially acting as a MOS capacitor. Accumulation of electrons in the Cr_2O_3 layer leads to a condition where the Cr_2O_3 structure becomes cathodically weakened. As the potential continues to increase toward the threshold point, the shielded Cr_2O_3 lattice likely undergoes chemical reduction and possibly cathodic weakening. Mobile chromium particles and oxygen may be produced in this space prior to E_{Brk} , $Cr_2O_3 \longrightarrow Cr^0 + 1\frac{1}{2}O_2\uparrow$, and outgassing may increase the pressure inside the volume beneath the NiO layer. For this particular run, the intersecting scan lines happen to correspond roughly to both the threshold potential and the repassivation potential E_{ReP} .

The indicated breakdown potential probably pertains to or is dominated by the NiO phase. At E_{Brk} , an abrupt increase in the current occurs as electrons begin tunneling through the layer followed by avalanche outflow. At the beginning of Region 3 (i.e... at E_{Brk}), anodic disintegration of NiO commences and nickel cations are ejected into the solution, $Ni_{Ni} \longrightarrow Ni^{2+}(aq) + V_{Ni}^{2+} + 2e^-$, as the NiO layer begins to break apart and dissolve in the acid, $NiO + 2H^+ \longrightarrow Ni^{2+}(aq) + H_2O$. Since the Cr_2O_3 layer is depleted when the NiO layer ruptures and dissolves, the base metal is instantly exposed to the highly anodic acid solution. Throughout Region 3 (E_{Brk} to E_{Ver}), rapid and aggressive etching of the base metal takes place which temporarily overwhelms the metal’s repassivation protection mechanism, $Ni^0 + 2H^+ \longrightarrow Ni^{2+}(aq) + H_2\uparrow$ and $Cr^0 + 6H^+ \longrightarrow Cr^{6+}(aq) + 3H_2\uparrow$. Etching ceases at E_{Ver} (the relief point) where the increasing voltage ramp reverses and begins to decrease.

The short vertical segment depicted by Region 4 reflects a small time period, just before repassivation begins, when the current change is almost nil. Due to the heavy concentration of Ni^{2+} ions in close proximity to the surface, it is possible a small degree of metallization or back-plating may have occurred. Once repassivation initiates, this very thin, shiny Ni deposit would be stabilized. Regions 5 and 6 represent the reactions associated with repassivation, oxide regeneration and recovery of the Ni-Cr surface. Recall that E_{ReP} is the point where the repassivation rate rapidly starts tapering off. It is usually not visible on the log plot but is quite pronounced on the normal plot. It has been observed with these metals that after the voltage ramp reverses, repassivation is usually swift and powerful. Along Region 5, new oxide is rapidly being deposited, and then following E_{ReP} , electrolytic polishing of the surface may take place which could also impart a shiny appearance as seen in the photo. Positively charged Ni complexes and hydrates saturate the adjacent solution within the Nernst layer. They are attracted to and neutralized along the negative oxide surface. At E_{Cor2} (the polarity reversal point), these products become loosely bound. Beyond E_{Cor2} , the damaged sample area is completely covered with new oxide and green Ni precipitates as it becomes increasingly more cathodic until the scan ends. While there is no solid corroborating evidence to support this scenario at this time, it does explain the observed phenomena to a reasonable degree.

References

1. “ECLSS Sustaining Metal Materials Compatibility Final Report, Electrochemical and Crevice Corrosion Test Results”, R.E. Lee, NASA/CR—2015–218208, April 2015, Contract NNM12AA41C
2. “ECLSS Sustaining Metal Materials Compatibility Final Briefing, Electrochemical and Crevice Corrosion Test Results”, October 6, 2014, Randy Lee
3. “Corrosion Protection for Space Flight Hardware”, NASA Technical Standard NASA-STD-6012, March 8, 2012

| REPORT DOCUMENTATION PAGE | | | | Form Approved OMB No. 0704-0188 | |
|--|----------------------|-------------------------------------|--------------------------------------|--|--|
| <p>The public reporting burden for this collection of information is estimated to average 1 hour per response, including the time for reviewing instructions, searching existing data sources, gathering and maintaining the data needed, and completing and reviewing the collection of information. Send comments regarding this burden estimate or any other aspect of this collection of information, including suggestions for reducing this burden, to Department of Defense, Washington Headquarters Services, Directorate for Information Operation and Reports (0704-0188), 1215 Jefferson Davis Highway, Suite 1204, Arlington, VA 22202-4302. Respondents should be aware that notwithstanding any other provision of law, no person shall be subject to any penalty for failing to comply with a collection of information if it does not display a currently valid OMB control number.</p> <p>PLEASE DO NOT RETURN YOUR FORM TO THE ABOVE ADDRESS.</p> | | | | | |
| 1. REPORT DATE (DD-MM-YYYY) 01-12-2019 | | 2. REPORT TYPE Contractor Report | | 3. DATES COVERED (From - To) 11/01/17 - 11/30/19 | |
| 4. TITLE AND SUBTITLE Electrochemical, Polarization, and Crevice Corrosion Testing of Inconel X750 A Supplement to the Environmental Control and Life Support System Sustaining Metal Materials Compatibility Study | | | | 5a. CONTRACT NUMBER 80MSFC18C0011 | |
| | | | | 5b. GRANT NUMBER | |
| | | | | 5c. PROGRAM ELEMENT NUMBER | |
| 6. AUTHOR(S) R.E. Lee | | | | 5d. PROJECT NUMBER | |
| | | | | 5e. TASK NUMBER | |
| | | | | 5f. WORK UNIT NUMBER | |
| 7. PERFORMING ORGANIZATION NAME(S) AND ADDRESS(ES) Jacobs Space Exploration Group (JSEG)/Bevilacqua Research Corporation Marshall Space Flight Center, Huntsville, AL | | | | 8. PERFORMING ORGANIZATION REPORT NUMBER M-1497 | |
| 9. SPONSORING/MONITORING AGENCY NAME(S) AND ADDRESS(ES) George C. Marshall Space Flight Center Huntsville, AL 35812 | | | | 10. SPONSORING/MONITOR'S ACRONYM(S) | |
| | | | | 11. SPONSORING/MONITORING REPORT NUMBER NASA/CR-2019-220550 | |
| 12. DISTRIBUTION/AVAILABILITY STATEMENT Unclassified-Unlimited Subject Category 26 Availability: NASA STI Information Desk (757-864-9658) | | | | | |
| 13. SUPPLEMENTARY NOTES Prepared for the Materials & Processes Laboratory, Engineering Directorate NASA Technical Monitor: T. Kent Pendergrass | | | | | |
| 14. ABSTRACT Electrochemical corrosion evaluations were conducted on samples of Inconel X750 in support of the materials compatibility program for the Environmental Control and Life Support System. The results were compared alongside those of several previously qualified metals, Titanium 6Al-4V, Inconel 625, Hastelloy C276, and Nitinol 60. While Titanium exhibited the best results of all, Inconel X750 demonstrated anti-corrosion properties similar to those of Hastelloy C276 and Inconel 625. For this current effort, the results have clearly shown that Inconel X750 possesses excellent corrosion protection properties and is galvanically compatible with each of the other metals in the subject test media. | | | | | |
| 15. SUBJECT TERMS corrosion, electrochemistry, polarization, pitting, galvanic, ECLSS | | | | | |
| 16. SECURITY CLASSIFICATION OF: | | | 17. LIMITATION OF ABSTRACT UU | 18. NUMBER OF PAGES 76 | 19a. NAME OF RESPONSIBLE PERSON STI Help Desk at email: help@sti.nasa.gov |
| a. REPORT U | b. ABSTRACT U | c. THIS PAGE U | | | 19b. TELEPHONE NUMBER (Include area code) STI Help Desk at: 757-864-9658 |

National Aeronautics and
Space Administration
IS02

George C. Marshall Space Flight Center
Huntsville, Alabama 35812